Lattice Boltzmann models based on the vielbein formalism for the simulation of flows in curvilinear geometries

Sergiu Busuioc and Victor E. Ambruş

Lattice Boltzmann models based on the vielbein formalism
for the simulation of flows in curvilinear geometries

Sergiu Busuioc[1, *] and Victor E. Ambruș[1, †]

[1] *Department of Physics, West University of Timișoara,*
Vasile Pârvan Avenue 4, 300223 Timișoara, Romania
(Dated: January 7, 2019)

In this paper, we consider the Boltzmann equation with respect to orthonormal vielbein fields in conservative form. This formalism allows the use of arbitrary coordinate systems to describe the space geometry, as well as of an adapted coordinate system in the momentum space, which is linked to the physical space through the use of vielbeins. Taking advantage of the conservative form, we derive the macroscopic equations in a covariant tensor notation, and show that the hydrodynamic limit can be obtained via the Chapman-Enskog expansion in the Bhatnaghar-Gross-Krook (BGK) approximation for the collision term. We highlight that in this formalism, the component of the momentum which is perpendicular to some curved boundary can be isolated as a separate momentum coordinate, for which the half-range Gauss-Hermite quadrature can be applied. We illustrate the capabilities of this formalism by considering two applications. The first one is the circular Couette flow between rotating coaxial cylinders, for which benchmarking data is available for all degrees of rarefaction, from the hydrodynamic to the ballistic regime. The second application concerns the flow in a gradually expanding channel. We employ finite-difference lattice Boltzmann models based on half-range Gauss-Hermite quadratures for the implementation of diffuse reflection, together with the fifth order WENO and third-order TVD Runge-Kutta numerical methods for the advection and time-stepping, respectively.

I. INTRODUCTION

Rarefied gas flows, where non-equilibrium effects become important and the Navier-Stokes equations are no longer applicable, can be successfully described within the framework of the Boltzmann equation [1–11]. Microfluidics specific effects (e.g. velocity slip, temperature jump) can be recovered by modelling the boundary conditions at the level of the Boltzmann distribution function $f \equiv f(\boldsymbol{x}, \boldsymbol{p}, t)$ (i.e. by imposing kinetic boundary conditions). According to the diffuse reflection concept, the particles reflected from the wall back into the fluid follow a Maxwellian distribution (all quantities are non-dimensionalized following the convention of Refs. [12–16]):

$$f_w(p_n < 0) = \frac{n_w}{(2\pi m T_w)^{3/2}} \exp\left[-\frac{(\boldsymbol{p} - m\boldsymbol{u}_w)^2}{2mT_w}\right], \quad (1.1)$$

where n_w, T_w and $\boldsymbol{u}_w$ are the particle number density, temperature and velocity of the wall. In the above, $p_n \equiv \boldsymbol{p} \cdot \boldsymbol{n}$ represents the projection of the particle momentum vector on the outwards-directed normal $\boldsymbol{n}$ to the wall, such that particles for which $p_n < 0$ travel from the wall back into the fluid domain.

Since the incident particle flux is a-priori essentially arbitrary, prescribing the distribution of emerging particles via Eq. (1.1) induces a discontinuity in the functional form of the distribution function [17]. Furthermore, the

impermeability of the wall is ensured by requiring that the mass flux through the boundary vanishes:

$$\int_{p_n < 0} d^3p \, f_w \, p_n = -\int_{p_n > 0} d^3p \, f \, p_n, \quad (1.2)$$

The correct numerical implementation of Eq. (1.2) requires the ability to recover half-range integrals of the distribution function. This can be done by choosing the discrete set of momentum vectors and their associated quadrature weights following the prescription of half-range Gauss quadrature methods [16, 18–36]. Since the Gauss quadratures are one-dimensional [37, 38], the integration over the momentum space must be split into a product of one-dimensional integrals. The half-range integration can be performed using a half-range Gauss-Hermite quadrature only if the integration range along this direction is $[0, \infty)$ or $(-\infty, 0]$. This implies that, for the Cartesian split of the integration domain (i.e. when the integrals over p_x, p_y and p_z are performed separately), the domain walls have to be orthogonal to the Cartesian axes. For example, for a wall perpendicular to the z axis, the integration in Eq. (1.2) is performed over the ranges $p_x, p_y \in (-\infty, \infty)$ and $p_z \in [0, \pm\infty)$. This results in a limitation of the applicability of the presently-available models based on half-range quadratures when curved or arbitrary boundaries are considered.

It is a common practice in the literature to exploit the symmetries of a non-Cartesian geometry by using curvilinear geometry-fitted coordinates [18–21, 39–47]. The coordinate system can be chosen such that the boundary is always orthogonal to the unit vector along one of the curvilinear coordinates. In order to apply the half-range quadrature along the direction perpendicular to the wall, one further step must be taken: the momentum space has

to be adapted to the new coordinate system, such that the components of the momentum vector always point along the unit vectors corresponding to the curvilinear coordinates.

In Ref. [48], Cardall et al. expressed the relativistic Boltzmann equation in conservative form with respect to a vielbein (i.e. tetrad in $4D$ spacetime) field and a general choice for the parametrization of the momentum space. In this paper, we present a formulation of the non-relativistic Boltzmann equation with respect to general coordinates. In order to keep the momentum space tied to the new coordinate frame, we employ an orthonormal vielbein field (i.e. a triad consisting of the non-commuting unit vectors of the coordinate frame) with respect to which the momentum space degrees of freedom are defined. The resulting Boltzmann equation contains inertial forces which ensure that freely-streaming particles travel along straight lines in the original Cartesian geometry. Key to this development is the use of the tools of differential geometry. It is worth mentioning that differential geometry and the vielbein formalism have been used previously in fluid dynamics, in particular for the study of flows on curved surfaces [49–52].

In order to demonstrate the robustness of our proposed formulation, we introduce the conservative form of the Boltzmann equation, with the help of which the Navier-Stokes equations with respect to general coordinates are derived via the Chapman-Enskog expansion. This is the main result of this paper.

The applicability of our proposed scheme to rarefied flows enclosed inside curved boundaries is demonstrated by considering two applications, namely the circular Couette flow between coaxial cylinders and the flow in a gradually expanding channel, which are described in what follows.

In the first case, cylindrical coordinates are used to parametrize the flow domain, such that the boundaries are orthogonal to the radial (R) direction. After defining the momentum space with respect to the unit vectors along the radial, azimuthal and z directions, the mixed-quadrature lattice Boltzmann (LB) models introduced in Ref. [34] are employed. These models allow the quadrature (half-range or full-range Gauss-Hermite) to be chosen on each axis separately. The implementation of the inertial forces requires the theory of distributions, as discussed in Ref. [36].

In Ref. [53], a D2Q9 collide-and-stream LB model was adapted to recover the Navier-Stokes equations with respect to the cylindrical coordinate system. In the resulting scheme, the velocity space parametrization is performed along the coordinate system unit vectors, however, its applicability is restricted to the hydrodynamic regime. Due to the collide-and-stream paradigm, the computational domain still required a two-dimensional discretization.

In Refs. [42, 43, 45, 46], the LB model was employed using a discretization with respect to cylindrical coordinates, but the momentum space degrees of freedom were the Cartesian ones. This discrepancy between the momentum space and the flow domain resulted in a broken symmetry which required a two-dimensional discretization of the flow domain. Furthermore, the aforementioned studies are limited to low Mach number flow regimes, where the flow is essentially incompressible. In our implementation of the circular Couette flow, the axial symmetry is preserved also in the momentum space, such that the discretization of the flow domain can be performed in a one-dimensional fashion, along the radial coordinate (with only one point along the azimuthal and z coordinates, where periodic boundary conditions apply), greatly reducing the total number of grid points required to obtain accurate results. Also, the half-range quadratures employed in our models allow us to model highly compressible flows for which the profiles of the macroscopic velocity, number density, temperature and heat fluxes are correctly recovered.

The velocity sets employed in our models are prescribed via Gauss quadrature rules and are in general off-lattice (i.e. the velocity vectors cannot point simultaneously to neighbouring lattice sites). Therefore, the widely-used collide-and-stream paradigm is inapplicable with our models and we are forced to resort to finite-difference schemes [54–77]. In order to ensure good accuracy of the spatial scheme, the fifth order Weighted Essentially Non-Oscillatory (WENO-5) scheme was employed [45, 78–83]. For the time marching, the third-order total variation diminishing (TVD) Runge-Kutta method described in [82, 84–87] was employed. Furthermore, the resolution near the bounding cylinders is increased by performing a stretching of the radial grid points through a coordinate transformation which is compatible with our proposed numerical scheme, as described in Refs. [40, 65].

Our scheme is validated in the context of the circular Couette flow problem in three flow regimes: the hydrodynamic (Navier-Stokes) regime, the transition regime and the ballistic (free-streaming) regime. In the hydrodynamic and ballistic regimes, our simulation results are compared with the analytic solution of the compressible Navier-Stokes and collisionless Boltzmann equations, respectively. In the slip-flow and transition regimes, our results are compared with those reported in Ref. [88] by Aoki et al. In all cases, an excellent match is found and we conclude that our scheme can be successfully applied for the simulation of the circular Couette flow.

Since the aim of this paper is to demonstrate the applicability of the lattice Boltzmann models based on half-range Gauss-Hermite quadratures introduced in Refs. [34, 36] for the study of rarefied flows confined in non-rectangular geometries, our study of the circular Couette flow is limited to the case of pure diffuse reflection (unit accommodation coefficient). We therefore do not discuss other interesting aspects of the circular Couette flow, such as the Taylor-Couette instability appearing at large values of the Taylor number [89, 90], or the inverted velocity profile due to sub-unitary accom-

modation coefficients [88, 91–99].

The second application consists of the gradually expanding channel introduced by Roache in Ref. [100]. This configuration is interesting since the flow features exhibit scale invariance at sufficiently large values of the Reynolds number Re. In particular, the results for Re = 100 already give a reasonable approximation of the flow features when Re → ∞. Subsequently, this problem was considered by 15 participant groups who attended the fifth workshop of the International Association for Hydraulic Research (IAHR) Working Group on Refined Modelling of Flows, held in Rome on 24-25th May 1982 and was reported in Ref. [101] for benchmarking purposes.

Before ending the introduction, we note that our study is limited to the case when the quadrature method is based on a Cartesian split of the momentum space. More efficient lattice Boltzmann algorithms may be developed by choosing a parametrization of the momentum space (after aligning the momentum space with respect to the triad) which shares the symmetries of the flow. In particular, a cylindrical coordinate system in the momentum space, such as the shell-based models introduced in Ref. [57] and further employed in Refs. [43, 102–104] may be more suitable for the simulation of flows with cylindrical symmetry. For flows with spherical symmetry, it may be convenient to parametrize the momentum space using spherical coordinates, as discussed in Refs. [105, 106]. However, to the best of our knowledge, none of the above mentioned models have been endowed with half-range capabilities. We thus postpone the study of flows in curvilinear geometries using non-Cartesian parametrizations of the momentum space for future work.

The paper is structured as follows. In Sec. II, we lay the theoretical foundation for our scheme by introducing the non-relativistic Boltzmann equation in conservative form with respect to orthonormal vielbein fields (i.e. triads in 3D space). In Subsec. II C, the Navier-Stokes equations are derived with respect to general coordinates via the Chapman-Enskog expansion. The numerical scheme and the implementation of the boundary conditions are discussed in Sec. III. The lattice Boltzmann algorithm is reviewed in Sec. IV. In Sec. V, the vielbein formalism is specialized to the case of the circular Couette flow and the numerical results are compared to analytic solutions in the Navier-Stokes (Subsec. V D) and collisionless (Subsec. V E) regimes, as well as with the DVM results in Ref. [88] in the transition regime. The flow through the gradually expanding channel is presented in Sec. VI. Our conclusions are presented in Sec. VII. Appendices A–C contain supplementary mathematical details required in Sec. II, while Appendix D discusses the implementation of the momentum space derivative of the distribution function in the lattice Boltzmann method employed in this paper.

II. BOLTZMANN EQUATION WITH RESPECT TO TRIADS

To better illustrate the use of triads, we refer the reader to Fig. 1, where the space between two coaxial cylinders constitutes the flow domain. The spatial grid can be constructed in two ways: using Cartesian coordinates (a) or cylindrical/polar coordinates (b and c). Similarly, the momentum space degrees of freedom can be chosen along the Cartesian axes (a and b) or along the cylindrical axes (c).

The grid in Fig. 1(a) requires a staircase (polygonal) approximation of the boundary and thus the results are dependent on the resolution of the grid around the boundary. The resulting grid is $2D$.

In Fig. 1(b), a cylindrical coordinate system (R, φ) is used to describe the flow domain. This ensures the exact representation of the boundary. However, the momentum space degrees of freedom point along the Cartesian axes (p_x, p_y). The resulting setup is not invariant under rotations since a rotation about the symmetry axis also rotates the momentum space. Thus, a $2D$ grid is required.

The final step is to orient the momentum space along the cylindrical coordinates $(p_{\hat{R}}, p_{\hat{\varphi}})$, as shown in Fig. 1(c). This results in a representation of the flow domain and particle momenta which is fully symmetric with respect to rotations about the symmetry axis. In order to achieve the alignment of the momentum space along the new coordinate system, an orthonormal triad must be employed, as described in the current Section.

The Boltzmann equation when non-Cartesian coordinates are used for the spatial domain and the momentum space degrees of freedom are taken with respect to a triad is derived in Subsec. II A. Using the conservative form of this equation derived in Subsec. II B, the application of the Chapman-Enskog procedure for the derivation of the conservation equations in the hydrodynamic limit is illustrated in Subsec. II C.

A. Advective form

The Boltzmann equation with respect to the Cartesian coordinates $\{x, y, z\}$ can be written as:

$$\frac{\partial f}{\partial t} + \frac{p^i}{m}\frac{\partial f}{\partial x^i} + F^i\frac{\partial f}{\partial p^i} = J[f], \qquad (2.1)$$

where f is the Boltzmann distribution function, m is the mass of the fluid particles, while p^i and F^i represent the Cartesian components of the fluid particle momentum and of the external force, respectively.

In certain situations, it is convenient to introduce a set of arbitrary coordinates $\{x^{\tilde{1}}, x^{\tilde{2}}, x^{\tilde{3}}\}$, where $x^{\tilde{i}} \equiv x^{\tilde{i}}(x, y, z)$ (in this paper, we restrict our analysis to time-independent coordinate transformations). This coordi-

nate transformation induces a metric $g_{\widetilde{i}\widetilde{j}}$, as follows:

$$ds^2 = \delta_{ij}dx^i dx^j = dx^2 + dy^2 + dz^2$$
$$= g_{\widetilde{i}\widetilde{j}}dx^{\widetilde{i}}dx^{\widetilde{j}}, \tag{2.2}$$

such that

$$g_{\widetilde{i}\widetilde{j}} = \delta_{ij}\frac{\partial x^i}{\partial x^{\widetilde{i}}}\frac{\partial x^j}{\partial x^{\widetilde{j}}}. \tag{2.3}$$

The Boltzmann equation (2.1) can be written in advective form with respect to these new coordinates as follows:

$$\frac{\partial f}{\partial t} + \frac{p^{\widetilde{i}}}{m}\frac{\partial f}{\partial x^{\widetilde{i}}} + \left(F^{\widetilde{i}} - \frac{1}{m}\Gamma^{\widetilde{i}}_{\widetilde{j}\widetilde{k}}p^{\widetilde{j}}p^{\widetilde{k}}\right)\frac{\partial f}{\partial p^{\widetilde{i}}} = J[f], \quad (2.4)$$

where the components $p^{\widetilde{i}}$ and $F^{\widetilde{i}}$ with respect to the new coordinates are related to the components p^i and F^i with respect to the old coordinates through:

$$p^{\widetilde{i}} = \frac{\partial x^{\widetilde{i}}}{\partial x^i}p^i, \qquad F^{\widetilde{i}} = \frac{\partial x^{\widetilde{i}}}{\partial x^i}F^i. \tag{2.5}$$

The Christoffel symbols $\Gamma^{\widetilde{i}}_{\widetilde{j}\widetilde{k}}$ appearing in Eq. (2.4) are defined as:

$$\Gamma^{\widetilde{i}}_{\widetilde{j}\widetilde{k}} = \frac{\partial x^{\widetilde{i}}}{\partial x^\ell}\frac{\partial^2 x^\ell}{\partial x^{\widetilde{j}}\partial x^{\widetilde{k}}}$$
$$= \frac{1}{2}g^{\widetilde{i}\widetilde{\ell}}\left(\partial_{\widetilde{k}}g_{\widetilde{\ell}\widetilde{j}} + \partial_{\widetilde{j}}g_{\widetilde{\ell}\widetilde{k}} - \partial_{\widetilde{\ell}}g_{\widetilde{j}\widetilde{k}}\right). \tag{2.6}$$

Further details regarding the connection between Eqs. (2.1) and (2.4) can be found in Appendix A.

The above formalism is sufficient to adapt the coordinate system to a curved boundary. However, the transition to an LB model is not straightforward, since the momentum space has an intrinsic dependence on the coordinates. Indeed, the Maxwellian distribution corresponding to a particle number density n, macroscopic velocity $\boldsymbol{u}$ and temperature T has the expression:

$$f^{(\text{eq})} = \frac{n}{(2\pi mT)^{\frac{3}{2}}}\exp\left[-\frac{g_{\widetilde{i}\widetilde{j}}(p^{\widetilde{i}} - mu^{\widetilde{i}})(p^{\widetilde{j}} - mu^{\widetilde{j}})}{2mT}\right], \tag{2.7}$$

while its moments are calculated as:

$$M^{\widetilde{i}_1,\cdots\widetilde{i}_n}_{\text{eq}} = \sqrt{g}\int d^3\widetilde{p}\, f^{(\text{eq})}p^{\widetilde{i}_1}\cdots p^{\widetilde{i}_n}, \tag{2.8}$$

where g is the determinant of the metric tensor $g_{\widetilde{i}\widetilde{j}}$.

In order to eliminate the burden of this metric dependence in the expression for the Maxwellian, it is convenient to introduce a triad (vielbein) with respect to which the metric is diagonal:

$$g_{\widetilde{i}\widetilde{j}}dx^{\widetilde{i}} \otimes dx^{\widetilde{j}} = \delta_{\hat{a}\hat{b}}\omega^{\hat{a}} \otimes \omega^{\hat{b}}, \tag{2.9}$$

where the triad one-forms $\omega^{\hat{a}}$ are defined as:

$$\omega^{\hat{a}} = \omega^{\hat{a}}_{\widetilde{j}}dx^{\widetilde{j}}, \tag{2.10}$$

such that:

$$g_{\widetilde{i}\widetilde{j}} = \delta_{\hat{a}\hat{b}}\omega^{\hat{a}}_{\widetilde{i}}\omega^{\hat{b}}_{\widetilde{j}}. \tag{2.11}$$

The above equation allows three degrees of freedom for the system $\{\omega^{\hat{a}}_{\widetilde{j}}\}$, corresponding to the invariance of the right hand side of Eq. (2.11) under rotations with respect to the hatted indices. It is possible to define triad vectors dual to the above one-forms by introducing the following inner product:

$$\langle \omega^{\hat{b}}, e_{\hat{a}}\rangle \equiv \omega^{\hat{b}}_{\widetilde{i}}e^{\widetilde{i}}_{\hat{a}} = \delta^{\hat{b}}_{\hat{a}}, \tag{2.12}$$

where

$$e_{\hat{a}} = e^{\widetilde{i}}_{\hat{a}}\frac{\partial}{\partial x^{\widetilde{i}}}. \tag{2.13}$$

Using the above triad, the components of vectors can be expressed as follows:

$$p^{\hat{a}} = \omega^{\hat{a}}_{\widetilde{i}}p^{\widetilde{i}}, \tag{2.14}$$

such that

$$g_{\widetilde{i}\widetilde{j}}p^{\widetilde{i}}p^{\widetilde{j}} = \delta_{\hat{a}\hat{b}}p^{\hat{a}}p^{\hat{b}}. \tag{2.15}$$

Thus, the metric dependence in the Maxwellian (2.7) disappears:

$$f^{(\text{eq})} = \frac{n}{(2\pi mT)^{\frac{3}{2}}}\exp\left[-\frac{\delta_{\hat{a}\hat{b}}(p^{\hat{a}} - mu^{\hat{a}})(p^{\hat{b}} - mu^{\hat{b}})}{2mT}\right], \tag{2.16}$$

allowing its moments to be written as:

$$M^{\hat{a}_1,\cdots\hat{a}_s}_{\text{eq}} = \int d^3\hat{p}\, f^{(\text{eq})}p^{\hat{a}_1}\cdots p^{\hat{a}_s}. \tag{2.17}$$

The expressions for the lower order moments of $f^{(\text{eq})}$ are listed below:

$$M_{\text{eq}} = n, \quad M^{\hat{a}}_{\text{eq}} = \rho u^{\hat{a}}, \quad M^{\hat{a}\hat{b}}_{\text{eq}} = m(P\delta^{\hat{a}\hat{b}} + \rho u^{\hat{a}}u^{\hat{b}}),$$
$$M^{\hat{a}\hat{b}\hat{c}}_{\text{eq}} = m^2 P(u^{\hat{a}}\delta^{\hat{b}\hat{c}} + u^{\hat{b}}\delta^{\hat{a}\hat{c}} + u^{\hat{c}}\delta^{\hat{a}\hat{b}}) + m^2\rho u^{\hat{a}}u^{\hat{b}}u^{\hat{c}},$$
$$M^{\hat{a}\hat{b}\hat{c}\hat{d}}_{\text{eq}} = m^2 PT(\delta^{\hat{a}\hat{b}}\delta^{\hat{c}\hat{d}} + \delta^{\hat{a}\hat{c}}\delta^{\hat{b}\hat{d}} + \delta^{\hat{a}\hat{d}}\delta^{\hat{b}\hat{c}})$$
$$+ m^3 P(u^{\hat{a}}u^{\hat{b}}\delta^{\hat{c}\hat{d}} + u^{\hat{a}}u^{\hat{c}}\delta^{\hat{b}\hat{d}} + u^{\hat{a}}u^{\hat{d}}\delta^{\hat{b}\hat{c}}$$
$$+ u^{\hat{b}}u^{\hat{c}}\delta^{\hat{a}\hat{d}} + u^{\hat{b}}u^{\hat{d}}\delta^{\hat{a}\hat{c}} + u^{\hat{c}}u^{\hat{d}}\delta^{\hat{a}\hat{b}})$$
$$+ m^3\rho u^{\hat{a}}u^{\hat{b}}u^{\hat{c}}u^{\hat{d}}. \tag{2.18}$$

It will be useful to introduce at this point the notation for the moments of the distribution function f:

$$M^{\hat{a}_1,\cdots\hat{a}_s} = \int d^3\hat{p}\, f\, p^{\hat{a}_1}\cdots p^{\hat{a}_s}. \tag{2.19}$$

The Boltzmann equation can now be written in advective form in terms of the triad components of the momentum vectors, as follows:

$$\frac{\partial f}{\partial t} + \frac{p^{\hat{a}}}{m}e^{\widetilde{i}}_{\hat{a}}\frac{\partial f}{\partial x^{\widetilde{i}}} + \left(F^{\hat{a}} - \frac{1}{m}\Gamma^{\hat{a}}_{\hat{b}\hat{c}}p^{\hat{b}}p^{\hat{c}}\right)\frac{\partial f}{\partial p^{\hat{a}}} = J[f], \quad (2.20)$$

where the connection coefficients $\Gamma^{\hat{a}}{}_{\hat{b}\hat{c}}$ are defined by:

$$\Gamma^{\hat{a}}{}_{\hat{b}\hat{c}} = \omega^{\hat{a}}_{\tilde{\imath}}\Gamma^{\tilde{\imath}}_{\tilde{\jmath}\tilde{k}}e^{\tilde{\jmath}}_{\hat{b}}e^{\tilde{k}}_{\hat{c}} - e^{\tilde{\imath}}_{\hat{b}}e^{\tilde{\jmath}}_{\hat{c}}\frac{\partial\omega^{\hat{a}}_{\tilde{\imath}}}{\partial x^{\tilde{\jmath}}}$$

$$= \frac{1}{2}\delta^{\hat{a}\hat{d}}\left(c_{\hat{d}\hat{b}\hat{c}} + c_{\hat{d}\hat{c}\hat{b}} - c_{\hat{b}\hat{c}\hat{d}}\right), \qquad (2.21)$$

while the Cartan coefficients $c_{\hat{b}\hat{c}}{}^{\hat{a}} = \delta^{\hat{a}\hat{d}}c_{\hat{b}\hat{c}\hat{d}}$ can be obtained using:

$$c_{\hat{b}\hat{c}}{}^{\hat{a}} = \langle\omega^{\hat{a}}, [e_{\hat{b}}, e_{\hat{c}}]\rangle, \qquad (2.22)$$

while $c_{\hat{b}\hat{c}\hat{d}} = \delta_{\hat{d}\hat{a}}c_{\hat{b}\hat{c}}{}^{\hat{a}}$. The vector $[e_{\hat{b}}, e_{\hat{c}}]$ represents the commutator of the triad vectors $e_{\hat{b}}$ and $e_{\hat{c}}$, having the components:

$$[e_{\hat{b}}, e_{\hat{c}}]^{\tilde{\imath}} = e^{\tilde{\jmath}}_{\hat{b}}\partial_{\tilde{\jmath}}e^{\tilde{\imath}}_{\hat{c}} - e^{\tilde{\jmath}}_{\hat{c}}\partial_{\tilde{\jmath}}e^{\tilde{\imath}}_{\hat{b}}. \qquad (2.23)$$

More details on the connection between Eqs. (2.4) and (2.20) can be found in Appendix B. Since the numerical implementations of hyperbolic equations in advective form are in general non-conservative [107], we will not consider the advective form (2.20) of the Boltzmann equation further in this paper.

B. Conservative form

The Boltzmann equation in advective form (2.20) hides the conservation laws both analytically and numerically. Following Ref. [48], Eq. (2.20) can be written in conservative form as follows:

$$\frac{\partial f}{\partial t} + \frac{1}{\sqrt{g}}\frac{\partial}{\partial x^{\tilde{\imath}}}\left(\frac{p^{\hat{a}}}{m}e^{\tilde{\imath}}_{\hat{a}}f\sqrt{g}\right)$$

$$+ \frac{\partial}{\partial p^{\hat{a}}}\left[\left(F^{\hat{a}} - \frac{1}{m}\Gamma^{\hat{a}}{}_{\hat{b}\hat{c}}p^{\hat{b}}p^{\hat{c}}\right)f\right] = J[f]. \quad (2.24)$$

The derivation of Eq. (2.24) is presented in Appendix C.

Multiplying Eq. (2.24) by $p^{\hat{a}_1}p^{\hat{a}_2}\cdots p^{\hat{a}_s}$ and integrating over the momentum space, it can be shown that:

$$\partial_t M^{\hat{a}_1\hat{a}_2\ldots\hat{a}_s} + \frac{1}{m}\nabla_{\hat{b}}M^{\hat{b}\hat{a}_1\ldots\hat{a}_s}$$

$$= \frac{1}{m}(F^{\hat{a}_1}M^{\hat{a}_2\ldots\hat{a}_s} + \ldots) + \mathcal{S}^{\hat{a}_1\hat{a}_2\ldots\hat{a}_s}, \quad (2.25)$$

where the right-hand side parenthesis is symmetric with respect to the indices $\hat{a}_1, \ldots\hat{a}_s$, containing s terms. The s'th order moment of f is defined in Eq. (2.19), while the covariant derivative $\nabla_{\hat{a}}$ acts on the tensor $M^{\hat{a}_1\ldots\hat{a}_s}$ as follows:

$$\nabla_{\hat{a}}M^{\hat{a}_1\ldots\hat{a}_s} = e^{\tilde{\imath}}_{\hat{a}}\partial_{\tilde{\imath}}M^{\hat{a}_1\ldots\hat{a}_s} + \Gamma^{\hat{a}_1}{}_{\hat{b}\hat{a}}M^{\hat{b}\hat{a}_2\ldots\hat{a}_s}$$

$$+ \Gamma^{\hat{a}_2}{}_{\hat{b}\hat{a}}M^{\hat{a}_1\hat{b}\hat{a}_3\ldots\hat{a}_s} + \cdots + \Gamma^{\hat{a}_s}{}_{\hat{b}\hat{a}}M^{\hat{a}_1\hat{a}_2\ldots\hat{a}_{s-1}\hat{b}}. \quad (2.26)$$

The source term $\mathcal{S}^{\hat{a}_1\hat{a}_2\ldots\hat{a}_s}$ is defined as:

$$\mathcal{S}^{\hat{a}_1\hat{a}_2\ldots\hat{a}_s} = \int d^3\hat{p}\, J[f]\, p^{\hat{a}_1}\cdots p^{\hat{a}_s}. \qquad (2.27)$$
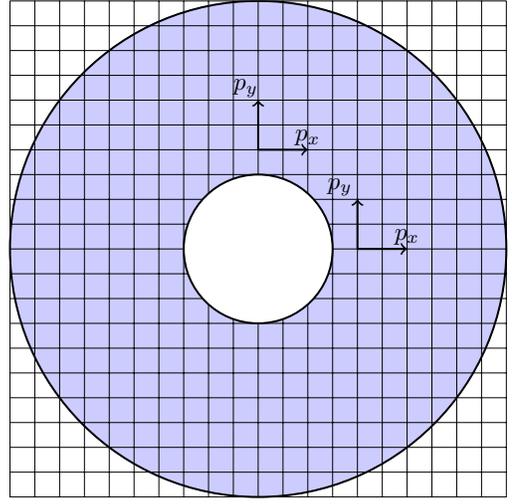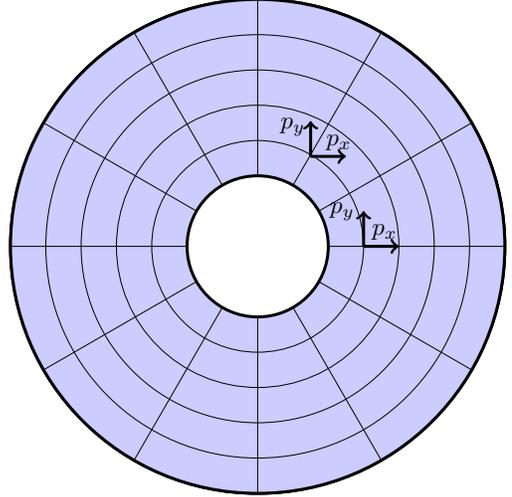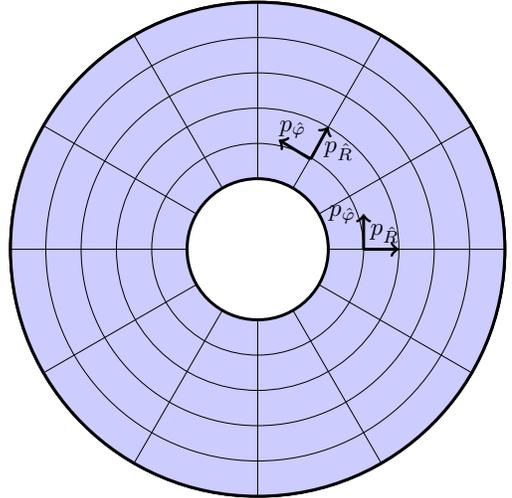
FIG. 1. Circular Couette flow setup. (a) Cartesian grid and momentum space decomposition along the Cartesian axes; (b) Cylindrical grid and momentum space decomposition along the Cartesian axes; (c) Cylindrical grid and momentum space decomposition adapted to the curvilinear coordinates.

It is now easy to derive the macroscopic fluid equations:

$$\frac{Dn}{Dt} + n(\nabla \cdot \boldsymbol{u}) = 0, \tag{2.28a}$$

$$\rho \frac{Du^{\hat{a}}}{Dt} = nF^{\hat{a}} - \nabla_{\hat{b}} T^{\hat{a}\hat{b}}, \tag{2.28b}$$

$$n \frac{De}{Dt} + \nabla_{\hat{a}} q^{\hat{a}} + T^{\hat{a}\hat{b}} \nabla_{\hat{a}} u_{\hat{b}} = 0, \tag{2.28c}$$

where $D/Dt = \partial_t + u^{\hat{a}} \nabla_{\hat{a}}$ is the material derivative, while $e = \frac{3}{2} T$ is the internal energy per constituent. The relations between the distribution function f and the particle number density n, macroscopic velocity $u^{\hat{a}}$, stress tensor $T^{\hat{a}\hat{b}}$ and heat flux $q^{\hat{a}}$ are listed below:

$$n = \int d^3 \hat{p} \, f, \tag{2.29a}$$

$$u^{\hat{a}} = \frac{1}{\rho} \int d^3 \hat{p} \, f \, p^{\hat{a}}, \tag{2.29b}$$

$$T^{\hat{a}\hat{b}} = \int d^3 \hat{p} \, f \, \frac{\xi^{\hat{a}} \xi^{\hat{b}}}{m}, \tag{2.29c}$$

$$q^{\hat{a}} = \int d^3 \hat{p} \, f \, \frac{\boldsymbol{\xi}^2}{2m} \frac{\xi^{\hat{a}}}{m}, \tag{2.29d}$$

where $\rho = mn$, $\xi^{\hat{a}} = p^{\hat{a}} - mu^{\hat{a}}$, and $\boldsymbol{\xi}^2 = \delta_{\hat{a}\hat{b}} \xi^{\hat{a}} \xi^{\hat{b}}$. The total number of particles N_{tot} inside the simulation domain can be computed using:

$$N_{\text{tot}} = \int d^3 x \sqrt{g} n = \int d^3 x \int d^3 \hat{p} \widetilde{f}. \tag{2.30}$$

C. Chapman-Enskog Expansion

In order to illustrate the application of the Chapman-Enskog procedure, we consider the Bhatnaghar-Gross-Krook (BGK) single-time approximation for the collision term:

$$J[f] = -\frac{1}{\tau}(f - f^{(\text{eq})}). \tag{2.31}$$

We note that this simplified implementation of the collision term has several drawbacks, including the fact that the Prandtl number Pr is fixed at 1, while its value for, e.g., hard sphere molecules is $2/3$. This drawback (and others) can be corrected, i.e. by employing the Shakhov extension of the BGK collision term [108–112]. In the interest of simplicity, in this paper we only consider the BGK implementation of the collision term, since the generalization of our proposed scheme to more complicated formulations of $J[f]$ is straightforward.

The "simplified version" of the Chapman-Enskog expansion entails treating τ and the difference $\delta f = f - f^{(\text{eq})}$ as small quantities, such that $\delta f/\tau$ is of the same order as the left-hand side of Eq. (2.24) when $f \simeq f^{(\text{eq})}$.

Ignoring higher-order terms, the following expression is obtained for δf:

$$\delta f = -\tau \left\{ \frac{\partial f^{(\text{eq})}}{\partial t} + \frac{1}{\sqrt{g}} \frac{\partial}{\partial x^{\tilde{i}}} \left(\frac{p^{\hat{a}}}{m} e_{\hat{a}}^{\tilde{i}} f^{(\text{eq})} \sqrt{g} \right) \right.$$
$$\left. + \frac{\partial}{\partial p^{\hat{a}}} \left[\left(F^{\hat{a}} - \frac{1}{m} \Gamma^{\hat{a}}_{\hat{b}\hat{c}} p^{\hat{b}} p^{\hat{c}} \right) f^{(\text{eq})} \right] \right\}. \tag{2.32}$$

The collision invariants $\psi \in \{1, p^{\hat{a}}, \boldsymbol{p}^2/2m\}$ are preserved only if:

$$\int d^3 \hat{p} \, \delta f = \int d^3 \hat{p} \, \delta f \, p^{\hat{a}} = \int d^3 \hat{p} \, \delta f \, \frac{\boldsymbol{p}^2}{2m} = 0, \tag{2.33}$$

where $\boldsymbol{p}^2 \equiv \delta_{\hat{a}\hat{b}} p^{\hat{a}} p^{\hat{b}}$ represents the squared norm of $\boldsymbol{p}$ written in terms of its tetrad components.

The deviation from equilibrium δf induces a deviation $\delta T^{\hat{a}\hat{b}}$ from the equilibrium stress-tensor, as well as a heat flux:

$$T^{\hat{a}\hat{b}} = \delta^{\hat{a}\hat{b}} P + \delta T^{\hat{a}\hat{b}}, \qquad q^{\hat{a}} = \delta q^{\hat{a}}, \tag{2.34}$$

where $P = nT$ is the ideal gas pressure. The non-equilibrium quantities $\delta T^{\hat{a}\hat{b}}$ and $\delta q^{\hat{a}}$ can be obtained as follows:

$$\delta T^{\hat{a}\hat{b}} = \int d^3 \hat{p} \, \delta f \frac{\xi^{\hat{a}} \xi^{\hat{b}}}{m} = \int d^3 \hat{p} \, \delta f \frac{p^{\hat{a}} p^{\hat{b}}}{m}, \tag{2.35a}$$

$$\delta q^{\hat{a}} = \int d^3 \hat{p} \, \delta f \frac{\boldsymbol{\xi}^2}{2m} \frac{\xi^{\hat{a}}}{m} = \int d^3 \hat{p} \, \delta f \frac{\boldsymbol{p}^2}{2m} \frac{p^{\hat{a}}}{m} - u_{\hat{b}} \delta T^{\hat{a}\hat{b}}. \tag{2.35b}$$

Substituting Eq. (2.32) into Eq. (2.35a) yields:

$$\delta T^{\hat{a}\hat{b}} = -\tau$$
$$\times \left[\frac{1}{m} \partial_t M_{\text{eq}}^{\hat{a}\hat{b}} + \frac{1}{m^2} \nabla_{\hat{c}} M_{\text{eq}}^{\hat{a}\hat{b}\hat{c}} - n(u^{\hat{a}} F^{\hat{b}} + u^{\hat{b}} F^{\hat{a}}) \right], \tag{2.36a}$$

while the heat flux can be obtained as:

$$\delta q^{\hat{a}} + u_{\hat{b}} \delta T^{\hat{a}\hat{b}} = -\tau \left\{ \delta_{\hat{c}\hat{d}} \left(\frac{1}{2m^2} \partial_t M_{\text{eq}}^{\hat{a}\hat{c}\hat{d}} + \frac{1}{2m^3} \nabla_{\hat{b}} M_{\text{eq}}^{\hat{a}\hat{b}\hat{c}\hat{d}} \right) \right.$$
$$\left. - \frac{5nT}{2m} F^{\hat{a}} - \frac{n}{2} [F^{\hat{a}} \boldsymbol{u}^2 + 2u^{\hat{a}} (\boldsymbol{u} \cdot \boldsymbol{F})] \right\}. \tag{2.36b}$$

The time derivatives appearing in Eqs. (2.36a) and (2.36b) can be eliminated since, at first order, n, $u^{\hat{a}}$ and T satisfy the Euler equations, obtained by setting $T^{\hat{a}\hat{b}} = \delta^{\hat{a}\hat{b}} P$ and $q^{\hat{a}} = 0$ in Eq. (2.28):

$$\frac{Dn}{Dt} + n \nabla_{\hat{a}} u^{\hat{a}} = 0,$$

$$\rho \frac{Du^{\hat{a}}}{Dt} + \nabla^{\hat{a}} P = nF^{\hat{a}},$$

$$n \frac{De}{Dt} + P \nabla_{\hat{a}} u^{\hat{a}} = 0. \tag{2.37}$$

Using the explicit expressions (2.18) for the moments of $f^{(\mathrm{eq})}$, a straightforward but tedious calculation shows that $\delta T^{\hat{a}\hat{b}}$ and $\delta q^{\hat{a}}$ can be expressed as:

$$\delta T^{\hat{a}\hat{b}} = -\mu\left(\nabla^{\hat{a}}u^{\hat{b}} + \nabla^{\hat{b}}u^{\hat{a}} - \frac{2}{3}\delta^{\hat{a}\hat{b}}\nabla_{\hat{c}}u^{\hat{c}}\right), \quad (2.38\text{a})$$

$$\delta q^{\hat{a}} = -\kappa\nabla^{\hat{a}}T, \tag{2.38b}$$

where the dynamic viscosity μ and the coefficient of thermal conductivity κ are given by:

$$\mu = \tau P, \qquad \kappa = \frac{5}{2m}\tau P. \tag{2.38c}$$

III. NUMERICAL SCHEME

The aim of this Section is to derive numerical implementations of Eq. (2.24) which are manifestly conservative. To this end, we also introduce the following form of the Boltzmann equation, obtained by multiplying Eq. (2.24) with $\sqrt{g}$:

$$\frac{\partial \widetilde{f}}{\partial t} + \frac{\partial}{\partial x^{\widetilde{\imath}}}\left(\frac{p^{\hat{a}}}{m}e_{\hat{a}}^{\widetilde{\imath}}\widetilde{f}\right) + \frac{\partial}{\partial p^{\hat{a}}}\left[\left(F^{\hat{a}} - \frac{1}{m}\Gamma^{\hat{a}}_{\ \hat{b}\hat{c}}p^{\hat{b}}p^{\hat{c}}\right)\widetilde{f}\right]$$
$$= J[f]\sqrt{g}, \quad (3.1)$$

where the following notation was introduced:

$$\widetilde{f} = f\sqrt{g}. \tag{3.2}$$

The advantage of the formulation (3.1) is that the spatial derivatives corresponding to the advection term do not have any position-dependent prefactors, such that a conservative numerical implementation is straightforward. The disadvantage of this formulation is that performing the evolution and advection at the level of $\widetilde{f}$ can introduce fluctuations in the numerical solution, which prevent, e.g., a solution of the form $f = \text{const}$ to be exactly achieved [107]. For definiteness, we shall refer to the formulation starting from Eq. (3.1) as the $\widetilde{f}$ formulation.

Our second (and preferred) implementation is inspired from the methodology proposed in Refs. [113, 114] and starts again from the Boltzmann equation in the form presented in Eq. (2.24). For simplicity, we restrict the construction of the numerical scheme to the case when $\sqrt{g}$ is separable, i.e.:

$$\sqrt{g} = \sqrt{g_{\widetilde{1}}g_{\widetilde{2}}g_{\widetilde{3}}}, \tag{3.3}$$

where the factors $g_{\widetilde{\imath}} \equiv g_{\widetilde{\imath}}(x^{\widetilde{\imath}})$ each depend only on one coordinate ($x^{\widetilde{\imath}}$). The above assumption is valid for both examples considered in this paper (circular Couette flow and flow through the gradually expanding channel). An extension of the present methodology to a non-separable metric determinant is straightforward but for simplicity, we do not discuss this case here. The main idea is to define a new set of coordinates, $\chi^{\widetilde{\imath}}$, such that the $1/\sqrt{g}$

TABLE I. Butcher tableau for the third-order Runge-Kutta time-stepping procedure described in Eq. (3.7).

0			
1	1		
1/2	1/4	1/4	
	1/6	1/6	2/3

factor in front of the spatial derivatives in Eq. (2.24) is absorbed into the derivative. This can be achieved when $\chi^{\widetilde{\imath}}$ is introduced as follows:

$$\chi^{\widetilde{\imath}} = \int^{x^{\widetilde{\imath}}} dx^{\widetilde{\imath}}\sqrt{g_{\widetilde{\imath}}}, \tag{3.4}$$

such that $\partial\chi^{\widetilde{\imath}}/\partial x^{\widetilde{\imath}} = \sqrt{g_{\widetilde{\imath}}}$. The lower integration end is not relevant, since only differences of the form $\delta\chi^{\widetilde{\imath}}$ appear in the numerical implementation and is thus left arbitrary. The above definition for $\chi^{\widetilde{\imath}}$ is inspired from Refs. [113] and [114], where a similar definition was employed for the cylindrical and spherical coordinate systems, respectively (more details will be given in Sec. V). The advantage of performing the derivative with respect to $\chi^{\widetilde{\imath}}$ is that the numerical procedure can be constructed to exactly preserve (up to machine precision) the conservation of the total number of particles, as will be shown in Subsec. III D. For definiteness, we shall refer to the formulation based on the change of variables in the spatial derivative given by Eq. (3.4) as the χ formulation.

For the flows considered in this paper, Eqs. (3.1) and (2.24) can be put in the form:

$$\frac{\partial F}{\partial t} + \sum_{\widetilde{\imath}}\frac{\partial(V^{\widetilde{\imath}}F)}{\partial\chi^{\widetilde{\imath}}} = S, \tag{3.5}$$

where the source term S contains the inertial forces (involving the momentum derivatives of f) and the collision term. In the $\widetilde{f}$ formulation (3.1), $F = \widetilde{f} \equiv f\sqrt{g}$ and $\chi^{\widetilde{\imath}} = x^{\widetilde{\imath}}$ is the coordinate on direction $\widetilde{\imath}$. In the χ formulation (2.24), $F = f$ and $\chi^{\widetilde{\imath}}$ is defined in Eq. (3.4). The advection velocity $V^{\widetilde{\imath}}$ is in general point dependent and is given in the $\widetilde{f}$ formulation by $V^{\widetilde{\imath}} = \frac{p^{\hat{a}}}{m}e_{\hat{a}}^{\widetilde{\imath}}$, while in the χ formulation, it has the expression $V^{\widetilde{\imath}} = \sqrt{g_{\widetilde{\imath}}}\frac{p^{\hat{a}}}{m}e_{\hat{a}}^{\widetilde{\imath}}$.

A. Time-stepping

Equation (3.5) can be put in the following form

$$\partial_t F = L[F], \tag{3.6}$$

where $L[F]$ is an integro-differential operator with respect to the spatial coordinates acting on F. Let us consider an equidistant discretization of the time variable, such that at step ℓ, the value of the time coordinate is $t_\ell = \ell\delta t$ (we assume that $t_0 = 0$ is the initial
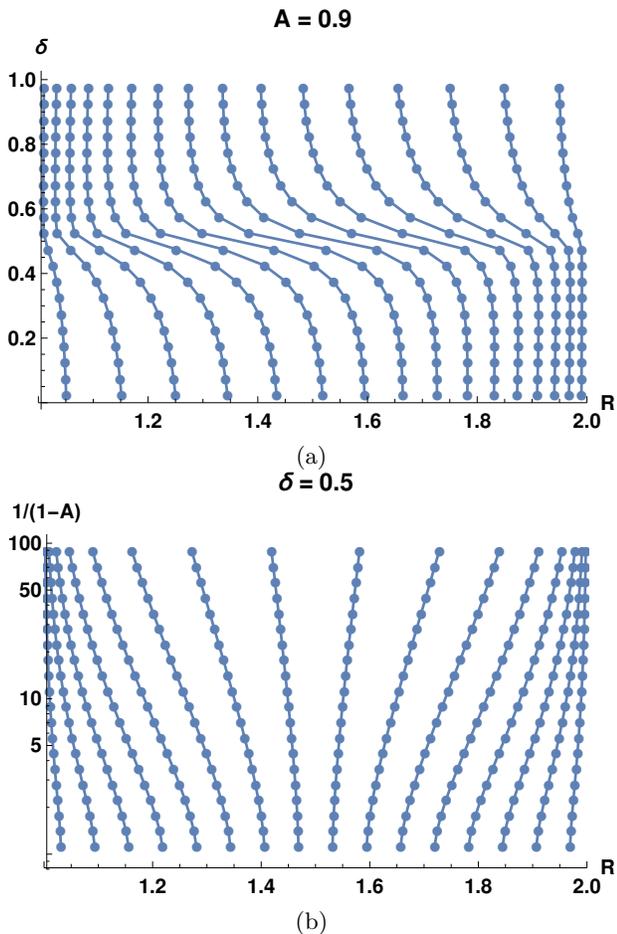
FIG. 2. Effect of grid stretching on 16 points between $R_{\text{in}} = 1$ and $R_{\text{out}} = 2$. (a) The parameter δ controls the positioning of the stretching center (i.e. the point where the grid is the coarsest). (b) The parameter A contains the amplitude of the stretching, with $A = 0$ and $A = 1$ corresponding to equidistant and infinitely-stretched points, respectively.

time). If $F_\ell \equiv F(t_\ell)$ at time $t = t_\ell$ is known, its value at $t_{\ell+1} = t_\ell + \delta t$ can be obtained using the third-order total variation diminishing (TVD) Runge-Kutta method described in Refs. [81, 82, 84–87]:

$$
\begin{aligned}
F_\ell^{(1)} &= F_\ell + \delta t\, L[F_\ell], \\
F_\ell^{(2)} &= \frac{3}{4} F_\ell + \frac{1}{4} F_\ell^{(1)} + \frac{1}{4}\delta t\, L[F_\ell^{(1)}], \\
F_{\ell+1} &= \frac{1}{3} F_\ell + \frac{2}{3} F_\ell^{(2)} + \frac{2}{3}\delta t\, L[F_\ell^{(2)}].
\end{aligned} \tag{3.7}
$$

The Butcher tableau [115] corresponding to this scheme is given in Table I.

B. Coordinate stretching

As pointed out in Refs. [40, 65], the correct recovery of the Knudsen layer in wall-bounded flows requires a substantially finer mesh near the walls than in the bulk of the channel. This can be efficiently achieved by performing a coordinate stretching such that the resulting grid is finer near the boundaries and coarser in the interior of the channel. Assuming that the walls are orthogonal to the $x^{\widetilde{1}}$ direction, we consider the following coordinate transformation:

$$
x^{\widetilde{1}}(\eta) = x^{\widetilde{1}}_{\text{left}} + (x^{\widetilde{1}}_{\text{right}} - x^{\widetilde{1}}_{\text{left}})\left(\delta + \frac{A_0}{A}\tanh\eta\right), \quad (3.8)
$$

where $x^{\widetilde{1}}_{\text{left}}$ and $x^{\widetilde{1}}_{\text{right}}$ are the coordinates of the left and right domain boundaries, respectively. The constants δ and A are free parameters, while A_0 is chosen as:

$$
A_0 = \max(\delta, 1 - \delta). \tag{3.9}
$$

The above definition of A_0 allows the range of δ to be $\delta \in [0, 1]$, while $A \in (0, 1)$. As illustrated in Fig. 2(a), the parameter δ controls the position of the stretching center (i.e. when $\eta = 0$), such that when $\delta = 0$ and 1, the coarsest region is near the left and right boundary, respectively.

The parameter A controls the grid stretching, such that as $A \to 0$, the grid becomes equidistant, while when $A \to 1$, the grid becomes infinitely stretched near the stretching center at $x^{\widetilde{1}} = x^{\widetilde{1}}_{\text{left}}(1 - \delta) + x^{\widetilde{1}}_{\text{right}}\delta$. This is illustrated in Fig. 2(b).

The range of η is $\eta \in [\eta_{\text{left}}, \eta_{\text{right}}]$, where η_{left} and η_{right} can be found by setting $x^{\widetilde{1}} = x^{\widetilde{1}}_{\text{left}}$ and $x^{\widetilde{1}} = x^{\widetilde{1}}_{\text{right}}$ in Eq. (3.8):

$$
\eta_{\text{left}} = -\text{arctanh}\frac{A\delta}{A_0}, \qquad \eta_{\text{right}} = \text{arctanh}\frac{A(1 - \delta)}{A_0}. \tag{3.10}
$$

In the special case when $\delta = 0.5$, the range of η is $\eta \in [-\text{arctanh}A, \text{arctanh}A]$, since $A_0 = 0.5$.

In the current formulation, the grid stretching is a coordinate transformation which changes the line element (2.2). In particular, the Boltzmann equation can be re-derived with respect to the stretched coordinate η and its associated momentum $p^{\hat{\eta}}$ and a different conservative formulation is obtained compared to the case when the grid is not stretched. This will be further discussed in the context of the circular Couette flow in Sec. V.

C. Implementation of advection

The examples considered in this paper are either one-dimensional (the circular Couette flow discussed in Sec. V) or two-dimensional (the gradually expanding channel discussed in Sec. VI), hence the flow can always be assumed to be homogeneous with respect to

TABLE II. Limiting values for the weighting factors $\overline{\omega}_q$ (3.14) employed in the computation of the WENO-5 flux (3.12).

	$\overline{\omega}_1$	$\overline{\omega}_2$	$\overline{\omega}_3$
$\sigma_1 = \sigma_2 = \sigma_3$	0.1	0.6	0.3
$\sigma_2 = \sigma_3 = 0$	0	2/3	1/3
$\sigma_3 = \sigma_1 = 0$	1/4	0	3/4
$\sigma_1 = \sigma_2 = 0$	1/7	6/7	0
$\sigma_1 = 0$	1	0	0
$\sigma_2 = 0$	0	1	0
$\sigma_3 = 0$	0	0	1

the z axis (we will take advantage of this simplification in Sec. IV A, where the z degree of freedom of the momentum space will be eliminated by introducing reduced distribution functions). The simulation domain is thus divided into $N^{\widetilde{1}} \times N^{\widetilde{2}}$ cells centered on $\boldsymbol{x}_{s,p} = (x_s^{\widetilde{1}}, x_p^{\widetilde{2}})$ $(1 \leq s \leq N^{\widetilde{1}}, 1 \leq p \leq N^{\widetilde{2}})$. Each cell (s,p) has four interfaces, located at $\boldsymbol{x}_{s+1/2,p}$, $\boldsymbol{x}_{s-1/2,p}$, $\boldsymbol{x}_{s,p+1/2}$ and $\boldsymbol{x}_{s,p-1/2}$. The domain boundary consists of the outer interfaces of the outer cells, having coordinates $\boldsymbol{x}_{\text{left}} = \boldsymbol{x}_{1/2,p}$, $\boldsymbol{x}_{\text{right}} = \boldsymbol{x}_{N+1/2,p}$, $\boldsymbol{x}_{\text{bottom}} = \boldsymbol{x}_{s,1/2}$ and $\boldsymbol{x}_{\text{top}} = \boldsymbol{x}_{s,M+1/2}$. With this notation, the advection part of Eq. (3.5) can be written as follows:

$$
\sum_{\widetilde{i}} \left(\frac{\partial (V^{\widetilde{i}} F)}{\partial \chi^{\widetilde{i}}} \right)_{s,p} \simeq
$$

$$
\frac{V_{s+1/2,p}^{\widetilde{1}} \mathcal{F}_{\widetilde{1};s+1/2,p} - V_{s-1/2,p}^{\widetilde{1}} \mathcal{F}_{\widetilde{1};s-1/2,p}}{\chi_{s+1/2}^{\widetilde{1}} - \chi_{s-1/2}^{\widetilde{1}}}
$$

$$
+ \frac{V_{s,p+1/2}^{\widetilde{2}} \mathcal{F}_{\widetilde{2};s+1/2,p} - V_{s,p-1/2}^{\widetilde{2}} \mathcal{F}_{\widetilde{2};s,p-1/2}}{\chi_{p+1/2}^{\widetilde{2}} - \chi_{p-1/2}^{\widetilde{2}}}, \quad (3.11)
$$

where directional splitting was applied, i.e. the advection along each direction $x^{\widetilde{i}}$ is performed independently. The quantities bearing the indices $s+1/2, p$ are evaluated at the interfaces between cells $(s+1, p)$ and (s, p), etc. The fluxes $\mathcal{F}_{\widetilde{1};s\pm1/2,p}$ correspond to the advection of F along $V_{s\pm1/2,p}^{\widetilde{1}}$ with respect to the coordinate $\chi^{\widetilde{1}}$, while the fluxes $\mathcal{F}_{\widetilde{2};s,p\pm1/2}$ correspond to the advection of F along $V_{s;p\pm1/2}^{\widetilde{2}}$ with respect to the coordinate $\chi^{\widetilde{2}}$. These fluxes are calculated using the fifth-order weighted essentially non-oscillatory (WENO-5) scheme [45, 78–82]. We employ the WENO-5 scheme as described in Ref. [16, 82], where the addition of a small quantity ε in order to avoid division by 0 operations is not required. For definiteness, we give below the procedure for constructing the flux $\mathcal{F}_{\widetilde{1};s+1/2,p}$ for the case when $V_{s+1/2,p}^{\widetilde{1}} > 0$:

$$
\mathcal{F}_{\widetilde{1};s+1/2,p} = \overline{\omega}_1 \mathcal{F}_{\widetilde{1};s+1/2,p}^1
$$
$$
+ \overline{\omega}_2 \mathcal{F}_{\widetilde{1};s+1/2,p}^2 + \overline{\omega}_3 \mathcal{F}_{\widetilde{1};s+1/2,p}^3, \quad (3.12)
$$

where the interpolating functions $\mathcal{F}_{\widetilde{1};s+1/2,p}^q$ $(q = 1, 2, 3)$ are given by:

$$
\mathcal{F}_{\widetilde{1};s+1/2,p}^1 = \frac{1}{3} F_{s-2,p} - \frac{7}{6} F_{s-1,p} + \frac{11}{6} F_{s,p},
$$

$$
\mathcal{F}_{\widetilde{1};s+1/2,p}^2 = -\frac{1}{6} F_{s-1,p} + \frac{5}{6} F_{s,p} + \frac{1}{3} F_{s+1,p},
$$

$$
\mathcal{F}_{\widetilde{1};s+1/2,p}^3 = \frac{1}{3} F_{s,p} + \frac{5}{6} F_{s+1,p} - \frac{1}{6} F_{s+2,p}, \quad (3.13)
$$

while the weighting factors $\overline{\omega}_q$ are defined as:

$$
\overline{\omega}_q = \frac{\widetilde{\omega}_q}{\widetilde{\omega}_1 + \widetilde{\omega}_2 + \widetilde{\omega}_3}, \qquad \widetilde{\omega}_q = \frac{\delta_q}{\sigma_q^2}. \quad (3.14)
$$

The ideal weights δ_q are:

$$
\delta_1 = 1/10, \qquad \delta_2 = 6/10, \qquad \delta_3 = 3/10, \quad (3.15)
$$

while the indicator of smoothness functions σ_q are given by:

$$
\sigma_1 = \frac{13}{12} (F_{s-2,p} - 2F_{s-1,p} + F_{s,p})^2
$$
$$
+ \frac{1}{4} (F_{s-2,p} - 4F_{s-1,p} + 3F_{s,p})^2,
$$
$$
\sigma_2 = \frac{13}{12} (F_{s-1,p} - 2F_{s,p} + F_{s+1,p})^2
$$
$$
+ \frac{1}{4} (F_{s-1,p} - F_{s+1,p})^2,
$$
$$
\sigma_3 = \frac{13}{12} (F_{s,p} - 2F_{s+1,p} + F_{s+2,p})^2
$$
$$
+ \frac{1}{4} (3F_{s,p} - 4F_{s+1,p} + F_{s+2,p})^2. \quad (3.16)
$$

It is customary to add in the denominators of $\widetilde{\omega}_q$ a small quantity ε (usually taken as 10^{-6}) to avoid division by 0 operations. However, as pointed out in Ref. [86], the effect of this alteration on the indicators of smoothness is strongly dependent on the given problem, since ε becomes a dimensional quantity. Furthermore, the accuracy of the resulting scheme depends on the value of ε. Since at higher orders, the distribution functions corresponding to large velocities can have values which are significantly smaller than those for smaller velocities, we cannot predict the effect of employing a unitary value for ε for the advection of all distribution functions. Therefore, we prefer to follow Refs. [16, 82] and compute the limiting values of $\overline{\omega}_q$ when one, two or all three of the indicators of smoothness vanish as indicated in Table II.

D. Particle number conservation

The Boltzmann equation implies the fluid equations (2.28), which ensure that the total number of particles N_{tot} (2.30) per unit length, the total momentum $\mathcal{P}$ and the total energy $\mathcal{E}$ are conserved within the fluid. However, the gas-wall interaction can induce changes in

these parameters. In this paper, we will consider diffuse-reflection boundary conditions for impermeable walls, such that N_{tot} is preserved at all times, while $\mathcal{P}$ and $\mathcal{E}$ are allowed to vary. Thus, in this Subsection, we will only consider the conservation of N_{tot}.

After the discretization of space and time, the only changes that can be induced in $N_{\text{tot}}(t)$ are due to the operator $L[F]$. In the following, the $\widetilde{f}$ and χ formulations will be treated separately.

In the $\widetilde{f}$ formulation, $F = \widetilde{f} = f\sqrt{g}$ and the time evolution of N_{tot} (2.30) can be obtained by integrating Eq. (3.6) with respect to the momentum space and over the entire fluid domain:

$$\partial_t N_{\text{tot}}(t) = \int d^3\widetilde{x} \int d^3\hat{p}\, L[\widetilde{f}]. \qquad (3.17)$$

The momentum space integral of the source term in Eq. (3.5) vanishes, since 1 is a collision invariant, while the zeroth-order moment of the force term is zero. For simplicity, an equidistant grid is considered, such that Eq. (3.17) reduces to:

$$\partial_t N_{\text{tot}}(t) = -\int d^3\hat{p} \int d^3\widetilde{x} \sum_{\widetilde{i}} \frac{\partial(V^{\widetilde{i}} f\sqrt{g})}{\partial x^{\widetilde{i}}}, \qquad (3.18)$$

where we took into account that $\chi^{\widetilde{i}} = x^{\widetilde{i}}$ in the $\widetilde{f}$ formulation. The integration domain can be split into cells and the advection term, replaced via Eq. (3.11), can be considered constant within each cell, such that Eq. (3.18) becomes simply:

$$\partial_t N_{\text{tot}}(t) = -\delta z \int d^3\hat{p} \sum_{s=1}^{N^{\widetilde{2}}} \sum_{p=1}^{N^{\widetilde{2}}} \left[\delta x^{\widetilde{2}}(\widetilde{\mathcal{F}}_{\widetilde{1};s+1/2,p} \right.$$
$$\left. -\widetilde{\mathcal{F}}_{\widetilde{1};s-1/2,p}) + \delta x^{\widetilde{1}}(\widetilde{\mathcal{F}}_{\widetilde{2};s,p+1/2} - \widetilde{\mathcal{F}}_{\widetilde{2};s,p-1/2}) \right], \quad (3.19)$$

where δz represents the height of the fluid domain and the notation $\widetilde{\mathcal{F}}_{\hat{a};s+1/2,p}$ indicates that the fluxes are computed by replacing $F_{s,p}$ with $\widetilde{f}_{s,p} = f_{s,p}\sqrt{g_{s,p}}$ in Eq. (3.12). The bulk terms cancel out and $\partial_t N_{\text{tot}}(t)$ reduces to:

$$\partial_t N_{\text{tot}}(t) = -\delta z \int d^3\hat{p} \left[\sum_{p=1}^{N^{\widetilde{2}}} \delta x^{\widetilde{2}}(\widetilde{\mathcal{F}}_{\widetilde{1};N^{\widetilde{1}}+1/2,p} - \widetilde{\mathcal{F}}_{\widetilde{1};1/2,p}) \right.$$
$$\left. + \sum_{s=1}^{N^{\widetilde{1}}} \delta x^{\widetilde{1}}(\widetilde{\mathcal{F}}_{\widetilde{2};s,N^{\widetilde{2}}+1/2} - \widetilde{\mathcal{F}}_{\widetilde{2};s,1/2}) \right]. \quad (3.20)$$

Thus, the conservation of the total number of particles is conditioned by the requirement that the momentum-space integrals of the fluxes at the outer interfaces of the outer cells cancel. Ensuring that these momentum space integrals vanish is the subject of Subsec. III F, which is dedicated to the discussion of the implementation of the boundary conditions.

In the case of the χ approach, $F = f$ while $\sqrt{g}$ appears explicitly in (3.17):

$$\partial_t N_{\text{tot}}(t) = \int d^3\widetilde{x} \sqrt{g} \int d^3\hat{p}\, L[f]. \qquad (3.21)$$

As before, the momentum space integral of the source term vanishes and the only contributions to $\partial_t N_{\text{tot}}(t)$ come from the advection part of $L[f]$. Treating again the advection terms as constants over the domain cells, the integral of $\sqrt{g}$ can be performed over each cell by keeping in mind the definition of $\chi^{\widetilde{i}}$ (3.4), such that:

$$\int_{(s,p)} d^3\widetilde{x} \sqrt{g} \frac{V^{\widetilde{1}}_{s+1/2,p}\mathcal{F}_{\widetilde{1};s+1/2,p} - V^{\widetilde{1}}_{s-1/2,p}\mathcal{F}_{\widetilde{1};s-1/2,p}}{\delta\chi^{\widetilde{1}}_s}$$
$$= \delta z \delta\chi^{\widetilde{2}}_p(V^{\widetilde{1}}_{s+1/2,p}\mathcal{F}_{\widetilde{1};s+1/2,p} - V^{\widetilde{1}}_{s-1/2,p}\mathcal{F}_{\widetilde{1};s-1/2,p}),$$
$$\int_{(s,p)} d^3\widetilde{x} \sqrt{g} \frac{V^{\widetilde{2}}_{s,p+1/2}\mathcal{F}_{\widetilde{2};s,p+1/2} - V^{\widetilde{2}}_{s,p-1/2}\mathcal{F}_{\widetilde{2};s,p-1/2}}{\delta\chi^{\widetilde{2}}_p}$$
$$= \delta z \delta\chi^{\widetilde{1}}_s(V^{\widetilde{2}}_{s,p+1/2}\mathcal{F}_{\widetilde{2};s,p+1/2} - V^{\widetilde{2}}_{s,p-1/2}\mathcal{F}_{\widetilde{2};s,p-1/2}),$$
$$\qquad (3.22)$$

where $\delta\chi^{\widetilde{1}}_s = \chi^{\widetilde{1}}_{s+1/2} - \chi^{\widetilde{1}}_{s-1/2}$ and $\delta\chi^{\widetilde{2}}_p = \chi^{\widetilde{2}}_{p+1/2} - \chi^{\widetilde{2}}_{p-1/2}$. The bulk terms again cancel and Eq. (3.21) becomes:

$$\partial_t N_{\text{tot}}(t) = -\delta z \int d^3\hat{p}$$
$$\left[\sum_{p=1}^{N^{\widetilde{2}}} \delta\chi^{\widetilde{2}}_p(V^{\widetilde{1}}_{N^{\widetilde{1}}+1/2,p}\mathcal{F}_{\widetilde{1};N^{\widetilde{1}}+1/2,p} - V^{\widetilde{1}}_{1/2,p}\mathcal{F}_{\widetilde{1};1/2,p}) \right.$$
$$\left. + \sum_{s=1}^{N^{\widetilde{1}}} \delta\chi^{\widetilde{1}}_s(V^{\widetilde{2}}_{s,N^{\widetilde{2}}+1/2}\mathcal{F}_{\widetilde{2};s,N^{\widetilde{2}}+1/2} - V^{\widetilde{2}}_{s,1/2}\mathcal{F}_{\widetilde{2};s,1/2}) \right].$$
$$\qquad (3.23)$$

As in the $\widetilde{f}$ formulation, the conservation of the total number of particles relies on the exact cancellation of the numerical fluxes through the outer interfaces of the outer cells of the fluid domain.

E. Order of advection scheme

Let us now discuss the order of our proposed scheme. For definiteness, the advection along the $x^{\widetilde{1}}$ direction is considered and for brevity, only the coordinate index along this direction is displayed. In particular, we are interested in deriving the accuracy of the approximation of the quantity:

$$\frac{\partial(VF)}{\partial x} = \sqrt{g}\frac{\partial(VF)}{\partial\chi}. \qquad (3.24)$$

In our implementation, $\sqrt{g}$ is replaced by its cell average

$$\sqrt{g}_s \simeq \frac{\chi_{s+1/2} - \chi_{s-1/2}}{\delta s}, \qquad (3.25)$$

where δs is the equidistant spacing on the x direction (in the case of the equidistant grid, $\delta s = \delta x$, while for the stretched grid, $\delta s = \delta \eta$). The derivative with respect to χ is approximated according to (3.11), such that Eq. (3.24) becomes:

$$\left(\frac{\partial (VF)}{\partial x}\right)_s \simeq \frac{V_{s+1/2}\mathcal{F}_{s+1/2} - V_{s-1/2}\mathcal{F}_{s-1/2}}{\delta s}. \quad (3.26)$$

The right hand side of the above relation can be expanded with respect to $x = x_s$ as follows:

$$\frac{V_{s+1/2}\mathcal{F}_{s+1/2} - V_{s-1/2}\mathcal{F}_{s-1/2}}{\delta s}$$
$$\simeq \frac{\mathcal{F}_{s+1/2} - \mathcal{F}_{s-1/2}}{\delta s}\left[V_s + \frac{(\delta s)^2}{8}\left(\frac{\partial^2 V}{\partial x^2}\right)_s + \cdots\right]$$
$$+ \frac{\mathcal{F}_{s+1/2} + \mathcal{F}_{s-1/2}}{2}\left[\left(\frac{\partial V}{\partial x}\right)_s + \frac{(\delta s)^2}{24}\left(\frac{\partial^3 V}{\partial x^3}\right)_s + \cdots\right], \quad (3.27)$$

When V is a constant, the error term is that of the scheme used to compute the fluxes, which ensures that $\frac{1}{\delta s}(\mathcal{F}_{s+1/2} - \mathcal{F}_{s-1/2}) = (\partial_x F)_s + O[(\delta s)^n]$, where n is the order of accuracy of the scheme for Cartesian coordinates. In the case when V depends on the coordinate, there are second order errors which are unavoidable in this construction. In the case when the WENO-5 procedure is employed to compute the fluxes $\mathcal{F}_{s+1/2}$, Eq. (3.27) reduces to:

$$\frac{V_{s+1/2}\mathcal{F}_{s+1/2} - V_{s-1/2}\mathcal{F}_{s-1/2}}{\delta s} \simeq \left(\frac{\partial(VF)}{\partial x}\right)_s$$
$$+ \frac{(\delta s)^2}{24}\left\{\frac{\partial}{\partial x}\left[2\frac{\partial V}{\partial x}\frac{\partial f}{\partial x} + f\frac{\partial^2 V}{\partial x^2}\right]\right\}_s + O[(\delta s)^4]. \quad (3.28)$$

Even though the resulting implementation presents errors which are second order with respect to δs, we find the implementation of the numerical fluxes using the WENO-5 algorithm to be more accurate than when using second order schemes, such as the flux limiters scheme [69, 87, 107].

F. Diffuse reflection boundary conditions

In the case of diffuse reflection, the flux of particles returning into the fluid domain through the cell interfaces between the fluid and the walls follow Maxwellian distributions. In the flows considered in this paper, the walls are always perpendicular to the direction corresponding to the first coordinate $x^{\widetilde{1}}$. For definiteness, let us consider the case of the left boundary, for which the above condition reads:

$$\mathcal{F}_{\widetilde{1};1/2,p} = f^{(\text{eq})}(n_{\text{left}}, \boldsymbol{u}_{\text{left}}, T_{\text{left}})(V^{\widetilde{1}}_{1/2,p} > 0). \quad (3.29)$$

We note that Eq. (3.29) holds in both the $\widetilde{f}$ and in the χ formulations, since the $\sqrt{g}$ factor which multiplies the

distribution function in the $\widetilde{f}$ approach ($\widetilde{f} = f\sqrt{g}$) can easily be absorbed into the unknown wall particle number density n_{left}.

The flux in Eq. (3.29) can be easily achieved analytically by populating the ghost nodes at $s = -2, -1$ and 0 according to ($V^{\widetilde{1}}_{1/2,p} > 0$):

$$F_{-2,p} = F_{-1,p} = F_{0,p} = f^{(\text{eq})}(n_{\text{left}}, \boldsymbol{u}_{\text{left}}, T_{\text{left}}). \quad (3.30)$$

With the above definitions, Eq. (3.16) shows that $\sigma_1 = 0$ for $s = 0$. According to Table II, $\overline{\omega}_1 = 1$ and $\overline{\omega}_2 = \overline{\omega}_3 = 0$ when $\sigma_1 = 0$. Thus, Eq. (3.12) implies that ($V^{\widetilde{1}}_{1/2,p} > 0$):

$$\mathcal{F}_{\widetilde{1};1/2,p} = \mathcal{F}^1_{\widetilde{1};1/2,p} = F_{0,p}. \quad (3.31)$$

Thus, Eq. (3.29) is established.

In order to calculate the fluxes at $s = 1/2$ and $s = 3/2$ for particles traveling towards the wall ($V^{\widetilde{1}}_{1/2,p} < 0$), the populations in the ghost nodes at $s = 0$ and $s = -1$ are obtained using a quadratic extrapolation:

$$F_{0,p} = 3F_{1,p} - 3F_{2,p} + F_{3,p},$$
$$F_{-1,p} = 6F_{1,p} - 8F_{2,p} + 3F_{3,p}. \quad (3.32)$$

Finally, mass conservation is ensured by requiring that:

$$\int d^3\hat{p}\mathcal{F}_{\widetilde{1};1/2,p}V^{\widetilde{1}}_{1/2,p} = 0. \quad (3.33)$$

This translates into the following equation for n_w:

$$n_w = -\frac{\int_{V^{\widetilde{1}}_{1/2,p}<0} d^3\hat{p}\mathcal{F}_{\widetilde{1};1/2,p}V^{\widetilde{1}}_{1/2,p}}{\int_{V^{\widetilde{1}}_{1/2,p}>0} d^3\hat{p}f^{(\text{eq})}(n=1, \boldsymbol{u}_{\text{left}}, T_{\text{left}})V^{\widetilde{1}}_{1/2,p}}. \quad (3.34)$$

IV. MIXED QUADRATURE LB MODELS

In this Section, the construction of mixed quadrature LB models for flows in curvilinear geometries will be discussed. Since the flows considered in this paper are homogeneous with respect to the z axis, the momentum degree of freedom along this axis can be integrated out, giving rise to the reduced Boltzmann equations which will be discussed in Subsec. IV A. The choice of quadrature for the two remaining directions is discussed in Subsec. IV B. The implementation of the inertial forces arising due to the formulation of the Boltzmann equation with respect to triads is discussed in Subsec. IV C.

A. Reduced Boltzmann equation

The flows considered in this paper are homogeneous with respect to the z axis. Hence, it is convenient to

define the following reduced distribution functions:

$$f' = \int_{-\infty}^{\infty} dp^{\hat{z}} f,$$

$$f'' = \int_{-\infty}^{\infty} dp^{\hat{z}} \frac{(p^{\hat{z}})^2}{m} f. \tag{4.1}$$

With the aid of these two reduced distributions, the macroscopic fields (2.29) can be written as:

$$n = \int d^2\hat{p}\, f', \tag{4.2a}$$

$$u^{\hat{a}} = \frac{1}{\rho} \int d^2\hat{p}\, p^{\hat{a}}\, f', \tag{4.2b}$$

$$T^{\hat{a}\hat{b}} = \int d^2\hat{p}\, \frac{\xi^{\hat{a}}\xi^{\hat{b}}}{m} f', \tag{4.2c}$$

$$q^{\hat{a}} = \int d^2\hat{p} \left(\frac{\boldsymbol{\xi}^2}{2m} f' + \frac{1}{2}f'' \right) \frac{\xi^{\hat{a}}}{m}, \tag{4.2d}$$

where the indices $\hat{a}, \hat{b} \in \{\hat{1}, \hat{2}\}$. Moreover, the temperature is defined as:

$$\frac{3}{2}nT = \int d^2\hat{p} \left(\frac{\boldsymbol{\xi}^2}{2m} f' + \frac{1}{2}f'' \right). \tag{4.3}$$

Thus, the function f'' appears only in the definitions of the temperature T and heat flux $q^{\hat{a}}$.

B. Choice of quadrature

We perform the numerical simulations presented in this paper using the mixed quadrature lattice Boltzmann models introduced in Refs. [34–36]. Depending on the flow regime under consideration, a mixture of the full-range Gauss-Hermite and half-range Gauss-Hermite quadratures can be employed.

For definiteness, let us consider the case when the half-range Gauss-Hermite quadrature of order Q_1 is employed along the first coordinate direction, while the full-range Gauss-Hermite quadrature of order Q_2 is employed along the second coordinate direction. Following the notation introduced in Refs. [34, 36], this model can be denoted using:

$$\mathrm{HH}(\mathcal{N}_1; Q_1) \times \mathrm{H}(\mathcal{N}_2; Q_2) \tag{4.4}$$

where $\mathcal{N}_a$ represents the order of the expansion of the equilibrium distribution $f^{(\mathrm{eq})}$ with respect to axis a, as will be discussed in Sec. IV D.

The choice of quadrature controls the discretization of the momentum space, as well as the momentum space integration. In particular, the moments (2.19) are evaluated as:

$$M^{\hat{a}_1 \dots \hat{a}_s} = \sum_{i=1}^{\mathcal{Q}_1} \sum_{j=1}^{\mathcal{Q}_2} f'_{ij} \prod_{\ell=1}^{s} p_{ij}^{\hat{a}_\ell}. \tag{4.5}$$

A similar prescription holds for the macroscopic quantities appearing in Eq. (4.2). The total number of quadrature points on axis a is $\mathcal{Q}_a = Q_a$ for the full-range Gauss-Hermite quadrature and $\mathcal{Q}_a = 2Q_a$ for the half-range Gauss-Hermite quadrature. In particular, $\mathcal{Q}_1 = 2Q_1$ and $\mathcal{Q}_2 = Q_2$ for the example considered in Eq. (4.4).

The components of $\boldsymbol{p}_{ij} = \{p_i^{\hat{1}}, p_j^{\hat{2}}\}$ are indexed on each direction separately, where $1 \le i \le \mathcal{Q}_1$ and $1 \le j \le \mathcal{Q}_2$. For the half-range Gauss-Hermite quadrature, we use the convention that the points with $1 \le i \le Q_1$ lie on the positive semi-axis of the radial direction, being given as the roots of the half-range Hermite polynomial $\mathfrak{h}_{Q_1}(x)$ of order Q_1:

$$\mathfrak{h}_{Q_1}(p_i^{\hat{1}}) = 0, \qquad (1 \le i \le Q_1), \tag{4.6}$$

while $p_{Q_1+i}^{\hat{1}} = -p_i^{\hat{1}}$ $(1 \le i \le Q_1)$. On the direction where the full-range Gauss-Hermite quadrature is applied, the quadrature points are chosen as the roots of the Hermite polynomial $H_{Q_2}(x)$ of order Q_2:

$$H_{Q_2}(p_j^{\hat{2}}) = 0. \tag{4.7}$$

The link between the discrete distributions f'_{ij} and f''_{ij} and the reduced Boltzmann distribution functions $f'(p^{\hat{1}}, p^{\hat{2}})$ and $f''(p^{\hat{1}}, p^{\hat{2}})$ is given through:

$$\begin{pmatrix} f'_{ij} \\ f''_{ij} \end{pmatrix} = \frac{w_i^{\mathfrak{h}}(Q_1) w_j^H(Q_2)}{\omega(p_i^{\hat{1}})\omega(p_j^{\hat{2}})} \begin{pmatrix} f'(p_i^{\hat{1}}, p_j^{\hat{2}}) \\ f''(p_i^{\hat{1}}, p_j^{\hat{2}}) \end{pmatrix}, \tag{4.8}$$

where the weight function $\omega(x)$ for the half-range and full-range Hermite polynomials is:

$$\omega(x) = \frac{1}{\sqrt{2\pi}} e^{-x^2/2}. \tag{4.9}$$

The quadrature weights $w_j^H(Q_2)$ for the full-range Gauss-Hermite quadrature of order Q_2 are [35]:

$$w_j^H(Q_2) = \frac{Q_2!}{H_{Q_2+1}^2(p_j^{\hat{2}})}. \tag{4.10}$$

The quadrature weights $w_i^{\mathfrak{h}}(Q_1)$ for the half-range Gauss-Hermite quadrature of order Q_1 are [34, 35]:

$$w_i^{\mathfrak{h}}(Q_1) = \frac{p_i^{\hat{1}} a_{Q_1-1}^2}{\mathfrak{h}_{Q_1-1}^2(p_i^{\hat{1}})[p_i^{\hat{1}} + \mathfrak{h}_{Q_1}^2(0)/\sqrt{2\pi}]}, \tag{4.11}$$

where

$$a_\ell = \frac{\mathfrak{h}_{\ell+1,\ell+1}}{\mathfrak{h}_{\ell,\ell}} \tag{4.12}$$

is written in terms of the coefficients $\mathfrak{h}_{\ell,s}$ of x^s in the polynomial expansion of $\mathfrak{h}_\ell(x)$:

$$\mathfrak{h}_\ell(x) = \sum_{s=0}^{\ell} \mathfrak{h}_{\ell,s} x^s. \tag{4.13}$$

C. Force terms

Since the functional dependence of the distribution function on the components of the momentum is removed through the discretization of the momentum space, an appropriate method for the computation of the momentum derivative of the distribution function must be employed. Discrete velocity models (DVMs) usually rely on finite differences to perform the momentum space derivatives [39, 88]. In this paper, we take the lattice Boltzmann approach introduced in Ref. [116], according to which the momentum space derivative is projected on the space of orthogonal Hermite polynomials. More precisely, we follow Ref. [36] and write the terms involving the momentum derivatives of f' and f'' as follows:

$$\left[\frac{\partial}{\partial p^{\hat{1}}}\begin{pmatrix} f' \\ f'' \end{pmatrix}\right]_{ij} = \sum_{i'=1}^{\mathcal{Q}_a} \mathcal{K}^{\hat{1}}_{i,i'} \begin{pmatrix} f'_{i',j} \\ f''_{i',j} \end{pmatrix},$$

$$\left[\frac{\partial}{\partial p^{\hat{1}}}\begin{pmatrix} p^{\hat{1}} f' \\ p^{\hat{1}} f'' \end{pmatrix}\right]_{ij} = \sum_{i'=1}^{\mathcal{Q}_a} \widetilde{\mathcal{K}}^{\hat{1}}_{i,i'} \begin{pmatrix} f'_{i',j} \\ f''_{i',j} \end{pmatrix}, \qquad (4.14)$$

and similarly for the derivatives with respect to $p^{\hat{2}}$.

In the case of the full-range Gauss-Hermite quadrature, the matrix $\mathcal{K}^{\hat{a}}_{k,k'}$ has the following form [36]:

$$\mathcal{K}^{\hat{a},H}_{k,k'} = -w^H_k \sum_{\ell=0}^{Q_a-1} \frac{1}{\ell!} H_{\ell+1}(p^{\hat{a}}_k) H_\ell(p^{\hat{a}}_{k'}), \qquad (4.15)$$

while in the case of the half-range Gauss-Hermite quadrature, it is given by [36]:

$$\mathcal{K}^{\hat{a},\mathfrak{h}}_{k,k'} = w^{\mathfrak{h}}_k \sigma^{\hat{a}}_k \left\{ \frac{1+\sigma^{\hat{a}}_k \sigma^{\hat{a}}_{k'}}{2} \sum_{\ell=0}^{Q_a-2} \mathfrak{h}_\ell(|p^{\hat{a}}_{k'}|) \right.$$
$$\times \left[\frac{\mathfrak{h}_{\ell,0}}{\sqrt{2\pi}} \sum_{s=\ell+1}^{Q_a-1} \mathfrak{h}_{s,0} \mathfrak{h}_s(|p^{\hat{a}}_k|) - \frac{\mathfrak{h}_{\ell,\ell}}{\mathfrak{h}_{\ell+1,\ell+1}} \mathfrak{h}_{\ell+1}(|p^{\hat{a}}_k|) \right]$$
$$\left. - \frac{1}{2\sqrt{2\pi}} \Phi^{Q_a}_0(|p^{\hat{a}}_k|) \Phi^{Q_a}_0(|p^{\hat{a}}_{k'}|) \right\}. \quad (4.16)$$

In the above, $\sigma^{\hat{a}}_k$ and $\sigma^{\hat{a}}_{k'}$ are the signs of $p^{\hat{a}}_k$ and $p^{\hat{a}}_{k'}$, respectively, having values $\sigma^{\hat{a}}_k = 1$ for $1 \le k \le Q_a$ and $\sigma^{\hat{a}}_k = -1$ when $Q_a < k \le 2Q_a$. The function $\Phi^n_s(x)$ is defined as follows [36]:

$$\Phi^n_s(x) = \sum_{\ell=s}^{n} \mathfrak{h}_{\ell,s} \mathfrak{h}_\ell(x). \qquad (4.17)$$

The details regarding the expansions of $\partial(p^{\hat{a}} f')/\partial p^{\hat{a}}$ and $\partial(p^{\hat{a}} f'')/\partial p^{\hat{a}}$ with respect to the full-range and half-range Hermite polynomials are presented in Appendix D. Below we only quote the results. In the case when the full-range Gauss-Hermite quadrature is employed, the

matrix $\widetilde{\mathcal{K}}^{\hat{a}}_{k,k'}$ reduces to:

$$\widetilde{\mathcal{K}}^{\hat{a},H}_{k,k'} = -w^H_k \sum_{\ell=0}^{Q_a-2} \frac{1}{\ell!} H_{\ell+1}(p^{\hat{a}}_k)[H_{\ell+1}(p^{\hat{a}}_{k'}) + \ell H_{\ell-1}(p^{\hat{a}}_{k'})]. \qquad (4.18)$$

In the case of the half-range Gauss-Hermite quadrature, the kernel $\widetilde{\mathcal{K}}^{\hat{a},\mathfrak{h}}_{k,k'}$ is given by:

$$\widetilde{\mathcal{K}}^{\hat{a},\mathfrak{h}}_{k,k'} = -w^{\mathfrak{h}}_k \frac{1+\sigma^{\hat{a}}_k \sigma^{\hat{a}}_{k'}}{2} \sum_{\ell=0}^{Q_a-1} \mathfrak{h}_\ell(|p^{\hat{a}}_k|) \left[\ell\, \mathfrak{h}_\ell(|p^{\hat{a}}_{k'}|) \right.$$
$$\left. + \frac{\mathfrak{h}^2_{\ell,0} + \mathfrak{h}^2_{\ell-1,0}}{a_{\ell-1}\sqrt{2\pi}} \mathfrak{h}_{\ell-1}(|p^{\hat{a}}_{k'}|) + \frac{1}{a_{\ell-1}a_{\ell-2}} \mathfrak{h}_{\ell-2}(|p^{\hat{a}}_{k'}|) \right]. \qquad (4.19)$$

D. Equilibrium distribution function

We now present the construction of the equilibrium distribution function (2.16) appearing on the right hand side of Eq. (2.31), as well as in the boundary conditions and in the initial state. After eliminating the $p^{\hat{z}}$ degree of freedom, $f^{(eq)}$ is replaced by

$$f'_{(eq)} = \int_{-\infty}^{\infty} dp^{\hat{z}}\, f^{(eq)},$$
$$f''_{(eq)} = \int_{-\infty}^{\infty} dp^{\hat{z}}\, \frac{(p^{\hat{z}})^2}{m} f^{(eq)} = T f'_{(eq)}. \qquad (4.20)$$

In discrete velocity models (DVMs), it is customary to evaluate the equilibrium distributions $f'_{(eq)}$ and $f''_{(eq)}$ directly, i.e. by computing the value of the Maxwellian for each given discrete momentum vector $\boldsymbol{p}_{ij}$ [39, 88]. On the other hand, the lattice Boltzmann (LB) approach is to replace the Maxwell-Boltzmann distribution with a polynomial approximation which ensures the exact recovery of its first few moments with a relatively small quadrature order. Thus, in this paper, we take the LB approach and replace f'_{eq} and f''_{eq} with their polynomial approximations.

As discussed in Refs. [34, 35], $f'_{(eq)}$ can be factorized with respect to $p^{\hat{1}}$ and $p^{\hat{2}}$ as follows:

$$f'_{(eq)} = n\, g_1(p^{\hat{1}}) g_2(p^{\hat{2}}),$$
$$g_a(p^{\hat{a}}) = \frac{1}{\sqrt{2\pi mT}} \exp\left[-\frac{(p^{\hat{a}} - mu^{\hat{a}})^2}{2mT}\right]. \qquad (4.21)$$

Following the discretization of the momentum space, $f'_{(eq)}$ is replaced by $f'_{(eq);ij} = n\, g_{1,i} g_{2,j}$, while $f''_{(eq);ij} = T f'_{(eq);ij}$. For the case of the full-range Gauss-Hermite quadrature, the polynomial approximation of $g_{a,k}$ is [34, 35]:

$$g^H_{a,k} = w^H_k \sum_{\ell=0}^{\mathcal{N}_a} H_\ell(p^{\hat{a}}_k) \sum_{s=0}^{\lfloor \ell/2 \rfloor} \frac{(mT-1)^s (mu^{\hat{a}})^{\ell-2s}}{2^s s!(\ell-2s)!}, \quad (4.22)$$
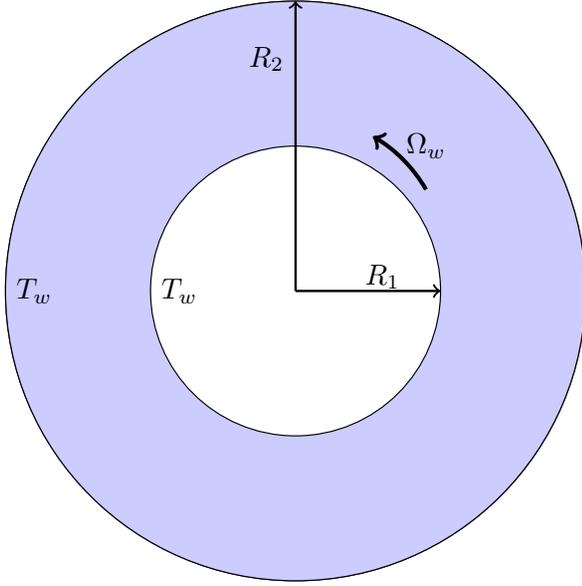
FIG. 3. Circular Couette flow setup.

where the expansion order $\mathcal{N}_a$ is a free parameter satisfying

$$0 \leq \mathcal{N}_a < Q_a. \tag{4.23}$$

An expansion of $g_{a,k}$ up to order $\mathcal{N}_a$ ensures the *exact* recovery of the moments (2.17) for polynomials in $p^{\hat{a}}$ of order less than or equal to $\mathcal{N}_a$. In the case of the half-range Gauss-Hermite quadrature, the polynomial approximation of $g_{a,k}$ can be put in the following form [34, 35]:

$$g_{a,k}^{\flat} = \frac{w_k^{\flat}}{2} \sum_{s=0}^{\mathcal{N}_a} \left(\frac{mT}{2} \right)^{s/2} \Phi_s^{\mathcal{N}_a}(|p_k^{\hat{a}}|)$$

$$\times \left[(1 + \mathrm{erf}\zeta^{\hat{a}}) P_s^+(\zeta^{\hat{a}}) + \frac{2}{\sqrt{\pi}} e^{-\zeta_{\hat{a}}^2} P_s^*(\zeta^{\hat{a}}) \right], \tag{4.24}$$

where $\zeta^{\hat{a}} = u^{\hat{a}}\sqrt{m/2T}$ when $p_k^{\hat{a}} > 0$ and $\zeta^{\hat{a}} = -u^{\hat{a}}\sqrt{m/2T}$ when $p_k^{\hat{a}} < 0$. The polynomials $P_s^+(x)$ and $P_s^*(x)$ are defined as:

$$P_s^{\pm}(x) = e^{\mp x^2} \frac{d^s}{dx^s} e^{\pm x^2},$$

$$P_s^*(x) = \sum_{j=0}^{s-1} \binom{s}{j} P_j^+(x) P_{s-j-1}^-(x). \tag{4.25}$$

V. CIRCULAR COUETTE FLOW

In this Section, the vielbein approach introduced in Sec. II is validated in the case of the circular Couette flow. The flow domain is bounded by two coaxial cylinders of radii $R_{\mathrm{in}} < R_{\mathrm{out}}$ which are kept at equal temperatures T_w, as shown in Fig. 3. The cylinders are free to rotate

around their vertical axis (the z axis). We are interested only in the stationary state and consider that the flow is homogeneous with respect to the z and φ directions. In order to take advantage of the φ homogeneity, we employ the vielbein approach.

This Section is structured as follows. In Subsec. V A, the Boltzmann equation is written with respect to the cylindrical coordinate system, in both the $\widetilde{f}$ and χ formulations, with or without grid stretching, while the ensuing macroscopic equations are discussed in Subsec. V B. These formulations are discussed in Subsec. V C, where we demonstrate the failure of the $\widetilde{f}$ formulations to capture the constant solution when the two cylinders are at rest, as well as the solution corresponding to rigid rotation. The $\widetilde{f}$ approach is not considered further outside this Subsection. Subsections V D and V E validate the χ implementation against analytic solutions in the hydrodynamic and ballistic regimes. In the transition regime, our scheme is validated against the DVM results presented in Ref. [88] in Subsec. V F. A performance analysis of our vielbein-based implementation is presented in Subsec. V G. Finally, conclusions are presented in Subsec. V H. The details regarding the mixed quadrature LB models employed for the simulations discussed in Subsecs. V D, V E and V F are summarized in Table III.

The initial state for all the numerical simulations presented in this Section consists of a gas in thermal equilibrium having constant density $n_0 = 1$, vanishing velocity $u^{\hat{R}} = u^{\hat{\varphi}} = u^{\hat{z}} = 0$ and $T_0 = T_w = 1$.

A. Boltzmann equation

Let us specialize the formalism of Section II to the case of the Couette flow between coaxial cylinders, described in Fig. 3. To describe the geometry of this flow, it is convenient to employ cylindrical coordinates $\{x^{\tilde{\imath}}\} = \{R, \varphi, z\}$ through $x = R\cos\varphi$ and $y = R\sin\varphi$. The line element (2.2) with respect to cylindrical coordinates is:

$$ds^2 = dR^2 + R^2 d\varphi^2 + dz^2, \tag{5.1}$$

while the triad vectors and the one-forms can be chosen as:

$$e_{\hat{R}} = \partial_R, \qquad e_{\hat{\varphi}} = R^{-1}\partial_\varphi, \qquad e_{\hat{z}} = \partial_z,$$
$$\omega^{\hat{R}} = dR, \qquad \omega^{\hat{\varphi}} = R\,d\varphi, \qquad \omega^{\hat{z}} = dz. \tag{5.2}$$

The square root of the determinant of the metric in Eq. (5.1) is equal to

$$\sqrt{g} = \sqrt{g_R} = R, \tag{5.3}$$

while $\sqrt{g_\varphi} = 1$ since the metric components do not depend on the azimuthal coordinate φ.

The non-vanishing connection coefficients for the triad (5.2) are:

$$\Gamma^{\hat{R}}{}_{\hat{\varphi}\hat{\varphi}} = -\frac{1}{R}, \qquad \Gamma^{\hat{\varphi}}{}_{\hat{R}\hat{\varphi}} = \frac{1}{R}, \tag{5.4}$$

such that the Boltzmann equation in the $\widetilde{f}$ formulation (3.1) reads:

$$\frac{\partial}{\partial t}\begin{pmatrix}\widetilde{f}'\\\widetilde{f}''\end{pmatrix} + \frac{p^{\hat{R}}}{m}\frac{\partial}{\partial R}\begin{pmatrix}\widetilde{f}'\\\widetilde{f}''\end{pmatrix} + \frac{1}{mR}\left[(p^{\hat{\varphi}})^2\frac{\partial}{\partial p^{\hat{R}}}\begin{pmatrix}\widetilde{f}'\\\widetilde{f}''\end{pmatrix}\right.$$
$$\left. -p^{\hat{R}}\frac{\partial}{\partial p^{\hat{\varphi}}}\begin{pmatrix}p^{\hat{\varphi}}\widetilde{f}'\\p^{\hat{\varphi}}\widetilde{f}''\end{pmatrix}\right] = -\frac{1}{\tau}\begin{pmatrix}\widetilde{f}'-\widetilde{f}'_{(\mathrm{eq})}\\\widetilde{f}''-\widehat{f}''_{(\mathrm{eq})}\end{pmatrix}, \quad (5.5)$$

where the flow was assumed to be homogeneous with respect to the φ and z coordinates and the $p^{\hat{z}}$ degree of freedom was reduced as described in Sec. IV A , while $\widetilde{f}' = f'R$ and $\widetilde{f}'' = f''R$. The reduced distributions f' and f'' were defined in Eq. (4.1). The above equation can be shown to be equivalent to the equations used in Refs. [117, 118].

As pointed out in Ref. [107], the numerical implementation of hyperbolic equations in the $\widetilde{f}$ formulation (i.e., by computing the numerical fluxes at the level of $\widetilde{f} = f\sqrt{g}$) is problematic since the preservation of a constant (analytic) solution is not guaranteed numerically.

In the χ formulation, the variable χ^R can be introduced via Eq. (3.4), following Ref. [113]:

$$\chi^R = \frac{R^2}{2}. \quad (5.6)$$

The Boltzmann equation in the χ formulation (2.24) can thus be written as follows:

$$\frac{\partial}{\partial t}\begin{pmatrix}f'\\f''\end{pmatrix} + \frac{p^{\hat{R}}}{m}\frac{\partial}{\partial \chi^R}\begin{pmatrix}f'R\\f''R\end{pmatrix} + \frac{1}{mR}\left[(p^{\hat{\varphi}})^2\frac{\partial}{\partial p^{\hat{R}}}\begin{pmatrix}f'\\f''\end{pmatrix}\right.$$
$$\left. -p^{\hat{R}}\frac{\partial}{\partial p^{\hat{\varphi}}}\begin{pmatrix}p^{\hat{\varphi}}f'\\p^{\hat{\varphi}}f''\end{pmatrix}\right] = -\frac{1}{\tau}\begin{pmatrix}f'-f'_{(\mathrm{eq})}\\f''-f''_{(\mathrm{eq})}\end{pmatrix}. \quad (5.7)$$

More details regarding our numerical implementation of the above equation and its order of accuracy are provided in Subsecs. III D and III E, respectively.

Let us now consider the grid stretching procedure described in Sec. III B for the case of the radial coordinate. Defining η in terms of R via Eq. (3.8) changes the line element (5.1) to

$$ds^2 = \left[\frac{A_0(R_{\mathrm{out}} - R_{\mathrm{in}})}{A\cosh^2\eta}\right]^2 d\eta^2 + R^2(\eta)d\varphi^2 + dz^2. \quad (5.8)$$

The triad corresponding to the above metric is:

$$e_{\hat{\eta}} = \frac{A\cosh^2\eta}{A_0(R_{\mathrm{out}} - R_{\mathrm{in}})}\partial_\eta, \qquad e_{\hat{\varphi}} = \frac{1}{R(\eta)}\partial_\varphi, \qquad e_{\hat{z}} = \partial_z,$$
$$(5.9)$$

while the non-vanishing connection coefficients are:

$$\Gamma^{\hat{\varphi}}{}_{\hat{\eta}\hat{\varphi}} = -\Gamma^{\hat{\eta}}{}_{\hat{\varphi}\hat{\varphi}} = \frac{1}{R(\eta)}. \quad (5.10)$$

The Boltzmann equation in the $\widetilde{f}$ formulation (5.5) becomes:

$$\frac{\partial}{\partial t}\begin{pmatrix}\widetilde{f}'\\\widetilde{f}''\end{pmatrix} + \frac{p^{\hat{\eta}}}{m}\frac{\partial}{\partial\eta}\left[\frac{A\cosh^2\eta}{A_0(R_{\mathrm{out}} - R_{\mathrm{in}})}\begin{pmatrix}\widetilde{f}'\\\widetilde{f}''\end{pmatrix}\right]$$
$$+\frac{1}{mR(\eta)}\left[(p^{\hat{\varphi}})^2\frac{\partial}{\partial p^{\hat{\eta}}}\begin{pmatrix}\widetilde{f}'\\\widetilde{f}''\end{pmatrix} - p^{\hat{\eta}}\frac{\partial}{\partial p^{\hat{\varphi}}}\begin{pmatrix}p^{\hat{\varphi}}\widetilde{f}'\\p^{\hat{\varphi}}\widetilde{f}''\end{pmatrix}\right]$$
$$= -\frac{1}{\tau}\begin{pmatrix}\widetilde{f}'-\widetilde{f}'_{(\mathrm{eq})}\\\widetilde{f}''-\widehat{f}''_{(\mathrm{eq})}\end{pmatrix}, \quad (5.11)$$

while

$$\sqrt{g} = \sqrt{g_\eta} = \frac{A_0(R_{\mathrm{out}} - R_{\mathrm{in}})R(\eta)}{A\cosh^2\eta}. \quad (5.12)$$

In the χ formulation, the equivalent of Eq. (5.11) is identical to Eq. (5.7), where $p^{\hat{R}}$ is replaced by $p^{\hat{\eta}}$, R is replaced by $R(\eta)$ and χ^R is replaced by $\chi^\eta = R^2(\eta)/2$:

$$\frac{\partial}{\partial t}\begin{pmatrix}f'\\f''\end{pmatrix} + \frac{p^{\hat{\eta}}}{m}\frac{\partial}{\partial\chi^\eta}\begin{pmatrix}f'R(\eta)\\f''R(\eta)\end{pmatrix}$$
$$+\frac{1}{mR(\eta)}\left[(p^{\hat{\varphi}})^2\frac{\partial}{\partial p^{\hat{\eta}}}\begin{pmatrix}f'\\f''\end{pmatrix} - p^{\hat{\eta}}\frac{\partial}{\partial p^{\hat{\varphi}}}\begin{pmatrix}p^{\hat{\varphi}}f'\\p^{\hat{\varphi}}f''\end{pmatrix}\right]$$
$$= -\frac{1}{\tau}\begin{pmatrix}f'-f'_{(\mathrm{eq})}\\f''-f''_{(\mathrm{eq})}\end{pmatrix}. \quad (5.13)$$

B. Macroscopic equations

In this Subsection, the macroscopic equations (2.28) are presented for the case when the stationary regime is achieved. The continuity equation (2.28a) reduces to:

$$\nabla_{\hat{a}}(nu^{\hat{a}}) = \frac{1}{R}\partial_R(nRu^{\hat{R}}) = 0. \quad (5.14)$$

Imposing a vanishing mass flux at the boundaries ($R = R_{\mathrm{in}}$ and $R = R_{\mathrm{out}}$) implies $u^{\hat{R}} = 0$ throughout the channel. This also implies that $\nabla_{\hat{a}}u^{\hat{a}} = 0$ and $u^{\hat{a}}\nabla_{\hat{a}}\phi = 0$, for any scalar function ϕ which does not depend on t, φ or z.

Substituting $\hat{a} \in \{\hat{R}, \hat{\varphi}, \hat{z}\}$ into the Cauchy equation (2.28b) gives:

$$\rho(u^{\hat{\varphi}})^2 = \partial_R(RT^{\hat{R}\hat{R}}) - T^{\hat{\varphi}\hat{\varphi}}, \quad (5.15a)$$
$$\partial_R(R^2 T^{\hat{R}\hat{\varphi}}) = 0, \quad (5.15b)$$
$$\partial_R(RT^{\hat{R}\hat{z}}) = 0. \quad (5.15c)$$

Considering that the flow is homogeneous along the z direction, $T^{\hat{R}\hat{z}} = 0$ is an acceptable solution of Eq. (5.15c). Next, the nondiagonal component $T^{\hat{R}\hat{\varphi}}$ of the stress-tensor can be expressed analytically as:

$$T^{\hat{R}\hat{\varphi}} = T^{\hat{R}\hat{\varphi}}_{\mathrm{in}}\frac{R_{\mathrm{in}}^2}{R^2}, \quad (5.16)$$

where $T_{\text{in}}^{\hat{R}\hat{\varphi}}$ is the value of $T^{\hat{R}\hat{\varphi}}$ in the vicinity of the inner cylinder. It is remarkable that Eq. (5.16) is valid for all degrees of rarefaction, while $T_{\text{in}}^{\hat{R}\hat{\varphi}}$ depends on the flow parameters, such as Kn or Ω_{in}.

Finally, the energy equation (2.28c) reduces to:

$$\partial_R(Rq^{\hat{R}}) + R^2 T^{\hat{R}\hat{\varphi}}\partial_R(R^{-1}u^{\hat{\varphi}}) = 0. \qquad (5.17)$$

Using Eq. (5.16) for $T^{\hat{R}\hat{\varphi}}$ yields:

$$q^{\hat{R}} + u^{\hat{\varphi}}T^{\hat{R}\hat{\varphi}} = \frac{Q}{R}, \qquad (5.18)$$

where Q is a constant which depends on the flow parameters.

In Subsections V D and V E, analytic solutions for n, $u^{\hat{\varphi}}$, T and $q^{\hat{R}}$ will be derived in the Navier-Stokes and ballistic regimes, respectively.

C. Comparison of $\widetilde{f}$ and χ formulations

This Subsection is dedicated to the comparative analysis of the $\widetilde{f}$ and χ implementations of the Boltzmann equation. These implementations are considered with and without the grid stretching procedure described in Sec. III B. The implementation of the advection part, described in the general case in Sec. III C, is given in Subsec. V C 1 for the particular cases considered herein. Two test cases are further considered. The first, consisting of the trivial setup when both cylinders are at rest and $f' = f'' = \text{const}$, is presented in Subsec. V C 2. The second test case, corresponding to rigid rotation (i.e. when the two cylinders rotate at the same angular speed), is considered in Subsec. V C 3. Our conclusions are presented in Subsec. V C 4.

1. Numerical scheme

As described in Sec. III, the flow domain is discretized using N_R cells along the R direction, while $N_\varphi = 1$ cells are used along the homogeneous φ direction. For the case of an equidistant grid, the radial coordinates of the centers of the N_R cells are given as:

$$R_s = R_{\text{in}} + \frac{s - 0.5}{N}(R_{\text{out}} - R_{\text{in}}), \qquad (5.19)$$

where $1 \le s \le N_R$, while R_{in} and R_{out} are the radii of the inner and outer cylinders, respectively. When employing the grid stretching procedure described in Sec. III B, the stretching parameter η is discretized equidistantly:

$$\eta_s = \eta_{\text{in}} + \frac{s - 0.5}{N}(\eta_{\text{out}} - \eta_{\text{in}}), \qquad (5.20)$$

where η_{in} and η_{out} are defined in Eq. (3.10) in terms of R_{in} and R_{out}, respectively.

In the $\widetilde{f}$ formulation (5.5), $\chi^{\widetilde{1}} \equiv \chi^R = R$ and $V^R = p^{\hat{R}}/m$, such that Eq. (3.11) becomes:

$$\left(\frac{\partial(V^R\widetilde{f})}{\partial R}\right)_{s,1} \simeq \frac{p^{\hat{R}}}{m}\frac{\widetilde{\mathcal{F}}_{R;s+1/2,1} - \widetilde{\mathcal{F}}_{R;s-1/2,1}}{\delta R}, \qquad (5.21)$$

where δR is the constant grid spacing along the radial direction. Similarly, $\chi^{\widetilde{1}} \equiv \chi^\eta = \eta$ and $V^\eta = p^{\hat{\eta}}e_{\hat{\eta}}^{\widetilde{\eta}}$ in Eq. (5.11) such that Eq. (3.11) reduces to:

$$\left(\frac{\partial(V^\eta\widetilde{f})}{\partial \eta}\right)_{s,1} \simeq \frac{p^{\hat{\eta}}}{m}$$
$$\times \frac{e_{\hat{\eta};s+1/2}^{\widetilde{\eta}}\widetilde{\mathcal{F}}_{\eta;s+1/2,1} - e_{\hat{\eta};s-1/2}^{\widetilde{\eta}}\widetilde{\mathcal{F}}_{\eta;s-1/2,1}}{\delta\eta}, \qquad (5.22)$$

where $\delta\eta$ is the constant grid spacing with respect to η, while $e_{\hat{\eta}}$ is given in Eq. (5.9).

In the χ formulation (5.7), $\chi^R = R^2/2$ and Eq. (3.11) becomes:

$$\left(\frac{\partial(Rp^{\hat{R}}f/m)}{\partial \chi^R}\right)_{s,1} \simeq \frac{p^{\hat{R}}}{m}$$
$$\times \frac{R_{s+1/2}\mathcal{F}_{\eta;s+1/2,1} - R_{s-1/2}\mathcal{F}_{\eta;s-1/2,1}}{R_s\delta R}. \qquad (5.23)$$

Similarly, in Eq. (5.13), $\chi^\eta = R^2(\eta)/2$, such that Eq. (3.11) reduces to:

$$\left(\frac{\partial[R(\eta)p^{\hat{\eta}}f/m]}{\partial \chi^\eta}\right)_{s,1} \simeq 2\frac{p^{\hat{\eta}}}{m}$$
$$\times \frac{R(\eta_{s+1/2})\mathcal{F}_{\eta;s+1/2,1} - R(\eta_{s-1/2})\mathcal{F}_{\eta;s-1/2,1}}{R^2(\eta_{s+1/2}) - R^2(\eta_{s-1/2})}. \qquad (5.24)$$

2. Cylinders at rest

The case when the inner and outer cylinders are at rest ($\Omega_{\text{in}} = \Omega_{\text{out}} = 0$) and at equal temperature ($T_{\text{in}} = T_{\text{out}} = T_w$) admits the solution

$$f' = f'_{\text{(eq)}}(n_0, \boldsymbol{u} = 0, T_w) = \frac{n_0}{2\pi m T_w}\exp\left(-\frac{p_{\hat{R}}^2 + p_{\hat{\varphi}}^2}{2m T_w}\right), \qquad (5.25)$$

while $f'' = T_w f'$. It can be easily seen that Eq. (5.25) satisfies the Boltzmann equation (5.5), as well as the boundary conditions.

Even though trivial, this simple test case serves as an example which highlights an important drawback of the $\widetilde{f}$ approaches based on Eqs. (5.5) and (5.11). As seen in Fig. 4, the density profile when the $\widetilde{f}$ formulation is employed exhibits fluctuations, while the scheme based on the χ formulations (5.7) and (5.13) recovers Eq. (5.25). Our conclusion is in agreement with that presented in

Regime	Kn	Model	N_{vel}	δt
Low	Hydro	$H(2;3) \times H(2;3)$	9	5×10^{-4}
Mach	0.01	$H(3;4) \times H(2;3)$	12	3×10^{-3}
	0.1	$HH(3;4) \times H(2;3)$	12	3×10^{-3}
	0.5	$HH(4;12) \times H(4;5)$	120	3×10^{-3}
	1	$HH(4;16) \times H(4;5)$	160	2×10^{-3}
	100	$HH(4;40) \times HH(2;3)$	480	10^{-3}
Non-	Hydro	$H(4;5) \times H(4;5)$	25	5×10^{-4}
negligible	0.02	$HH(3;4) \times H(4;5)$	40	10^{-3}
Mach	0.1	$HH(3;4) \times H(4;5)$	40	10^{-3}
	1	$HH(4;24) \times H(4;11)$	528	10^{-3}
	10	$HH(4;60) \times HH(3;4)$	480	5×10^{-4}
	∞	$HH(4;200) \times HH(4;10)$	8000	2×10^{-5}

TABLE III. Mixed quadrature LB models, corresponding total number of velocities N_{vel} and time step δt employed for the simulations of the circular Couette flow presented in Figs. 7 and 17 (low Mach number), as well as in Figs. 8, 13, 14, and 15 (Non-negligible Mach number). In the hydrodynamic regime (Figs. 7 and 8), the relaxation time τ is given by Eq. (5.28) with Kn = 0.001. Outside the hydrodynamic regime (Figs. 15 and 17), τ is related to Kn through Eq. (5.65).
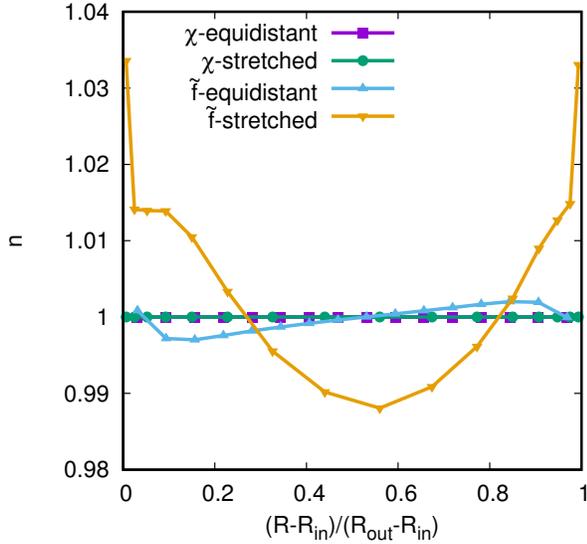
FIG. 4. Density profile $n(R)$ for static cylinders having radii $R_{\text{in}} = 1$ and $R_{\text{out}} = 2$. The numerical results were obtained using the $H(4;5) \times H(4;5)$ model with $\tau = $ Kn/n, where Kn $= 10^{-3}$. In all cases, $N_R = 16$ nodes were used and the stretching was performed according to $\delta = 0.5$ and $A = 0.95$.

Ref. [107]: the numerical fluxes associated to $f' \sqrt{g}$ and $f'' \sqrt{g}$ do not vanish, even when f' and f'' are constant. This leads to a spurious redistribution of f' and f'' due to which the stationary state does not coincide with the analytic solution.
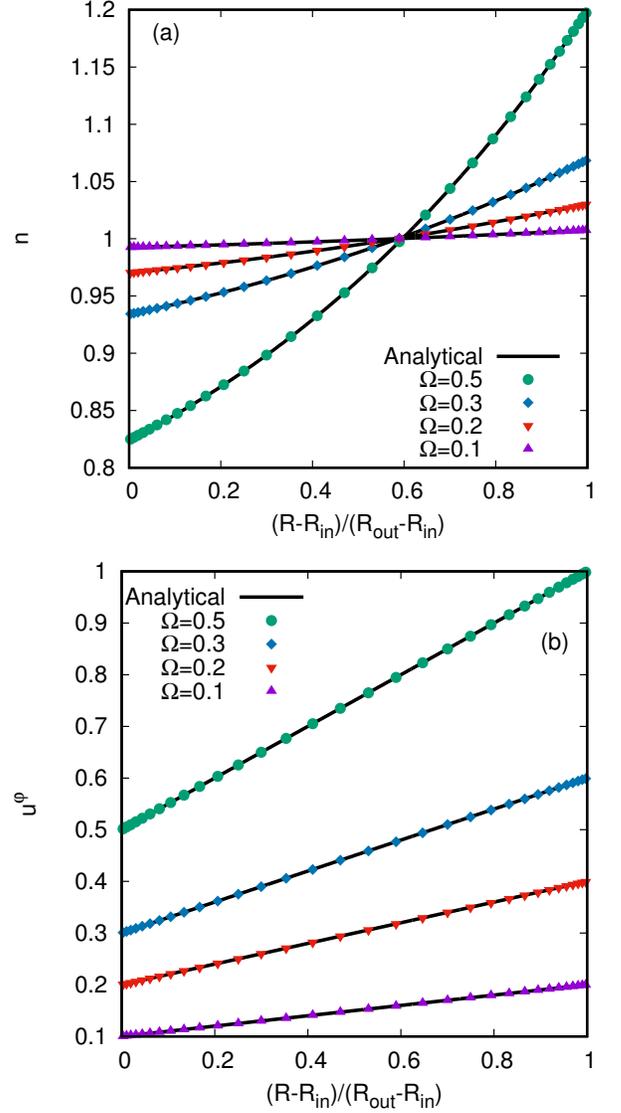
FIG. 5. Numerical results obtained using the $H(4;5) \times H(4;5)$ models for various values of the angular velocity Ω in the case of the rigid rotation considered in Sec. V C 3. (a) Density profile compared to Eq. (5.27). (b) Azimuthal velocity compared to the analytic solution $u^{\hat{\varphi}} = \Omega R$.

3. Rigid rotation

We now turn our attention to another trivial case in which the two cylinders rotate at the same angular speed $\Omega_{\text{in}} = \Omega_{\text{out}} = \Omega_w$. Assuming that the walls have equal temperature $T_{\text{in}} = T_{\text{out}} = T_w$, the analytic solution of the Boltzmann equation (5.5) reads:

$$f'(R) = f^{(\text{eq})}[n(R), u^{\hat{\varphi}} = \Omega R, T_w]$$
$$= \frac{n(R)}{2\pi m T_w} \exp\left[-\frac{p_{\hat{R}}^2 + (p_{\hat{\varphi}} - m\Omega R)^2}{2m T_w}\right], \quad (5.26)$$
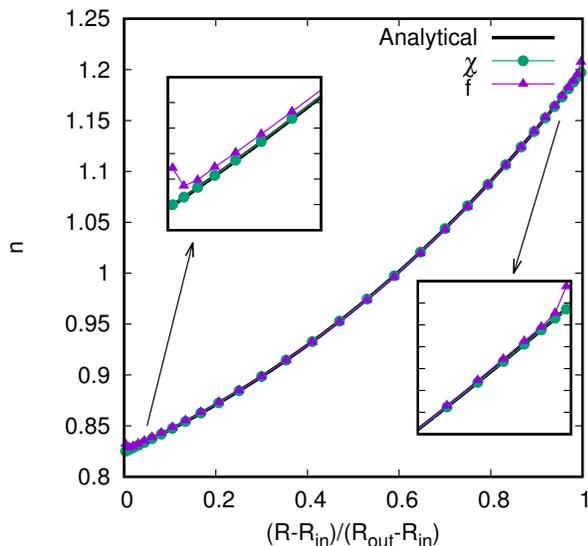
FIG. 6. Comparison of the $\widetilde{f}$ and χ formulations for $\Omega = 0.5$, using the $H(4;5) \times H(4;5)$ model.

and $f''(R) = T_w f'(R)$, while $n(R)$ is given by [119]:

$$n(R) = N_{\text{tot}} \frac{m\Omega^2}{4\pi T_w} \frac{\exp\left[\frac{m\Omega^2}{4T_w}(2R^2 - R_{\text{in}}^2 - R_{\text{out}}^2)\right]}{\sinh\left[\frac{m\Omega^2}{4T_w}(R_{\text{out}}^2 - R_{\text{in}}^2)\right]},$$
(5.27)

where N_{tot} represents the total number of particles per unit height between the two cylinders. The density normalization is chosen such that $N_{\text{tot}} = \pi(R_{\text{out}}^2 - R_{\text{in}}^2)$.

It is worth emphasizing that Eq. (5.26) satisfies the Boltzmann equation for all values of the relaxation time. Fig. 5 shows that our models can successfully reproduce both the velocity (top) and the density profile (bottom) for all tested values of the angular velocity. The models used are $H(4;5) \times H(4;5)$, the Knudsen number is $Kn = 0.001$, the time step is set to $\delta t = 5 \times 10^{-4}$ and $N_R = 32$ grid points are employed, stretched according to $\delta = 0.5$ and $A = 0.95$. In Fig. 6, we highlight the the tendency of the density profile to bend upwards in the vicinity of the wall when the $\widetilde{f}$ formulation is employed, while the χ approach matches the analytic solution with very high accuracy.

4. Summary

The simple tests considered in this Subsection highlight two important drawbacks of the $\widetilde{f}$ formulation. First, the trivial solution $f' = f'' = \text{const}$ cannot be fully recovered in this formulation, as shown in Fig. 4. This is in agreement with the discussion in Ref. [107]. Second, spurious terms are induced in the density profile in the vicinity of the boundaries. Even though the magnitude of these terms is small, they are not present in the χ formulation.

We thus conclude that the χ formulation is superior to the $\widetilde{f}$ one for the applications considered in this paper and thus discard the $\widetilde{f}$ formulation from the analysis presented in the following Sections. It is worth emphasizing that the conservation of the total number of particles is retained in the χ formulation, as highlighted in Ref. [113] (see also Sec. III D for more details).

D. Navier-Stokes regime

The hydrodynamic regime is achieved in kinetic theory by taking the limit when the Knudsen number satisfies $Kn \ll 1$. In the BGK formulation of the collision operator, we set the relaxation time in the form:

$$\tau = \frac{Kn}{nT},$$
(5.28)

where Kn is set to 10^{-3} in order to achieve the hydrodynamic regime. The form (5.28) for the relaxation time ensures that the viscosity μ and heat conductivity κ remain constant throughout the simulation, as implied by Eq. (2.38c).

The analytic solution of the Navier-Stokes equations is obtained in Subsec. V D 1. This solution is used in Subsecs. V D 2 and V D 3 to validate our implementation in the low and moderate Mach number regimes. The numerical simulations were performed by fixing the inner cylinder radius at $R_{\text{in}} = 1$, while the radius of the outer cylinder is allowed to vary in order to check the sensitivity of our implementation to curvature effects [53, 120, 121]. We thus set $R_{\text{out}} \in \{2, 4, 8, 16\}$, resulting in the radii ratios $\beta = R_{\text{in}}/R_{\text{out}} \in \{0.5, 0.25, 0.125, 0.0625\}$. The number of nodes employed is 64 and 96 for the low and non-negligible values of the Mach number, respectively, while the time step was set to $\delta t = 5 \times 10^{-4}$. Since in the hydrodynamic regime, the flow is close to equilibrium, the full-range Gauss-Hermite quadrature is employed on all momentum space directions.

1. Analytic analysis

In order to obtain the analytic solution in the Navier-Stokes regime, the constitutive equations (2.38a) and (2.38b) are employed for the nonequilibrium parts $\delta T^{\hat{a}\hat{b}}$ and $\delta q^{\hat{a}}$ in Eq. (2.34), where the transport coefficients μ and κ are assumed to be constant. The cylinders are assumed to have equal temperatures $T_{\text{in}} = T_{\text{out}} = T_w$, the outer cylinder is kept at rest (i.e. $\Omega_{\text{out}} = 0$), while the angular velocity Ω_{in} of the inner cylinder is left arbitrary. Noting that $\nabla_{\hat{a}} u^{\hat{a}} = 0$, the non-vanishing components of the stress-tensor are:

$$T^{\hat{R}\hat{R}} = T^{\hat{\varphi}\hat{\varphi}} = T^{\hat{z}\hat{z}} = P,$$
(5.29a)

$$T^{\hat{R}\hat{\varphi}} = -\mu R \frac{\partial}{\partial R}(R^{-1}u^{\hat{\varphi}}).$$
(5.29b)

Substituting Eq. (5.29b) into Eq. (5.16) gives the Navier-Stokes solution for the velocity [122, 123]:

$$u^{\hat{\varphi}} = R^{-1} \frac{\Omega_{\rm in}}{R_{\rm in}^{-2} - R_{\rm out}^{-2}} - R \frac{\Omega_{\rm in} R_{\rm in}^2}{R_{\rm out}^2 - R_{\rm in}^2}, \qquad (5.30)$$

where the conditions $u^{\hat{\varphi}}(R = R_{\rm in}) = \Omega_{\rm in} R_{\rm in}$ and $u^{\hat{\varphi}}(R = R_{\rm out}) = 0$ were imposed on the inner and outer cylinders, respectively. The tangential stress $T^{\hat{R}\hat{\varphi}}$ (5.16) reads:

$$T^{\hat{R}\hat{\varphi}} = T_{\rm in}^{\hat{R}\hat{\varphi}} \frac{R_{\rm in}^2}{R^2}, \qquad T_{\rm in}^{\hat{R}\hat{\varphi}} = \frac{2\mu \Omega_{\rm in} R_{\rm out}^2}{R_{\rm out}^2 - R_{\rm in}^2}. \qquad (5.31)$$

Next, the temperature can be obtained by substituting Eq. (2.38b) into Eq. (5.18):

$$T = T_w + \frac{\mu}{\kappa} \frac{\Omega_{\rm in}^2}{R_{\rm in}^{-2} - R_{\rm out}^{-2}}$$
$$\times \left[\frac{R_{\rm in}^{-2} - R^{-2}}{R_{\rm in}^{-2} - R_{\rm out}^{-2}} - \frac{\ln(R/R_{\rm in})}{\ln(R_{\rm out}/R_{\rm in})} \right], \quad (5.32)$$

where the boundary conditions $T(R = R_{\rm in}) = T(R = R_{\rm out}) = T_w$ were imposed. The heat flux $q^{\hat{R}} = -\kappa \partial_R T$ can be obtained as follows:

$$q^{\hat{R}} = -\frac{\mu}{R} \frac{\Omega_{\rm in}^2}{R_{\rm in}^{-2} - R_{\rm out}^{-2}}$$
$$\times \left[\frac{2R^{-2}}{R_{\rm in}^{-2} - R_{\rm out}^{-2}} - \frac{1}{\ln(R_{\rm out}/R_{\rm in})} \right], \quad (5.33)$$

while the constant Q in Eq. (5.18) is given by:

$$Q = \frac{\mu \Omega_{\rm in}^2}{R_{\rm in}^{-2} - R_{\rm out}^{-2}} \left[\frac{1}{\ln(R_{\rm out}/R_{\rm in})} - \frac{2R_{\rm in}^2}{R_{\rm out}^2 - R_{\rm in}^2} \right]. \quad (5.34)$$

Finally, the equation for the pressure can be obtained by substituting Eq. (5.29a) into Eq. (5.15a):

$$\partial_R \ln P = \frac{m(u^{\hat{\varphi}})^2}{RT}. \qquad (5.35)$$

To the best of our knowledge, the analytic solution of this equation is not known. Thus, the density profile $n = P/T$ must be computed using numerical methods, with the constraint that

$$2\pi \int_{R_{\rm in}}^{R_{\rm out}} nR dR = \pi(R_{\rm out}^2 - R_{\rm in}^2). \qquad (5.36)$$

2. Low Mach flows

The low Mach regime of the circular Couette flow has become a preferred benchmark test in the literature for models which deal with curved boundaries [43, 45, 53]. Since in this regime, the flow is essentially incompressible and isothermal, we only examine the azimuthal velocity $u^{\hat{\varphi}}$, which is represented in Fig. 7 for various values of
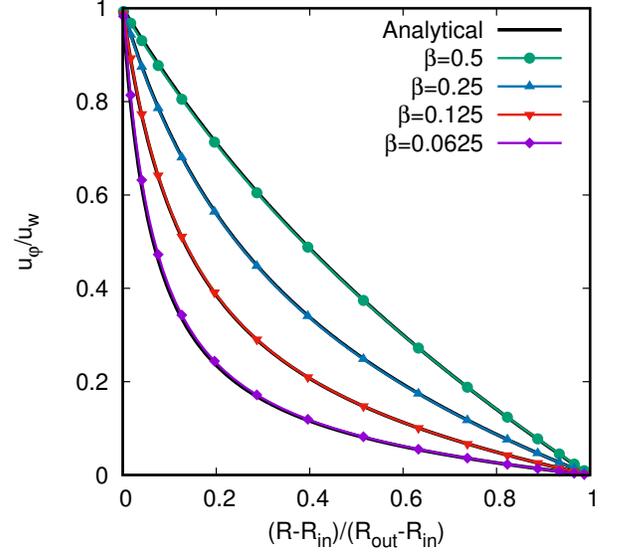
FIG. 7. Azimuthal velocity profile $u^{\hat{\varphi}}(R)$ for the angular velocity of the inner cylinder of $\Omega_{\rm in} = 0.01$. The curves correspond to various values of $\beta = R_{\rm in}/R_{\rm out}$. Our numerical results, obtained using the $H(2;3) \times H(2;3)$ model, are overlapped with the analytic solution (5.30).

$\beta = R_{\rm in}/R_{\rm out}$. In this regime, the analytic profiles can be recovered using the $H(2;3) \times H(2;3)$ model (employing $3 \times 3 = 9$ velocities), which is just the equivalent of the widely-used D2Q9 model employed in Refs. [45, 53]. However, the vielbein allows only one node to be used in the φ direction, thus bringing an improvement in the computational efficiency of several orders of magnitude compared to the implementations presented in Refs. [45, 53].

3. Non-negligible Mach flows

We now consider the case when the angular velocity of the inner wall is $\Omega_{\rm in} = 0.5$, such that $u_{\rm in}^{\varphi} = \Omega_{\rm in} R_{\rm in} = 0.5$.

Figure 8 shows a comparison between the results obtained using the $H(4;5) \times H(4;5)$ model against the analytical solution of the density n [computed numerically using Eq. (5.35)], tangential velocity $u^{\hat{\varphi}}$ (5.30), temperature T (5.32) and radial heat flux $q^{\hat{R}}$ (5.33). A very good agreement is observed with the analytic solution for all tested parameters. The temperature profile exhibits a maximum when

$$R = \sqrt{\frac{2\ln(R_{\rm out}/R_{\rm in})}{R_{\rm in}^{-2} - R_{\rm out}^{-2}}}. \qquad (5.37)$$

The above curve is also represented in Fig. 8(c) and it can be seen that the maximum is captured very well.

We note that the radial heat flow profiles are not well recovered near the boundaries, where a deviation with respect to the analytic profile can be seen. Figure 9 shows
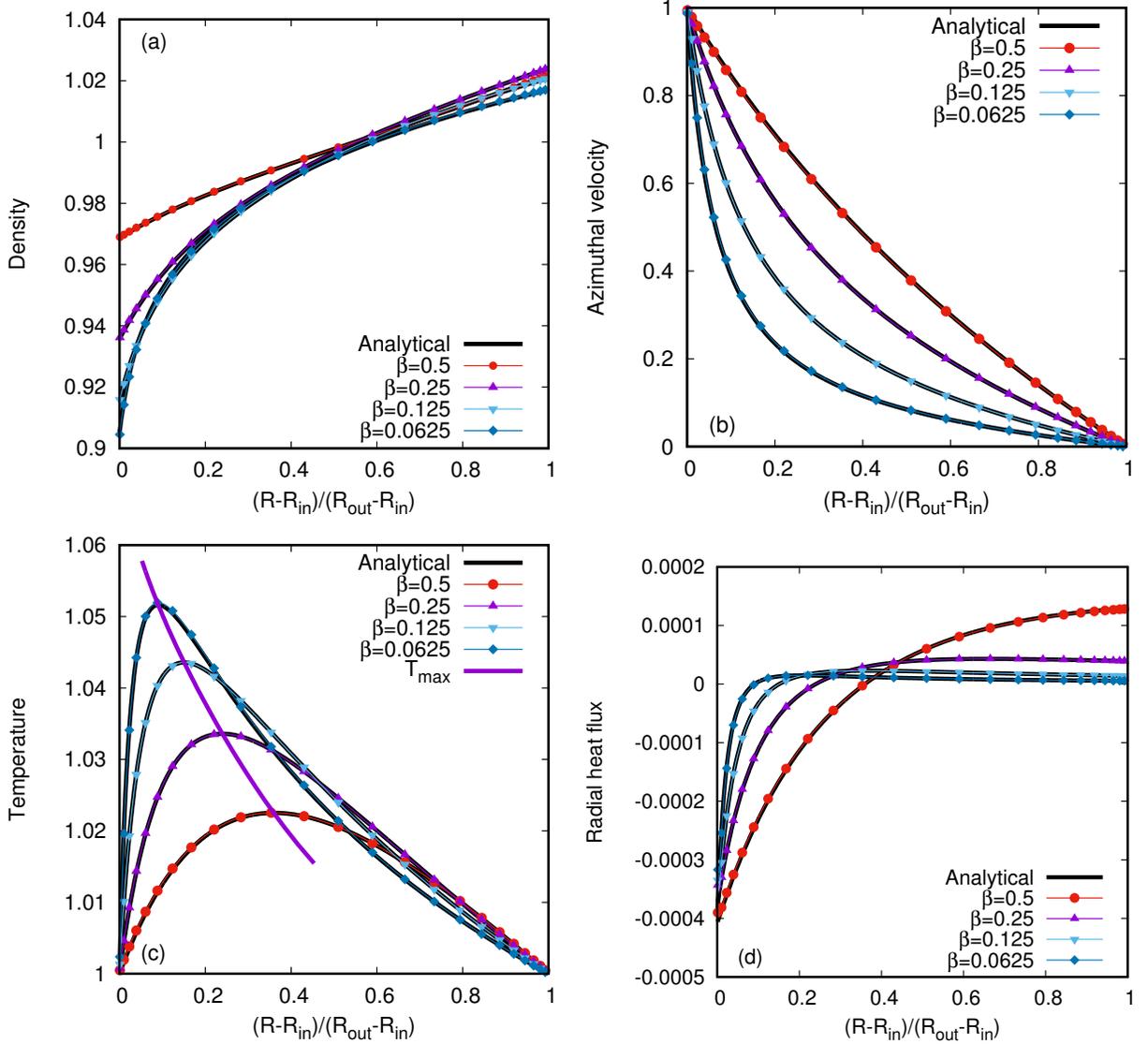
FIG. 8. Comparison between the numerical and analytic results for the profiles of (a) n [the theoretical value is computed numerically by solving Eq. (5.35)]; (b) $u^{\hat{\varphi}}$ (5.30); (c) T (5.32), together with Eq. (5.37) giving the position of the maximum in the temperature profile; (d) $q^{\hat{R}}$ (5.33). The curves correspond to various values of $\beta = R_{in}/R_{out}$. The inner cylinder rotates with $\Omega_{in} = 0.5$, while the outer cylinder is kept at rest. The numerical results, obtained using the H(4;5) × H(4;5) model, are overlapped with the analytic solutions.

the radial heat flux profile corresponding to equidistant grids having $N_R \in \{32, 64, 128, 256\}$ nodes and $\beta = 0.5$. It can be seen that this deviation occurs in the two points which are nearest to the boundary. By increasing the resolution in the vicinity of the boundary, the amplitude of the deviation of the numerical result compared to the analytic prediction (5.33) is seen to decrease roughly as $(\delta R)^{0.58}$. Figure 10 shows the comparison of the $\widetilde{f}$ and χ formulations with stretched and equidistant grids using $N_R = 32$ grid nodes. This plot clearly shows the advantage of using a stretched grid and the χ formulation, which appears to minimize the amplitude of the devia-

tions most efficiently out of the previously enumerated approaches.

E. Free molecular flow regime

In the free molecular flow regime, the collision term in the Boltzmann equation vanishes. The analytic solution in this case was derived in Ref. [88] only for the distribution function, density, azimuthal velocity and temperature. For completeness, we present a similar derivation for the distribution function and the macroscopic mo-
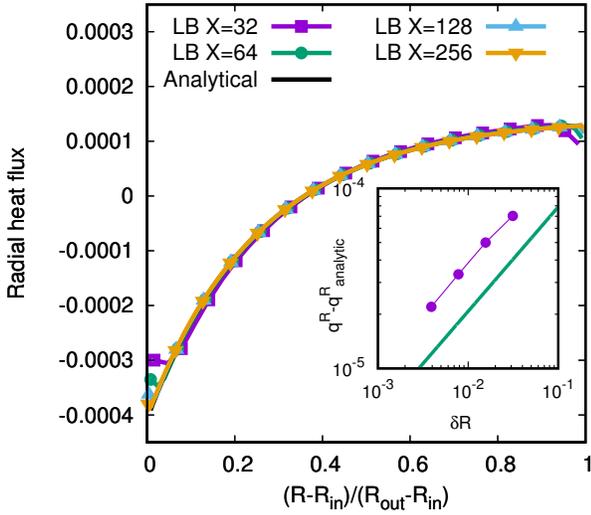
FIG. 9. Effect of lattice spacing on the behavior of $q^{\hat{R}}$ near the wall when an equidistant grid is employed. The inset shows that the amplitude of the deviation of $q^{\hat{R}}$ with respect to the expected analytic value (5.33) is proportional to $(\delta R)^{0.58}$.

ments (including the stress tensor and heat fluxes which are not derived in Ref. [88]), which are presented in Subsecs. V E 1 and V E 2, respectively. Our numerical scheme is validated by comparison with these results in Subsec. V E 3.
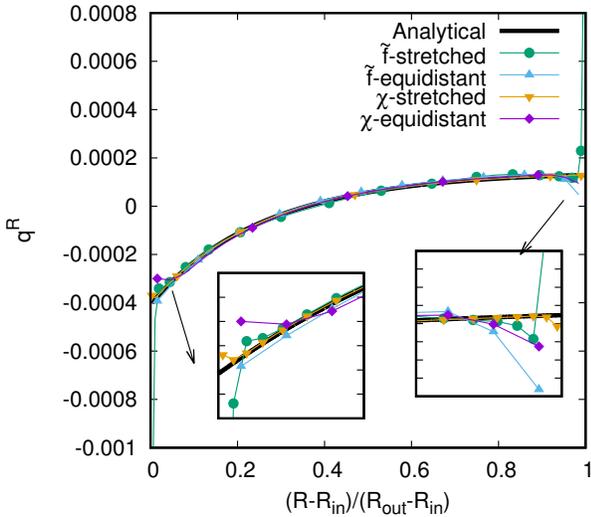
FIG. 10. Comparison of the $\widetilde{f}$ (stretched and equidistant) and χ (stretched and equidistant) radial heat flux using $N_R = 32$ grid points.
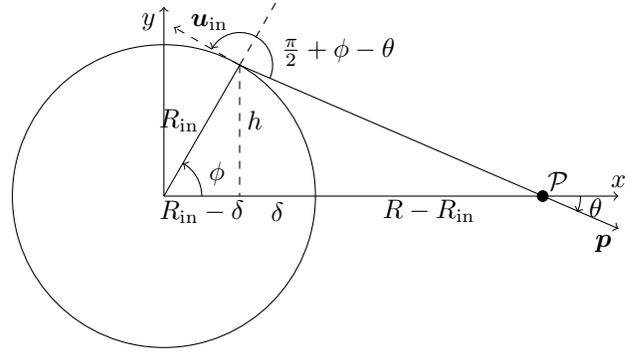
FIG. 11. Trajectory of a free-streaming particle originating from the inner cylinder, which passes through point $\mathcal{P}$ at distance R from the symmetry axis with momentum $\boldsymbol{p}$. Since the particle travels downwards, $\theta < 0$ and $\phi > 0$.

1. Boltzmann distribution function

Since there are no body forces present, the particles in the free molecular flow regime stream freely between the two bounding cylinders. Due to the symmetry of the flow configuration, the solution is independent of the azimuth φ. Let us consider a point $\mathcal{P}$ at a distance $R - R_{\rm in}$ from the first cylinder, as shown in Fig. 11. The momentum of a particle passing through this point has the components:

$$p^{\hat{R}} = p \cos\theta, \qquad p^{\hat{\varphi}} = p \sin\theta, \qquad (5.38)$$

where $p = \sqrt{(p^{\hat{R}})^2 + (p^{\hat{\varphi}})^2}$ and $\theta = \arctan(p^{\hat{\varphi}}/p^{\hat{R}})$. It is convenient to set the range of $\theta \in (-\pi, \pi)$ with $\theta = 0$ corresponding to the radial direction towards the outer cylinder. With this convention, the particles with $|\theta| < \theta_{\rm max} = \arcsin(R_{\rm in}/R)$ originate from the inner cylinder, while those with $\theta_{\rm max} < |\theta| < \pi$ are emitted by the outer cylinder. The coordinate axis x is aligned along the radial direction passing through $\mathcal{P}$, such that the radial and azimuthal unit vectors at $\mathcal{P}$ are just $\boldsymbol{i}$ and $\boldsymbol{j}$.

When $|\theta| < \theta_{\rm max}$, the distribution of particles at $\mathcal{P}$ having momentum $\boldsymbol{p}$ along the direction given by θ is equal to the distribution of particles emitted from the point located at $R_{\rm in}$ and angle $-\frac{\pi}{2} < \phi < \frac{\pi}{2}$ with respect to the horizontal axis, as shown in Fig. 11. We use the convention that the angle ϕ is positive when measured trigonometrically from the horizontal axis and negative otherwise. From Fig. 11 it can be seen that:

$$(\boldsymbol{p} - m\boldsymbol{u}_{\rm in})^2 = p^2 + p_z^2 + m^2 \Omega_{\rm in}^2 R_{\rm in}^2$$
$$- 2mp\Omega_{\rm in}R_{\rm in} \cos\left(\frac{\pi}{2} + \phi - \theta\right), \quad (5.39)$$

where $\boldsymbol{u}_{\rm in} = \Omega_{\rm in}R_{\rm in}(-\boldsymbol{i}\sin\phi + \boldsymbol{j}\cos\phi)$. In the above, it is understood that θ and ϕ have opposite signs, i.e. a particle travelling downwards ($\theta < 0$) originates from the upper half of the inner cylinder ($\phi > 0$), as shown in Fig. 11. The cosine function in Eq. (5.39) can be evalu-

ated as follows:

$$\cos\left(\frac{\pi}{2}+\phi-\theta\right)=\sin\theta(\cos\phi-\sin\phi\cot\theta)$$

$$=\frac{R}{R_{\rm in}}\sin\theta, \qquad (5.40)$$

where $\cos\phi=(R_{\rm in}-\delta)/R_{\rm in}$, $\sin\phi=\pm h/R_{\rm in}$ and $\cot\theta=\mp(R-R_{\rm in}+\delta)/h$, where the upper sign refers to the case when the particle is emitted from above the horizontal axis.

Thus, at radial distance R from the axis of the inner cylinder, the distribution function of particles travelling at angle θ with respect to the radial direction is:

$$f(R;\theta,p)=\frac{n_{\rm in}}{(2\pi mT_w)^{3/2}}\exp\left\{-\frac{1}{2mT_w}(p^2+p_z^2\right.$$
$$\left.+m^2\Omega_{\rm in}^2R_{\rm in}^2-2mp\Omega_{\rm in}R\sin\theta)\right\}, \quad (5.41)$$

where the number density of emitted particles $n_{\rm in}$ will be determined in Subsec. V E 2, T_w is the wall temperature and $|\theta|<\theta_{\rm max}=\arcsin(R_{\rm in}/R)$. Since the outer cylinder

is at rest, the distribution function of the emitted particles is isotropic, such that, when $\theta_{\rm max}<|\theta|<\pi$, the distribution function is given by:

$$f(R;\theta,p)=\frac{n_{\rm out}}{(2\pi mT_w)^{3/2}}\exp\left[-\frac{p^2+p_z^2}{2mT_w}\right], \qquad (5.42)$$

where the number density $n_{\rm out}$ of the particles emitted by the outer cylinder will be determined in the next Subsection.

2. Macroscopic moments

Let us introduce the following moments:

$$M_{s_R,s_\varphi,s_z}\equiv\int_{-\infty}^{\infty}dp_{\hat{z}}\int_{-\infty}^{\infty}dp_{\hat{R}}\int_{-\infty}^{\infty}dp_{\hat{\varphi}}\,f\,p_{\hat{R}}^{s_R}p_{\hat{\varphi}}^{s_\varphi}p_{\hat{z}}^{s_z}$$
$$=\int_{-\infty}^{\infty}dp_{\hat{z}}\,p_{\hat{z}}^{s_z}\int_0^{\infty}dp\,p^{s_R+s_\varphi+1}$$
$$\times\int_{-\pi}^{\pi}d\theta\,f\,(\cos\theta)^{s_R}(\sin\theta)^{s_\varphi}. \quad (5.43)$$

Using the results (5.41) and (5.42), the above expression can be written as:

$$M_{s_R,s_\varphi,s_z}=\frac{1+(-1)^{s_z}}{2\pi^{3/2}}(2mT_w)^{\frac{1}{2}(s_R+s_\varphi+s_z)}\Gamma\left(\frac{s_z+1}{2}\right)\left\{\right.$$
$$\frac{n_{\rm in}e^{-\widetilde{R}_{\rm in}^2}}{\widetilde{R}^{s_\varphi+1}}\int_{-\widetilde{R}_{\rm in}}^{\widetilde{R}_{\rm in}}d\zeta\,\zeta^{s_\varphi}e^{\zeta^2}(1-\zeta^2/\widetilde{R}^2)^{\frac{1}{2}(s_R-1)}\int_0^{\infty}d\xi\,\xi^{s_R+s_\varphi+1}e^{-(\xi-\zeta)^2}$$
$$\left.+n_{\rm out}\Gamma\left[1+\frac{1}{2}(s_R+s_\varphi)\right]\frac{1+(-1)^{s_\varphi}}{2}\int_{\theta_{\rm max}}^{\pi}d\theta\,(\cos\theta)^{s_R}(\sin\theta)^{s_\varphi}\right\}, \quad (5.44)$$

where the changes of variables $\xi=p/\sqrt{2mT_w}$ and $\zeta=\widetilde{R}\sin\theta$ were performed. The notation

$$\widetilde{R}=\Omega_{\rm in}R\sqrt{m/2T_w} \qquad (5.45)$$

represents the square root of the ratio between the kinetic energy $\frac{m}{2}\Omega_{\rm in}^2R^2$ induced by the rigid rotation at R and the thermal energy T_w, while $\widetilde{R}_{\rm in}=\widetilde{R}R_{\rm in}/R$.

Noting that $\rho u_{\hat{R}}=M_{1,0,0}$, the macroscopic velocity along the radial direction can be computed as:

$$u_{\hat{R}}=\frac{R_{\rm in}}{\rho R}\sqrt{\frac{mT_w}{2\pi}}(n_{\rm in}-n_{\rm out}), \qquad (5.46)$$

where the integration with respect to ζ in Eq. (5.44) was performed first. In order to ensure vanishing mass transfer through the bounding cylinders, $u_{\hat{R}}$ must vanish at

$R=R_{\rm in}$ and at $R=R_{\rm out}$, requiring that:

$$n_{\rm in}=n_{\rm out}=n_w. \qquad (5.47)$$

In order to fix n_w, the particle number density $n=M_{0,0,0}$ must be computed:

$$n(R)=\frac{n_w}{\widetilde{R}\pi}e^{-\widetilde{R}_{\rm in}^2}\int_{-\widetilde{R}_{\rm in}}^{\widetilde{R}_{\rm in}}\frac{e^{\zeta^2}d\zeta}{\sqrt{1-\zeta^2/\widetilde{R}^2}}\int_0^{\infty}d\xi\,\xi\,e^{-(\xi-\zeta)^2}$$
$$+n_w(1-\theta_{\rm max}/\pi), \quad (5.48)$$

where $\theta_{\rm max}=\arcsin(R_{\rm in}/R)$. Using the following identity:

$$\int_0^{\infty}d\xi\,\xi\,e^{-(\xi-\zeta)^2}=\frac{1}{2}e^{-\zeta^2}+\frac{\sqrt{\pi}}{2}\zeta(1+\mathrm{erf}\,\zeta), \qquad (5.49)$$

the particle number density can be expressed as:

$$n(R) = n_w \left\{ 1 - \frac{\theta_{\max}}{\pi} + e^{-\widetilde{R}_{\text{in}}^2} \left[\frac{\theta_{\max}}{\pi} + \frac{I_0(\widetilde{R})}{\widetilde{R}\sqrt{\pi}} \right] \right\}, \tag{5.50}$$

where

$$I_n(\widetilde{R}) = \int_0^{\widetilde{R}_{\text{in}}} \frac{\zeta^{2n+1} d\zeta}{\sqrt{1 - \zeta^2/\widetilde{R}^2}} e^{\zeta^2} \text{erf}\zeta. \tag{5.51}$$

Since the radial integral in Eq. (5.36) cannot be performed analytically, we resort to numerical methods to find the value of n_w.

The macroscopic velocity along the φ direction can be computed by noting that $\rho u^{\hat{\varphi}} = M_{0,1,0}$:

$$\rho u^{\hat{\varphi}} = \frac{n_w e^{-\widetilde{R}_{\text{in}}^2}}{\pi \widetilde{R}^2} \sqrt{2mT_w} \int_{-\widetilde{R}_{\text{in}}}^{\widetilde{R}_{\text{in}}} \frac{\zeta d\zeta\, e^{\zeta^2}}{\sqrt{1 - \zeta^2/\widetilde{R}^2}}$$
$$\times \int_0^\infty d\xi\, \xi^2 e^{-(\xi-\zeta)^2}. \tag{5.52}$$

Using the following property:

$$\int_0^\infty d\xi\, \xi^2 [e^{-(\xi-\zeta)^2} - e^{-(\xi+\zeta)^2}]$$
$$= \zeta e^{-\zeta^2} + \frac{\sqrt{\pi}}{2}(1 + 2\zeta^2)\text{erf}(\zeta), \tag{5.53}$$

the azimuthal velocity can be written as:

$$u^{\hat{\varphi}} = \frac{n_w \Omega_{\text{in}} R}{2\pi n(R)} e^{-\widetilde{R}_{\text{in}}^2} \left\{ \arcsin \frac{R_{\text{in}}}{R} - \frac{R_{\text{in}}}{R} \sqrt{1 - \frac{R_{\text{in}}^2}{R^2}} \right.$$
$$\left. + \frac{\sqrt{\pi}}{\widetilde{R}^3}[I_0(\widetilde{R}) + 2I_1(\widetilde{R})] \right\}. \tag{5.54}$$

Noting that

$$I_0 = \frac{\widetilde{R}^3}{\sqrt{\pi}} \left(\theta_{\max} - \frac{R_{\text{in}}}{R} \sqrt{1 - \frac{R_{\text{in}}^2}{R^2}} \right) + O(\Omega_{\text{in}}^5),$$

$$I_1 = \frac{\widetilde{R}^5}{4\sqrt{\pi}} \left[3\theta_{\max} - \frac{R_{\text{in}}}{R} \sqrt{1 - \frac{R_{\text{in}}^2}{R^2}} \left(3 + 2\frac{R_{\text{in}}^2}{R^2} \right) \right]$$
$$+ O(\Omega_{\text{in}}^7), \tag{5.55}$$

it can be seen that, in the small Ω_{in} limit, Eq. (5.54) reduces to the expression in Refs. [43, 124]:

$$u^{\hat{\varphi}} = \frac{1}{\pi}\Omega_{\text{in}}R \left(\arcsin \frac{R_{\text{in}}}{R} - \frac{R_{\text{in}}}{R} \sqrt{1 - \frac{R_{\text{in}}^2}{R^2}} \right) + O(\Omega_{\text{in}}^3). \tag{5.56}$$

Finally, $u^{\hat{z}} = 0$ since $M_{s_R, s_\varphi, 1} = 0$ due to the $[1 + (-1)^{s_z}]/2$ prefactor in Eq. (5.44).

For the computation of the stress tensor, it can be seen that $T^{\hat{z}\hat{z}} = \frac{1}{m}M_{0,0,2}$ is given by:

$$T^{\hat{z}\hat{z}} = n(R)T_w. \tag{5.57}$$

Since $T^{\hat{R}\hat{z}} = \frac{1}{m}M_{1,0,1} = 0$ and $\frac{1}{m}T^{\hat{\varphi}\hat{z}} = M_{0,1,1} = 0$, the only non-vanishing non-diagonal component of the stress tensor is $T^{\hat{R}\hat{\varphi}} = \frac{1}{m}M_{1,1,0}$:

$$T^{\hat{R}\hat{\varphi}} = \frac{2n_w T_w}{\pi \widetilde{R}^2} e^{-\widetilde{R}_{\text{in}}^2} \int_0^\infty d\xi\, \xi^3 e^{-\xi^2} \int_{-\widetilde{R}_{\text{in}}}^{\widetilde{R}_{\text{in}}} d\zeta\, \zeta e^{2\xi\zeta}. \tag{5.58}$$

The above integrals can be performed analytically, yielding:

$$T^{\hat{R}\hat{\varphi}} = T_{\text{in}}^{\hat{R}\hat{\varphi}} \frac{R_{\text{in}}^2}{R^2}, \qquad T_{\text{in}}^{\hat{R}\hat{\varphi}} = \frac{n_w T_w}{\sqrt{\pi}} \widetilde{R}_{\text{in}}, \tag{5.59}$$

where, as before, $\widetilde{R}_{\text{in}} = \Omega_{\text{in}} R_{\text{in}} \sqrt{m/2T_w}$. The above expression is in agreement with the general result (5.16). The last non-vanishing components of the stress-tensor are $T^{\hat{R}\hat{R}} = \frac{1}{m}M_{2,0,0}$ and $T^{\hat{\varphi}\hat{\varphi}} = \frac{1}{m}M_{0,2,0} - \rho(u^{\hat{\varphi}})^2$, which have the following expressions:

$$T^{\hat{R}\hat{R}} = \frac{n_w T_w}{\pi} e^{-\widetilde{R}_{\text{in}}^2} \left\{ \frac{R_{\text{in}}}{4R}(4 + 2\widetilde{R}_{\text{in}}^2 - \widetilde{R}^2) \cos\theta_{\max} + \frac{1}{4}(4 + \widetilde{R}^2)\theta_{\max} + \frac{\sqrt{\pi}}{\widetilde{R}^3} \left[3\widetilde{R}^2 I_0 + (2\widetilde{R}^2 - 3)I_1 - 2I_2 \right] \right\}$$
$$+ n_w T_w \left(1 - \frac{\theta_{\max}}{\pi} - \frac{\sin 2\theta_{\max}}{2\pi} \right), \tag{5.60a}$$

$$T^{\hat{\varphi}\hat{\varphi}} = \frac{n_w T_w}{\pi} e^{-\widetilde{R}_{\text{in}}^2} \left[-\frac{R_{\text{in}}}{4R}(4 + 2\widetilde{R}_{\text{in}}^2 + 3\widetilde{R}^2) \cos\theta_{\max} + \frac{1}{4}(4 + 3\widetilde{R}^2)\theta_{\max} + \frac{\sqrt{\pi}}{\widetilde{R}^3}(3I_1 + 2I_2) \right]$$
$$+ n_w T_w \left(1 - \frac{\theta_{\max}}{\pi} + \frac{\sin 2\theta_{\max}}{2\pi} \right) - \rho(u^{\hat{\varphi}})^2. \tag{5.60b}$$

The temperature can be obtained as follows:

$$T = T_w - \frac{m}{d}(u^{\hat{\varphi}})^2 + \frac{n_w T_w \widetilde{R}^2}{d\pi n(R)} e^{-\widetilde{R}_{\text{in}}^2} \left[\theta_{\max} - \frac{R_{\text{in}}}{R} \cos\theta_{\max} + \frac{\sqrt{\pi}}{\widetilde{R}}(I_0 + 2I_1) \right], \tag{5.61}$$

where the number of dimensions d was kept explicitly to allow the above formula to be applied when the momentum space is two-dimensional.

Finally, the components of the heat flux can be written as:

$$q^{\hat{R}} = \frac{M_{3,0,0} + M_{1,2,0} + M_{1,0,2}}{2m^2} - u^{\hat{\varphi}} T^{\hat{R}\hat{\varphi}},$$

$$q^{\hat{\varphi}} = \frac{M_{2,1,0} + M_{0,3,0} + M_{0,1,2}}{2m^2} - u^{\hat{\varphi}} T^{\hat{\varphi}\hat{\varphi}}$$

$$- \frac{1}{2}\rho(u^{\hat{\varphi}})^3 - \frac{3}{2} n u^{\hat{\varphi}} T. \qquad (5.62)$$

Noting that $M_{1,0,2} = 0$, $q^{\hat{R}}$ can be expressed as in Eq. (5.18), with

$$Q = \frac{n_w R_{\rm in} T_{\rm in}^{3/2}}{\sqrt{2\pi m}} \widetilde{R}_{\rm in}^2, \qquad (5.63)$$

where the notation $\widetilde{R}_{\rm in}$ is defined in Eq. (5.45). The component $q^{\hat{\varphi}}$ can be obtained from Eq. (5.62) using:

$$\frac{M_{2,1,0} + M_{0,3,0}}{2m^2} = \frac{n_w T_w^{3/2} \widetilde{R} e^{-\widetilde{R}_{\rm in}^2}}{4\pi\sqrt{2m}} \left[\theta_{\max}(10 + 3\widetilde{R}^2) \right.$$

$$- \frac{R_{\rm in}}{R}(10 + 2\widetilde{R}_{\rm in}^2 + 3\widetilde{R}^2)\cos\theta_{\max}$$

$$\left. + \frac{2\sqrt{\pi}}{\widetilde{R}^3}(3I_0 + 12I_1 + 4I_2) \right]. \qquad (5.64)$$

as well as $\frac{1}{2m^2} M_{0,1,2} = \frac{1}{2} n T_w u^{\hat{\varphi}}$.

3. Numerical results

As also noted in Refs. [36, 43, 82], a sufficiently high quadrature order must be employed at high values of the relaxation time in order to avoid oscillations in the stationary state. Fig. 12 illustrates how increasing the radial quadrature order quenches the oscillation amplitude. We note that the quadrature order required to reduce the oscillations below a detectable level increases with the number of spatial grid points. Since we employ the fifth-order WENO-5 scheme together with an appropriate grid stretching, we are able to obtain accurate results with only 16 grid points and a quadrature order of $Q_R = 200$ [36].

We tested our models in the high-Mach regime by considering three values of the angular velocity of the inner cylinder, namely $\Omega_{\rm in} \in \{1, 2, 3\}$. In this case, we kept $R_{\rm in} = 1$ and $R_{\rm out} = 2$ fixed, such that $\beta = R_{\rm in}/R_{\rm out} = 0.5$. In order to ensure accuracy, we employed a number of 16 nodes along the radial direction and our time step was set to $\delta t = 2 \times 10^{-5}$. For these values of the parameters, we used the models $\mathrm{HH}(4; 200) \times \mathrm{HH}(4; 10)$ to ensure smooth profiles in the stationary state. Excellent agreement is found between our simulation results for the
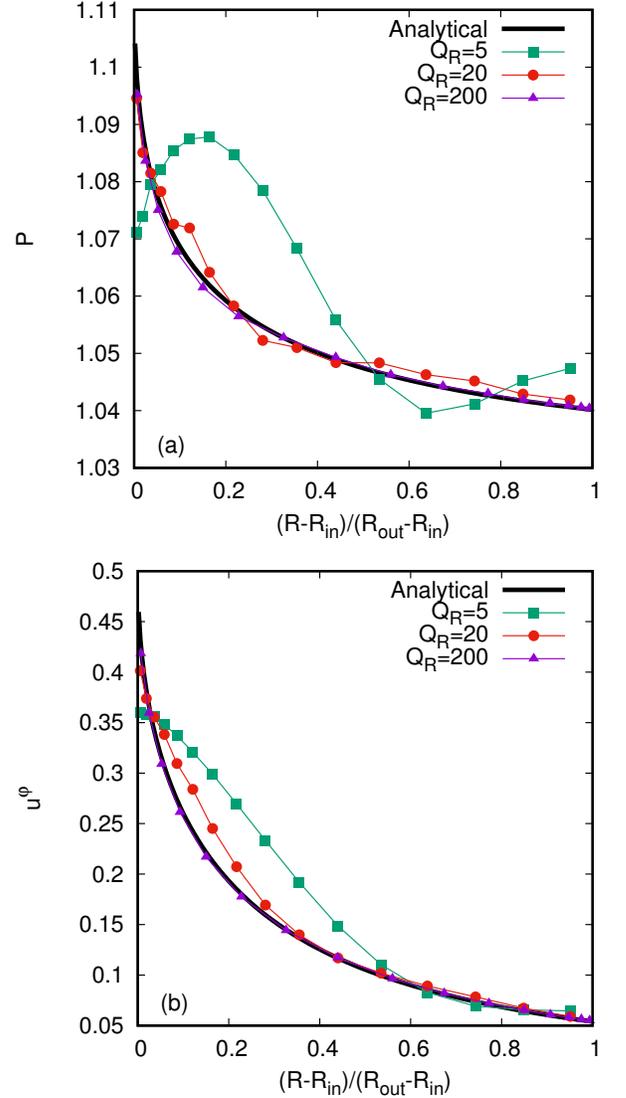
FIG. 12. Effect of the quadrature order on the oscillations in the stationary profile of the pressure and azimuthal velocity in the ballistic regime. The results were obtained with the models $\mathrm{HH}(4; Q_R) \times \mathrm{HH}(4; 10)$ and the curves correspond to various values of Q_R. The parameters employed in these simulations are: $R_{\rm in} = 1$, $R_{\rm out} = 2$, $\Omega_{\rm in} = 1.0$, $\Omega_{\rm out} = 0$ and $\delta t = 2 \times 10^{-5}$. Our simulations reached the stationary state after 500 000 iterations. We used $N_R = 16$ grid points together with the stretching given by $A = 0.95$ and $\delta = 0.75$. The thick continuous curve corresponds to the analytic solution (5.50).

profiles of P, $u^{\hat{\varphi}}$, $q^{\hat{R}}$, $q^{\hat{\varphi}}$, $T^{\hat{R}\hat{R}}$, $T^{\hat{\varphi}\hat{\varphi}}$, $T^{\hat{R}\hat{\varphi}}$ and temperature T and the corresponding analytic results derived in Sec. V E 2, as can be seen in Figs. 13 and 14.

Before ending this Section, it is worth emphasizing that the formula (5.56) derived by Willis [124] is valid only in the limit of low Mach number flows, as shown in Subsec. V E 2. At higher values of the Mach number, the ratio $u^{\hat{\varphi}}/u_w$ no longer coincides with the profile predicted
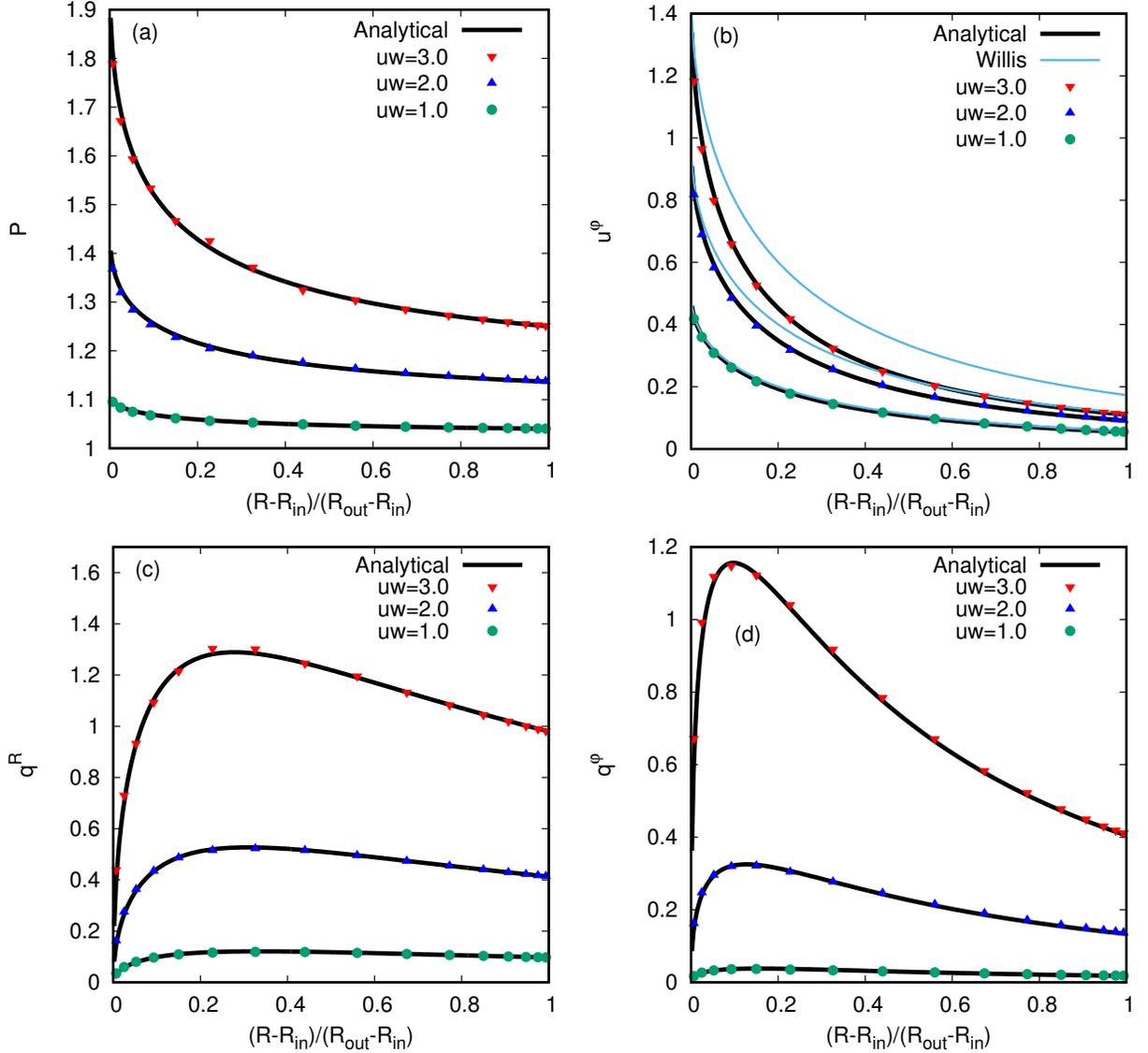
FIG. 13. Comparison between our numerical results and the analytic predictions in the ballistic regime. (a) $P = nT$ (5.50),(5.61); (b) $u^{\hat{\varphi}}/u^{\hat{\varphi}}_{\text{in}}$ (5.54); (c) $q^{\hat{R}}$ (5.62); (d) $q^{\hat{\varphi}}$ (5.62). The radii of the inner and outer cylinders were $R_{\text{in}} = 1$ and $R_{\text{out}} = 2$, such that $\beta = 0.5$. The quadrature used was HH(4; 200) × HH(4; 10). The curves correspond to various values of Ω_{in}. The analytic solution for $u^{\hat{\varphi}}$ reported by Willis [124] and reproduced in Eq. (5.56) is shown in (b) alongside the exact expression (5.54). The time step was set to $\delta t = 2 \times 10^{-5}$ and the number of nodes was $N_R = 16$.

by Willis, since the non-linear terms in $u^{\hat{\varphi}}$ which appear in the exact result (5.54) and are absent in the result from Willis (5.56) become important. This discrepancy is highlighted in Fig. 13(b).

F. Transition flow regime

To the best of our knowledge, there is no analytic solution of the Boltzmann-BGK equation which is valid for the circular Couette flow in the transition regime. In order to validate our models in this regime, we com-

pared our simulation results with those obtained by Aoki et al. [88] using a high-order Discrete Velocity Model (DVM) for $\text{Kn} \in \{0.02, 0.1, 1.0, 10.0\}$, where the Knudsen number is related to the relaxation time τ via [88]:

$$\tau = \frac{\text{Kn}}{n} \sqrt{\frac{\pi}{8}}. \qquad (5.65)$$

The angular velocity of the inner cylinder was set to $\Omega_{\text{in}} = 0.5\sqrt{2}$, while $\Omega_{\text{out}} = 0$. The radii of the inner and outer cylinders were kept fixed at $R_{\text{in}} = 1$ and $R_{\text{out}} = 2$. In order to maintain good agreement between our simulation results and those reported in Ref. [88], the ra-
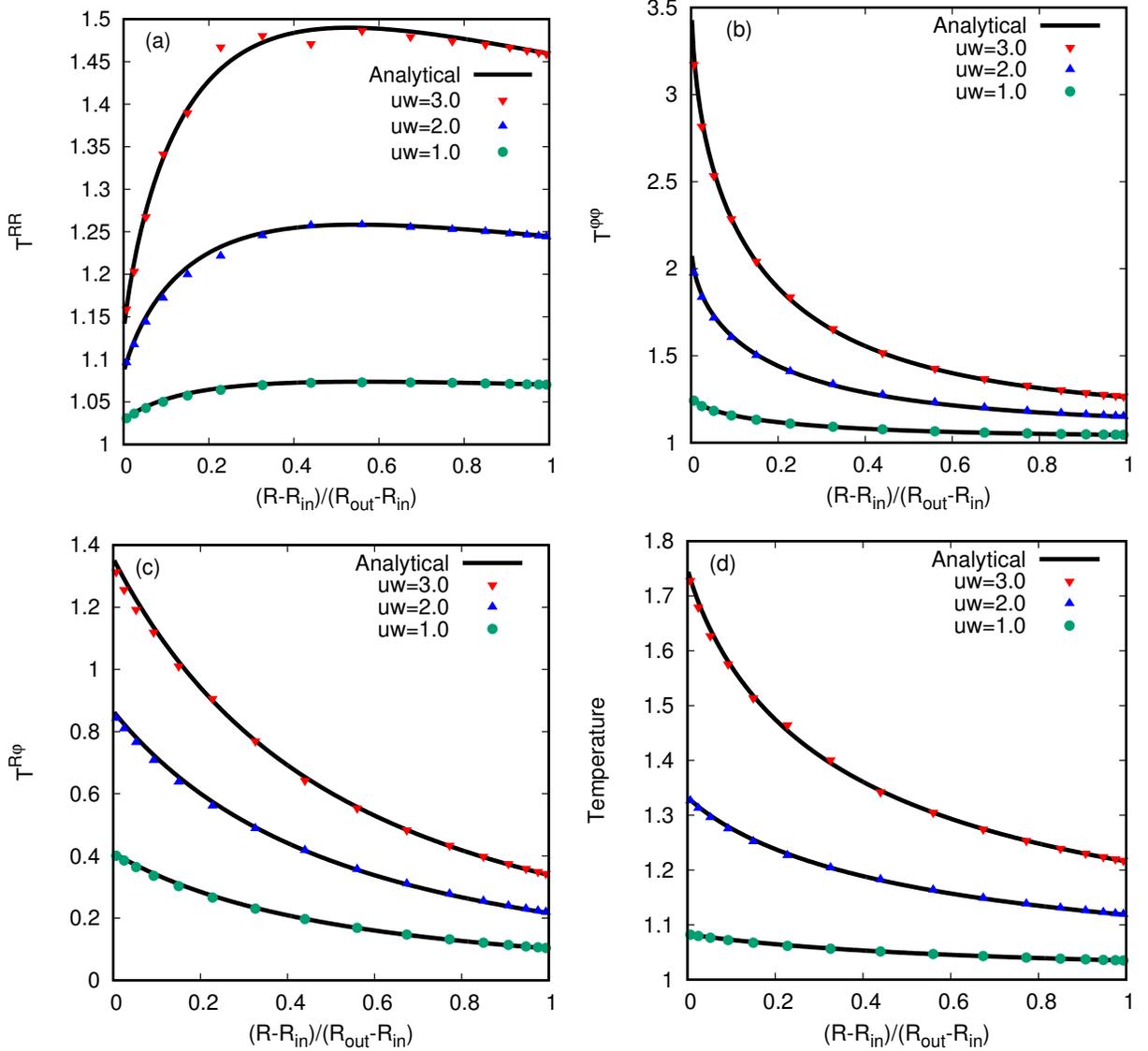
FIG. 14. Same as Fig. 13 in the case of: (a) $T^{\hat{R}\hat{R}}$ (5.60a); (b) $T^{\hat{\varphi}\hat{\varphi}}$ (5.60b); (c) $T^{\hat{R}\hat{\varphi}}$ (5.59); (d) T (5.61). The simulation parameters are the same as in Fig. 13.

dial and azimuthal quadrature orders were increased as Kn was increased, as summarized in Table III (the time step employed is also shown therein). The simulation domain comprised $N_R = 16$ nodes stretched according to Eq. (3.8) with $A = 0.95$ and $\delta = 0.5$.

Figures 15(a), 15(b) and 15(c) show comparisons between the profiles of n, T and $u^{\hat{\varphi}}$ obtained using the models summarized in Table III and those reported by Aoki et al. [88]. A very good agreement can be seen.

In Figures 16 (a) and 16(b), the variation over Kn of the constants Q (5.18) and $T_{\text{in}}^{\hat{R}\hat{\varphi}}$ (5.16) is represented. The simulation results match the analytic results in the hydrodynamic and ballistic flow regimes. For $T_{\text{in}}^{\hat{R}\hat{\varphi}}$, our numerical results are compared with the analytic result

obtained by Willis [124] and a good match is observed at high Knudsen numbers, close to the free molecular flow regime.

Finally, we considered the low Mach number case studied in Ref. [43]. Our simulation results obtained using the models summarized in Table III are shown in Fig. 17. An excellent match with the LB results reported by Watari in Ref. [43] can be observed.

G. Performance analysis

Let us now consider a comparison between the efficiency of our method and that of previously published methods. The lattice Boltzmann implementations em-
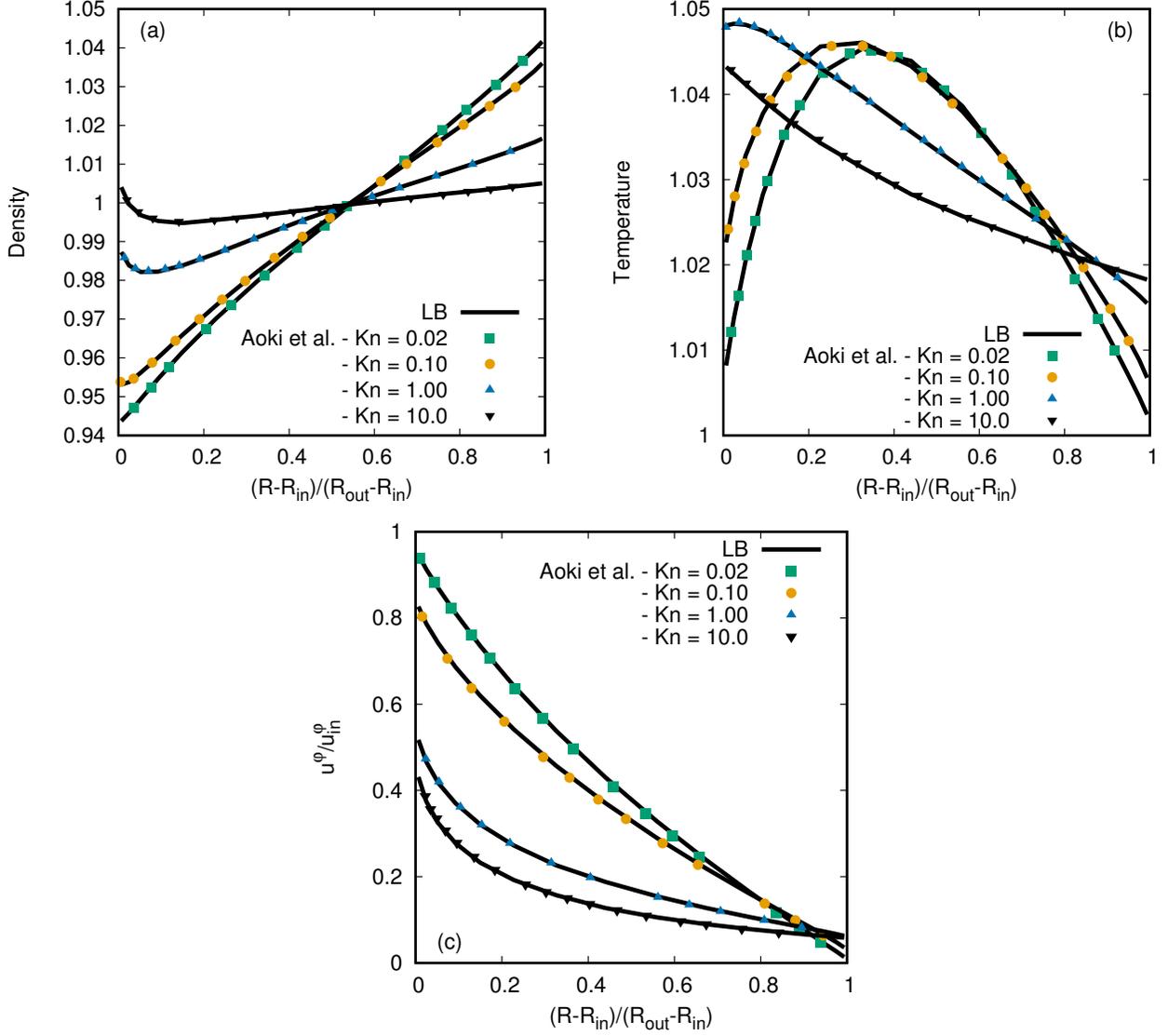
FIG. 15. Comparison between our simulation results and those reported in Ref. [88]. (a) $n(R)$; (b) $T(R)$; (c) $u^{\hat{\varphi}}(R)/u^{\hat{\varphi}}_{\text{in}}$. The angular velocity of the inner cylinder was set to $\Omega_{\text{in}} = 0.5\sqrt{2}$, while the Knudsen number is related to the relaxation time through Eq. (5.65). The models employed in these simulations are summarized in the *Non-negligible Mach* section of Table III.

ployed in Refs. [45, 53] are validated only in the hydrodynamic regime at small Mach numbers and employ the D2Q9 model (employing 9 velocities). Our scheme is capable of recovering this regime also with 9 velocities. However, the implementations of Refs. [45, 53] do not align the momentum space along the cylindrical coordinate system unit vectors, such that the spatial grid employed therein is two-dimensional. Thus, our proposed scheme is much more efficient, since our spatial grid is always one-dimensional.

Next, we consider a comparison with the LB implementation proposed by Watari in Ref. [43]. This scheme is also restricted to low Mach number flows, however, the whole range of the Knudsen number is explored. For Kn $\lesssim 0.5$, Watari employed models with 40 velocities in order to obtain accurate results. As Table III shows, our implementation allows us to recover the same results with 12 and 24 velocities at Kn = 0.01 and Kn = 0.1, respectively, while at Kn = 0.5, we employed a model with 120 velocities. At Kn = 1, Watari employed $4 \times 24 = 96$ velocities, while we required a number of 160 velocities to match the velocity profile. Finally, at Kn = 100, Watari obtained good agreement with the free-streaming solution with $4 \times 60 = 240$ velocities, while we employed 480 velocities in this regime. We note that our implementation requires higher quadrature orders at Kn $\gtrsim 0.5$ due to the inertial forces which act along the radial direction, where the distribution function is discontinuous. This

FIG. 17. Velocity profile in the low Mach number regime $\Omega_{\rm in} = 0.01$. Our simulation results are compared with the LB results reported by Watari in Ref. [43]. The models employed in these simulations are summarized in the *Low Mach* section of Table III alongside the corresponding time step. The number of grid points was $N_R = 16$, stretched according to Eq. (3.8) with $A = 0.95$ and $\delta = 0.5$.

FIG. 16. Comparison of our simulation results for the constants Q (a) and $T_{\rm in}^{\hat{R}\hat{\varphi}}$ (b) against the analytic solutions given in Eqs. (5.34) and (5.31) in the hydrodynamic limit, as well as in Eqs. (5.63) and (5.59) in the free molecular flow limit. The Knudsen number is related to the relaxation time through Eq. (5.65). In (b), the analytic result reported by Willis [124] is represented using a solid black line.

was also seen in the case of a rarefied gas between parallel plates under the effect of gravity [36]. Such forces are not present in the implementation of Ref. [43], since there the momentum space is not aligned to the cylindrical coordinate system. The gain in efficiency at the level of the momentum space compared to our scheme is lost since the spatial grid is two dimensional. The number of distribution functions required at Kn = 100 in Ref. [43] is 240 velocities multiplied by $200 \times 100 = 20000$ spatial grid points, resulting in $4\,800\,000$ population updates per time step. In our implementation, we only use 16 radial points, such that the number of population updates per time step is just $16 \times 480 = 7\,680$, which is significantly more efficient than the implementation presented

in Ref. [43].

In the transition regime, Aoki et al. [88] employed a polar decomposition of the momentum space using 48 shells of equal momentum magnitude containing 272 directions, resulting in a velocity set comprising $48 \times 272 = 13.056$ elements. As can be seen from Table III, the number of velocities employed by our models is significantly lower at Kn $\lesssim$ 10, with 40 velocities for Kn $\in \{0.02, 0.1\}$, 528 velocities at Kn = 1, and 960 velocities at Kn = 10. As Kn $\to \infty$, the number of velocities required to obtain accurate results increases to $8\,000$, which is still lower than the number of velocities employed in Ref. [88]. Furthermore, the use of the WENO-5 scheme for the computation of the numerical fluxes allows us to recover the analytic solutions in the ballistic regime using only 16 nodes, compared with the 240 nodes employed in Ref. [88] using the second order numerical scheme introduced in Refs. [125–127]. It can thus be seen that, as the ballistic regime is approached, the efficiency of our scheme decreases to that of standard DVM codes. However, in the regime of moderate Knudsen numbers, our implementation is significantly more efficient, especially due to the use of the half-range Gauss-Hermite quadrature on the radial direction. This can be seen by looking at Fig. 18, where the time required to achieve the steady state using the models benchmarked in Figs. 7, 8, 15 and 17 and summarized in Table III is represented with respect to Kn, for both the low and the high Mach regimes. It can be seen that the lowest runtime is registered around Kn $\simeq$ 0.1. For completeness, the methodology to deter-

mine this runtime is presented below.

In each of the simulations presented in Fig. 18, the time to achieve the steady state is determined by comparing the output of two successive cycles of duration $\Delta t = 6$ (the number of iterations per cycle is computed based on the time step). At the end of cycle $\ell > 1$, the following L_2 norms are computed:

$$L_{2;u}^\ell = \left[\int_{R_{\text{in}}}^{R_{\text{out}}} dR\, R \left(\frac{u_\ell^{\hat\varphi} - u_{\ell-1}^{\hat\varphi}}{u_w} \right)^2 \right]^{1/2},$$

$$L_{2;n}^\ell = \left[\int_{R_{\text{in}}}^{R_{\text{out}}} dR\, R \left(\frac{n_\ell}{n_{\ell-1}} - 1 \right)^2 \right]^{1/2},$$

$$L_{2;T}^\ell = \left[\int_{R_{\text{in}}}^{R_{\text{out}}} dR\, R \left(\frac{T_\ell}{T_{\ell-1}} - 1 \right)^2 \right]^{1/2}, \quad (5.66)$$

where u_w is the angular velocity of the inner cylinder (the outer cylinder is at rest), while $R_{\text{in}} = 1$ and $R_{\text{out}} = 2$ are the radii of the inner and outer cylinders. The integration is performed using the rectangle method by switching to the equidistant coordinate η, as described below for an arbitrary function $\mathfrak{f}$:

$$\int_{R_{\text{in}}}^{R_{\text{out}}} dR\, R\, \mathfrak{f}(R) = \frac{A_0}{A}(R_{\text{out}} - R_{\text{in}}) \int_{\eta_{\text{in}}}^{\eta_{\text{out}}} \frac{R(\eta)d\eta}{\cosh^2 \eta} \mathfrak{f}(\eta)$$

$$\simeq \frac{A_0}{A}(R_{\text{out}} - R_{\text{in}}) \sum_{s=1}^{N_R} \frac{R_s \delta\eta}{\cosh^2 \eta_s} \mathfrak{f}_s, \quad (5.67)$$

where the quantities bearing the subscript s are evaluated at $\eta = \eta_s = \eta_{\text{in}} + (s - 0.5)\delta\eta$. We consider that the steady state is achieved when all the L_2 norms defined in Eq. (5.66) decrease below the threshold 10^{-5}.

Let us now discuss the order of algorithmic complexity of the main steps of our proposed algorithm, namely:

1. Computation of the macroscopic variables;

2. Relaxation;

3. Enforcing boundary conditions;

4. Applying the advection rule;

5. Applying the forcing terms.

The order of the above steps is arbitrary, since we use a fully explicit algorithm and the new populations are stored in a separate memory zone. The complexity of steps 1, 2 and 4 is $O(N_{\text{vel}} \times N_R)$, where $N_{\text{vel}} = 2Q_R Q_\varphi$ is the total number of velocities when the half-range and full-range quadratures of orders Q_R and Q_φ are employed on the radial and azimuthal directions, while N_R is the number of nodes in the radial direction. Step 3 does not depend on the number of nodes (there are only two sites where diffuse reflection is applied for the circular Couette problem), so the complexity of this step is $O(N_{\text{vel}})$. Finally, step 5 involves the computation of the momentum space derivatives, which are performed using the kernels introduced in Sec. IV C and in Appendix D. It can be seen that the complexity for this step is $O[(Q_R + Q_\varphi) \times N_{\text{vel}} \times N_R]$. Thus, the time required to perform one iteration can be estimated via:

$$\Delta T = (a_1 + a_2 + a_4)N_{\text{vel}}N_R + a_3 N_{\text{vel}}$$
$$+ a_5(2Q_R + Q_\varphi)N_{\text{vel}}N_R + c, \quad (5.68)$$

where a_i ($1 \le i \le 5$) are constants corresponding to the steps of the algorithm and the constant c denotes an overhead which is due to one-off operations, such as memory allocations, input/output operations, etc.

We now consider a series of simulations in order to validate Eq. (5.68). For simplicity, the number of nodes is kept constant at $N_R = 128$, such that Eq. (5.68) becomes:

$$\Delta T = aN_{\text{vel}} + b(2Q_R + Q_\varphi)N_{\text{vel}} + c, \quad (5.69)$$

where a, b and c are constants. We now consider three batches of simulations. In the first batch, the radial and azimuthal quadrature orders are varied simultaneously, such that $Q_R = Q_\varphi = Q$, where $4 \le Q \le 30$. In this case, $Q = \sqrt{N_{\text{vel}}/2}$ and Eq. (5.69) reduces to:

$$\Delta T = aN_{\text{vel}} + \frac{3b}{\sqrt{2}} N_{\text{vel}}^{3/2} + c. \quad (5.70)$$

The second batch corresponds to keeping $Q_R = 4$ and varying Q_φ between 4 and 200, such that $Q_\varphi = N_{\text{vel}}/8$ and Eq. (5.69) becomes:

$$\Delta T = aN_{\text{vel}} + bN_{\text{vel}}\left(8 + \frac{N_{\text{vel}}}{8}\right). \quad (5.71)$$

Finally, in the third simulation batch, $Q_\varphi = 4$ is kept fixed and $Q_R = N_{\text{vel}}/8$ is varied between 4 and 200, while ΔT (5.69) is given by:

$$\Delta T = aN_{\text{vel}} + bN_{\text{vel}}\left(4 + \frac{N_{\text{vel}}}{4}\right). \quad (5.72)$$

The time per iteration ΔT can be used to compute the number of million of sites updated per second (Msites/s), which we denote by MS, being given by:

$$\text{MS} = \frac{N_R}{10^6 \Delta T}, \quad (5.73)$$

where ΔT is expressed in seconds. In order to validate Eq. (5.69), MS is computed by measuring the total simulation time T required to complete $32\,000/N_{\text{vel}}$ iterations for a system with $N_R = 128$ nodes stretched according to $\delta = 0.5$ and $A = 0.95$, with $\tau = \text{Kn}/n$, $\text{Kn} = 0.001$ and time step taken as $\delta t = 10^{-5}$ in order to satisfy the CFL condition for all quadrature orders considered in these simulations, by using the formula:

$$\text{MS} = \frac{0.32 N_R}{N_{\text{vel}} T}, \quad (5.74)$$
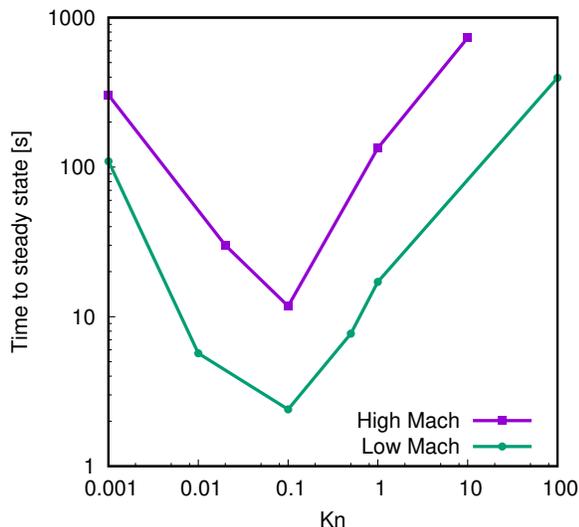
FIG. 18. Time (in seconds) required to achieve steady state using the models summarized in Table III.

FIG. 19. Number of millions of site updates per second in the context of the circular Couette flow for a system with $N_R = 128$ nodes in the radial direction when the half-range and full-range Gauss-Hermite quadratures of orders Q_R and Q_φ are employed on the radial and azimuthal directions, respectively. The total number of velocities is $N_{vel} = 2Q_R Q_\varphi$. The curves correspond to the cases when $Q_R = Q_\varphi$; when $Q_R = 4$ is kept fixed and Q_φ is varied; and when $Q_\varphi = 4$ is kept fixed and Q_R is varied. The simulation data are represented using lines with points, while the solid lines correspond to Eqs. (5.70), (5.71) and (5.72), where the parameters a,b and c are obtained using a fitting routine.

where T is given in seconds. Figure 19 shows the dependence of MS with respect to N_{vel} for the three batches considered above. For each simulation batch, the corresponding formula (5.70)–(5.72) is fitted to the numerical values of MS in order to determine the coefficients a, b and c. Taking the average between the three sets of values gives $a \simeq 42.4$ μs, $b \simeq 0.944$ μs and $c \simeq 198$ μs. The curves corresponding to Eqs. (5.70)–(5.72) with the above values for a, b and c are represented alongside the numerical data and an excellent agreement can be seen. This validates the algorithmic complexity proposed in Eq. (5.68).

For consistency, all runtime results are calculated for simulations performed on a single core of an Intel©Core™ i7-4790 Processor.

H. Summary

In this Section, the circular Couette problem was considered at various values of the Knudsen number, in the low and moderate Mach number regimes. Our numerical results reproduced with high accuracy the analytic solutions in the hydrodynamic and ballistic regimes, while at intermediate relaxation times, we obtained excellent agreement with the discrete velocity model (DVM) results reported in Ref. [88].

VI. FLOW THROUGH A GRADUALLY EXPANDING CHANNEL

In this Section, the versatility of the vielbein formalism is demonstrated in the case of a more complex geometry. The implementation is validated for the case of the gradually expanding channel problem initially proposed

in Ref. [100]. This type of channel has the advantage that the transition from a narrow to a wide channel opening is made gradually, without resorting to sharp corners.

Benchmark results were published in Ref. [101] for the incompressible Navier-Stokes flow through this channel at Reynolds number Re = 100 in the no-slip regime. In this Section, we validate our implementation against these benchmark results and further exploit the vielbein formalism in order to study the properties of the flow at non-negligible values of the Knudsen number Kn. In particular, we consider flow regimes with Mach numbers of order unity, as well as with Kn $\simeq 0.5$.

In Subsec. VI A, we introduce the vielbein for the general case of channels with symmetric walls and show how the momentum space can be aligned along them. The case of the gradually expanding channel is presented in Subsec. VI B, where the grid construction is discussed. The inlet and outlet boundary conditions, as well as specular and diffuse reflection boundary conditions on the channel centerline and channel walls, respectively, are discussed in Subsec. VI C. Our implementation is validated in the incompressible hydrodynamic regime in Subsec. VI D and simulations in the compressible hydrodynamic regime are presented in Subsec. VI E. To demonstrate the capabilities of the vielbein approach coupled with half-range quadratures, the flow through the grad-

ually expanding channel is considered for non-negligible values of the Knudsen number in Subsec. VI F.

A. General formalism

Let us consider the general case of a channel exhibiting a gradual symmetric modification of its exterior boundary. Let the top boundary be given by the function $x_{\text{top}}(y) = \frac{H}{2}[1 + \phi(y)]$, while the bottom boundary is located at $x_{\text{bottom}}(y) = -x_{\text{top}}(y)$. The normalized tangent vector to the top boundary is:

$$t = \frac{\frac{H}{2}\phi'\boldsymbol{i} + \boldsymbol{j}}{\sqrt{1 + (\frac{H}{2}\phi')^2}}, \tag{6.1}$$

while the exterior normal can be obtained as:

$$n = t \times k = \frac{\boldsymbol{i} - \frac{H}{2}\phi'\boldsymbol{j}}{\sqrt{1 + (\frac{H}{2}\phi')^2}}. \tag{6.2}$$

The incoming flux from the fluid towards the boundary is comprised of the particles for which

$$\boldsymbol{p} \cdot \boldsymbol{n} = \frac{p^x - \frac{H}{2}\phi'p^y}{\sqrt{1 + (\frac{H}{2}\phi')^2}} > 0. \tag{6.3}$$

The above restriction cuts the momentum space in half along a plane given by the equation $p^x = \frac{H}{2}\phi'p^y$, which is point dependent due to the presence of ϕ'. This has the undesirable effect that it does not allow the construction of a quadrature rule for the momentum space which is the same throughout the fluid domain. In particular, the lattice Boltzmann models based on half-range quadratures are developed for the case when the boundary is orthogonal to one of the momentum space directions (e.g., p^x), such that the incoming and outgoing fluxes are obtained as momentum space integrals of the distribution function restricted to positive or negative values of the momentum component along this direction [16, 18–36].

In order to make the condition (6.3) point-independent, the following coordinates can be employed:

$$\lambda = \frac{x}{1 + \phi(y)}, \qquad \xi = y, \tag{6.4}$$

while z remains unchanged. The boundaries are now located at $\lambda = \pm H/2$. The metric $ds^2 = dx^2 + dy^2 + dz^2$ becomes:

$$ds^2 = \{[1 + \phi(\xi)]d\lambda + \lambda\phi'(\xi)d\xi\}^2 + d\xi^2 + dz^2. \tag{6.5}$$

By writing $ds^2 = g_{\tilde{i}\tilde{j}}dx^{\tilde{i}}dx^{\tilde{j}}$, it can be seen that the non-vanishing components $g_{\tilde{i}\tilde{j}}$ of the metric tensor are given by:

$$g_{\tilde{\lambda}\tilde{\lambda}} = [1 + \phi(\xi)]^2, \qquad g_{\tilde{\xi}\tilde{\xi}} = 1 + \lambda^2[\phi'(\xi)]^2,$$
$$g_{\tilde{\xi}\tilde{\lambda}} = g_{\tilde{\lambda}\tilde{\xi}} = \lambda[1 + \phi(\xi)]\phi'(\xi), \qquad g_{\tilde{z}\tilde{z}} = 1, \tag{6.6}$$

while $\sqrt{g} = \sqrt{g_{\tilde{\xi}}} = 1 + \phi(\xi)$. Thus, the metric tensor exhibits non-vanishing non-diagonal components.

The components of the momentum vector $\boldsymbol{p}$ with respect to the coordinates λ and ξ are:

$$p^{\tilde{\lambda}} = \frac{\partial\lambda}{\partial x}p^x + \frac{\partial\lambda}{\partial y}p^y = \frac{p^x - \lambda\phi'p^y}{1 + \phi},$$
$$p^{\tilde{\xi}} = \frac{\partial\xi}{\partial x}p^x + \frac{\partial\xi}{\partial y}p^y = p^y, \tag{6.7}$$

while the inverse transformation gives

$$p^x = (1 + \phi)p^{\tilde{\lambda}} + \lambda\phi'p^{\tilde{\xi}}, \qquad p^y = p^{\tilde{\xi}}. \tag{6.8}$$

It can be seen that at $\lambda = H/2$, $p^{\tilde{\lambda}}$ is proportional to $\boldsymbol{p} \cdot \boldsymbol{n}$, such that Eq. (6.3) reduces to:

$$p^{\tilde{\lambda}} > 0. \tag{6.9}$$

The coordinate directions ∂_λ and ∂_ξ are not orthogonal, since $g_{\tilde{\lambda}\tilde{\xi}} \neq 0$. This implies that the momentum vectors $\boldsymbol{p}_\lambda$ and $\boldsymbol{p}_\xi$, corresponding to $(p^{\tilde{\lambda}}, p^{\tilde{\xi}}) = (1, 0)$ and $(0, 1)$, respectively, are not orthogonal:

$$\boldsymbol{p}_\lambda \cdot \boldsymbol{p}_\xi = g_{\tilde{\lambda}\tilde{\xi}} = \lambda(1 + \phi)\phi'. \tag{6.10}$$

In order to construct an orthogonal momentum space which retains the beauty of Eq. (6.9), it is convenient to work with the following triad one-forms:

$$\omega^{\hat{\xi}} = \frac{\lambda\phi'(1 + \phi)}{\sqrt{1 + \lambda^2\phi'^2}}d\lambda + \sqrt{1 + \lambda^2\phi'^2}\,d\xi,$$
$$\omega^{\hat{\lambda}} = \frac{1 + \phi}{\sqrt{1 + \lambda^2\phi'^2}}d\lambda, \qquad \omega^{\hat{z}} = dz, \tag{6.11}$$

and the associated triad vectors:

$$e_{\hat{\lambda}} = \frac{\sqrt{1 + \lambda^2\phi'^2}}{1 + \phi}\partial_\lambda - \frac{\lambda\phi'}{\sqrt{1 + \lambda^2\phi'^2}}\partial_\xi,$$
$$e_{\hat{\xi}} = \frac{1}{\sqrt{1 + \lambda^2\phi'^2}}\partial_\xi, \qquad e_{\hat{z}} = \partial_z. \tag{6.12}$$

The connection between the hatted components $p^{\hat{\lambda}}$ and $p^{\hat{\xi}}$ and the Cartesian components p^x and p^y of $\boldsymbol{p} = p^{\hat{\lambda}}e_{\hat{\lambda}} + p^{\hat{\xi}}e_{\hat{\xi}} = p^x\boldsymbol{i} + p^y\boldsymbol{j}$ is given through:

$$p^{\hat{\lambda}} = \omega^{\hat{\lambda}}_{\tilde{\lambda}}p^{\tilde{\lambda}} + \omega^{\hat{\lambda}}_{\tilde{\xi}}p^{\tilde{\xi}} = \frac{p^x - \lambda\phi'p^y}{\sqrt{1 + \lambda^2(\phi')^2}}, \tag{6.13a}$$
$$p^{\hat{\xi}} = \omega^{\hat{\xi}}_{\tilde{\lambda}}p^{\tilde{\lambda}} + \omega^{\hat{\xi}}_{\tilde{\xi}}p^{\tilde{\xi}} = \frac{p^y + \lambda\phi'p^x}{\sqrt{1 + \lambda^2(\phi')^2}}. \tag{6.13b}$$

The inverse relations are:

$$p^x = \left(\frac{\partial x}{\partial \lambda}e_{\hat{\lambda}}^{\widetilde{\lambda}} + \frac{\partial x}{\partial \xi}e_{\hat{\lambda}}^{\widetilde{\xi}}\right)p^{\hat{\lambda}} + \left(\frac{\partial x}{\partial \lambda}e_{\hat{\xi}}^{\widetilde{\lambda}} + \frac{\partial x}{\partial \xi}e_{\hat{\xi}}^{\widetilde{\xi}}\right)p^{\hat{\xi}}$$

$$= \frac{p^{\hat{\lambda}} + \lambda\phi' p^{\hat{\xi}}}{\sqrt{1 + \lambda^2(\phi')^2}}, \tag{6.14a}$$

$$p^y = \left(\frac{\partial y}{\partial \lambda}e_{\hat{\lambda}}^{\widetilde{\lambda}} + \frac{\partial y}{\partial \xi}e_{\hat{\lambda}}^{\widetilde{\xi}}\right)p^{\hat{\lambda}} + \left(\frac{\partial y}{\partial \lambda}e_{\hat{\xi}}^{\widetilde{\lambda}} + \frac{\partial y}{\partial \xi}e_{\hat{\xi}}^{\widetilde{\xi}}\right)p^{\hat{\xi}}$$

$$= \frac{p^{\hat{\xi}} - \lambda\phi' p^{\hat{\lambda}}}{\sqrt{1 + \lambda^2(\phi')^2}}. \tag{6.14b}$$

It can be seen that at $\lambda = H/2$, $p^{\lambda} = \boldsymbol{p} \cdot \boldsymbol{n}$ (6.13a). Moreover, the triad vectors $e_{\hat{\lambda}}$ and $e_{\hat{\xi}}$ are orthogonal, thus ensuring that the vectors $\boldsymbol{p}_{\hat{\lambda}}$ and $\boldsymbol{p}_{\hat{\xi}}$ corresponding to $(p^{\hat{\lambda}}, p^{\hat{\xi}}) = (1, 0)$ and $(0, 1)$ are orthogonal:

$$\boldsymbol{p}_{\hat{\lambda}} \cdot \boldsymbol{p}_{\hat{\xi}} = g_{\widetilde{i}\widetilde{j}}e_{\hat{\lambda}}^{\widetilde{i}}e_{\hat{\xi}}^{\widetilde{j}} = \delta_{\hat{\lambda}\hat{\xi}} = 0. \tag{6.15}$$

Noting that the only non-vanishing commutator $[e_{\hat{\lambda}}, e_{\hat{\xi}}]$, gives rise to the following connection and Cartan coefficients:

$$\Gamma_{\hat{\lambda}\hat{\xi}\hat{\xi}} = c_{\hat{\lambda}\hat{\xi}\hat{\xi}} = \frac{\lambda\phi''}{(1 + \lambda^2\phi'^2)^{3/2}},$$

$$\Gamma_{\hat{\lambda}\hat{\xi}\hat{\lambda}} = c_{\hat{\lambda}\hat{\xi}\hat{\lambda}} = \frac{\phi'[1 + \lambda^2\phi'^2 - \lambda^2\phi''(1 + \phi)]}{(1 + \phi)(1 + \lambda^2\phi'^2)^{3/2}}, \tag{6.16}$$

the Boltzmann equation (2.24) can be written as:

$$\frac{\partial f}{\partial t} + \frac{\partial(V^{\lambda}f)}{\partial \lambda} + \frac{\partial(V^{\xi}f)}{\partial \chi^{\xi}}$$
$$- \frac{1}{m}\Gamma_{\hat{\lambda}\hat{\xi}\hat{\xi}}\left[(p^{\hat{\xi}})^2\frac{\partial f}{\partial p^{\hat{\lambda}}} - p^{\hat{\lambda}}\frac{\partial(fp^{\hat{\xi}})}{\partial p^{\hat{\xi}}}\right]$$
$$- \frac{1}{m}\Gamma_{\hat{\xi}\hat{\lambda}\hat{\lambda}}\left[(p^{\hat{\lambda}})^2\frac{\partial f}{\partial p^{\hat{\xi}}} - p^{\hat{\xi}}\frac{\partial(fp^{\hat{\lambda}})}{\partial p^{\hat{\lambda}}}\right] = -\frac{1}{\tau}(f - f^{(\text{eq})}), \tag{6.17}$$

where homogeneity with respect to the z coordinate was assumed and the following notation was introduced:

$$V^{\lambda} = \frac{\sqrt{1 + \lambda^2\phi'^2}}{1 + \phi}\frac{p^{\hat{\lambda}}}{m},$$

$$V^{\xi} = (1 + \phi)\frac{p^{\hat{\xi}} - \lambda\phi' p^{\hat{\lambda}}}{m\sqrt{1 + \lambda^2\phi'^2}} = (1 + \phi)\frac{p^y}{m}, \tag{6.18}$$

while χ^{ξ} is defined through:

$$d\chi^{\xi} = (1 + \phi)d\xi. \tag{6.19}$$

Since the channel is symmetric with respect to the central line located at $\lambda = 0$, the fluid flow is simulated only in the upper half ($0 < \lambda < H/2$). The fluid domain is thus represented by the rectangle in the (ξ, λ) space

defined by $\xi_{\text{in}} < \xi < \xi_{\text{out}}$ and $0 < \lambda < H/2$. The non-dimensionalization convention is such that $H/2 = 1$. The λ direction is further stretched towards the solid boundary according to the coordinate transformation (3.8) with $\lambda_{\text{left}} = 0$, $\lambda_{\text{right}} = H/2$ and $\delta = 0$, as follows:

$$\lambda(\eta) = \frac{H}{2A}\tanh\eta, \tag{6.20}$$

where $A = 0.95$ for all simulations presented in this Section. The resulting grid is shown in Figs. 20(a) and (b) with respect to the (x, y) and (λ, ξ) coordinates, respectively, for the wall function $\phi(\xi)$ corresponding to the gradually expanding channel, given in Eq. (6.24).

The fluid domain in the (η, ξ) variables is divided into $N_{\eta} \times N_{\xi}$ equally sized cells (where $N_{\eta} = N_{\lambda}$) centered on coordinates (λ_s, ξ_p), where $\lambda_s \equiv \lambda(\eta_s)$ and $1 \leq s \leq N_{\lambda}$, $1 \leq p \leq N_{\xi}$, while

$$\eta_s = \frac{s - 0.5}{N_{\lambda}}\text{arctanh}A,$$

$$\xi_p = \xi_{\text{in}} + \frac{p - 0.5}{N_{\xi}}(\xi_{\text{out}} - \xi_{\text{in}}). \tag{6.21}$$

Inlet and outlet boundary conditions are imposed at $\xi = \xi_{\text{in}}$ and $\xi = \xi_{\text{out}}$, respectively, while specular and diffuse reflection boundary conditions are imposed at $\lambda = 0$ and $\lambda = H/2$, respectively, as shown in Fig. 20(b).

In order to ensure that $f = \text{const}$ is accepted as a numerical solution, the connection coefficients in Eq. (6.16) are implemented as follows:

$$(\Gamma_{\hat{\lambda}\hat{\xi}\hat{\lambda}})_{s,p} = \frac{1}{\delta\chi_{s,p}^{\xi}}\left(\frac{1 + \phi_{p+1/2}}{\sqrt{1 + \lambda_s^2\phi_{p+1/2}'^2}} - \frac{1 + \phi_{p-1/2}}{\sqrt{1 + \lambda_s^2\phi_{p-1/2}'^2}}\right),$$

$$(\Gamma_{\hat{\lambda}\hat{\xi}\hat{\xi}})_{s,p} = -\frac{\sqrt{1 + \lambda_{s+1/2}^2\phi_p'^2} - \sqrt{1 + \lambda_{s-1/2}^2\phi_p'^2}}{\delta\lambda_s(1 + \phi_p)}$$

$$+ \frac{\lambda_s}{\delta\chi_{s,p}^{\xi}}\left(\frac{\phi_{p+1/2}'(1 + \phi_{p+1/2})}{\sqrt{1 + \lambda_s^2\phi_{p+1/2}'^2}} - \frac{\phi_{p-1/2}'(1 + \phi_{p-1/2})}{\sqrt{1 + \lambda_s^2\phi_{p-1/2}'^2}}\right) \tag{6.22}$$

where $\delta\chi_{s,p}^{\xi} = \chi_{s,p+1/2}^{\xi} - \chi_{s,p-1/2}^{\xi}$ and $\delta\lambda_s = \lambda_{s+1/2} - \lambda_{s-1/2}$.

For the remainder of this Section, we consider the reduced form of Eq. (6.17), obtained by multiplying Eq. (6.17) by 1 and $(p^{\hat{z}})^2/m$ followed by an integration over the $p^{\hat{z}}$ momentum space axis, as described in Sec. IV A. The resulting equations for f' (f'') are identical with Eq. (6.17), with f and $f^{(\text{eq})}$ replaced by f' (f'') and $f'_{(\text{eq})}$ ($f''_{(\text{eq})}$), respectively. In order to ensure constant transport coefficients, the relaxation time is implemented as follows:

$$\tau = \frac{\text{Kn}}{nT}. \tag{6.23}$$
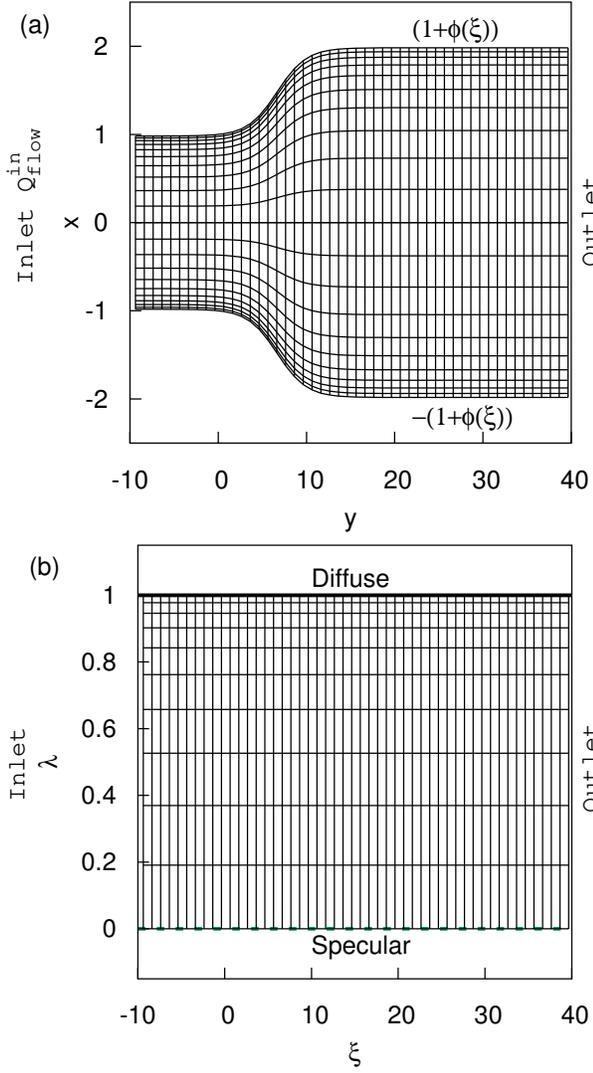
FIG. 20. (a) Geometry of the gradually expanding channel for $\mathrm{Re}_c = 100$. The vertical lines correspond to constant values of ξ chosen equidistantly between -10 and 40. The horizontal lines are drawn at constant values of λ which are stretched towards the boundaries via Eq. (6.20). (b) Fluid domain in (λ, ξ) coordinates, corresponding to the upper half of the channel.

FIG. 21. The orientation of the principal axes of the momentum space expressed with respect to the vielbein. The vectors $\boldsymbol{p}_{\hat{\lambda}} = e_{\hat{\lambda}}$ and $\boldsymbol{p}_{\hat{\xi}} = e_{\hat{\xi}}$ can be regarded as unit vectors along these axes. The vertical lines correspond to constant values of ξ, while the horizontal lines represent lines of constant values of λ. The geometry corresponds to setting $\mathrm{Re}_c = 6$ in Eq. (6.24).

B. Gradually expanding channel

We now turn to the particular case of the gradually expanding channel proposed in Refs. [100, 101], for which the function $\phi(\xi)$ defining the position of the wall is given as

$$\phi(\xi) = \frac{1}{2}\left[\tanh(2) - \tanh\left(2 - \frac{30}{\mathrm{Re}_c}\frac{2\xi}{H}\right)\right]. \quad (6.24)$$

The parameter Re_c controls the steepness of the expanding portion (i.e., its horizontal span). When Re_c is equal to the Reynolds number Re of the flow, the flow features become independent of $\mathrm{Re} = \mathrm{Re}_c$ in the region $0 < 2\xi/H < \mathrm{Re}/3$ as $\mathrm{Re} \to \infty$. In particular, the

flow configuration at $\mathrm{Re} = \mathrm{Re}_c = 100$ is a good approximation for the $\mathrm{Re} \to \infty$ case [100]. In this Section, $\mathrm{Re}_c = 100$ is employed for all simulations, even when the Reynolds number of the flow Re differs from this value. The resulting geometry is shown in Fig. 20(a). Integrating Eq. (6.19) gives the following expression for χ^ξ:

$$\chi^\xi = \left(1 + \frac{\tanh 2}{2}\right)\xi + \frac{H\mathrm{Re}_c}{120}\ln\frac{\cosh(2 - 60\xi/H\mathrm{Re}_c)}{\cosh 2},$$
$$(6.25)$$

where the integration constant was fixed such that $\chi^\xi = 0$ when $\xi = 0$.

For all simulations performed in the gradually expanding channel, we used a grid comprised of $N_\lambda \times N_\xi =$

30 × 200 nodes. The relevant flow domain is bounded by $\xi = 0$ and $\xi = \mathrm{Re}_c/100 \simeq 33.33$. The inlet and outlet boundary conditions are imposed at $\xi = \xi_{\mathrm{in}} = -10$ and $\xi = \xi_{\mathrm{out}} = 40$, thus allowing some space for the flow to adjust itself before entering the investigated region.

In order to better understand the effect of employing the orthogonal triad, Fig. 21 shows the pair of vectors $(\boldsymbol{p}_{\hat{\lambda}}, \boldsymbol{p}_{\hat{\xi}}) = (e_{\hat{\lambda}}, e_{\hat{\xi}})$ at fixed ξ and for various values of λ, represented with respect to the (x, y) coordinate frame. In order to maintain the same scale on the horizontal and vertical axes, the figure is drawn for a channel with $\mathrm{Re}_c = 6$, for which the horizontal span of the expanding portion of the channel is comparable to its vertical span. It can be seen that the two vectors start from being parallel to the x and y axes on the horizontal axis ($\lambda = 0$) to being aligned perpendicular to, and along, the upper boundary for $\lambda = H/2$.

The momentum space defined with respect to the vielbein is discretized on the ξ and λ directions separately using $\mathcal{Q}_\xi \times \mathcal{Q}_\lambda$ velocities. On the ξ direction, which is parallel to the walls, the full-range Gauss-Hermite quadrature is used, such that $p^{\hat{\xi}} \to p_j^{\hat{\xi}}$ ($1 \leq j \leq Q_\xi$), where $p_j^{\hat{\xi}}$ are the roots of the Hermite polynomial $H_{Q_\xi}(p^{\hat{\xi}})$ of order Q_ξ. On the λ axis, the choice of quadrature depends on the value of Kn. The momentum components are indexed as $p_i^{\hat{\lambda}}$, where $1 \leq i \leq \mathcal{Q}_\lambda$ and $\mathcal{Q}_\lambda = Q_\lambda$ when the full-range Gauss-Hermite quadrature of order Q_λ is employed, while $\mathcal{Q}_\lambda = 2Q_\lambda$ for the case of the half-range Gauss-Hermite quadrature of order Q_λ, as discussed in Sec. IV B. The expansion orders are generally constrained by Eq. (4.23). We find that increasing the expansion orders beyond 4 does not have a visible effect on the simulation results. Thus, the expansion orders are computed using

$$\mathcal{N}_\lambda = \min(Q_\lambda - 1, 4), \qquad \mathcal{N}_\xi = \min(Q_\xi - 1, 4). \quad (6.26)$$

The system at initial time is considered to be in thermal equilibrium ($f' = f'^{(\mathrm{eq})}$ and $f'' = f''^{(\mathrm{eq})}$) corresponding to the temperature T_0, density n_0 and velocity $\boldsymbol{u} = 0$ (the fluid is at rest). The non-dimensionalization convention used for the numerical simulations is such that $H/2 = 1$, $T_0 = 1$ and $n_0 = 1$, while $\sqrt{K_B T_0/m} = 1$ is the reference speed.

C. Boundary conditions

This Subsection presents our strategy for the implementation of the inlet and outlet boundary conditions compatible with the approach used in Refs. [100, 101], as well as of the boundary conditions at the wall and channel center.

1. Inlet boundary conditions

The problem initially proposed in Ref. [101] was the simulation of the incompressible Navier-Stokes flow
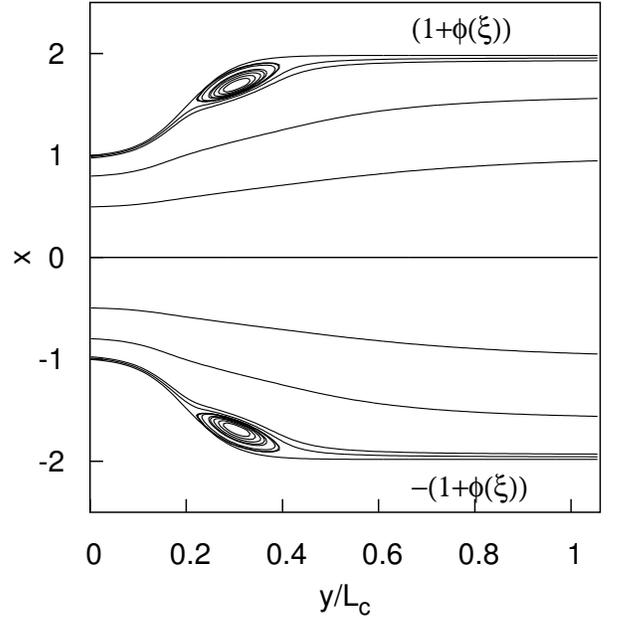
FIG. 22. Streamlines for the flow through the gradually expanding channel corresponding to $\mathrm{Re}_c = 100$, obtained for $Q_0 = 0.1$ and $\mathrm{Kn} = 0.001$ ($\mathrm{Re} = 100$), corresponding to the incompressible hydrodynamic limit.

through the gradually expanding channel introduced in Subsec. VI B, subject to an inlet parabolic velocity profile at $\xi = 0$ of the following form:

$$u^y = \frac{3u_0}{2}\left(1 - \frac{4x^2}{H^2}\right), \qquad u^x = 0, \quad (6.27)$$

such that the particle flow rate through half of the channel cross section is $Q_0 = \frac{H}{2}n_0 u_0$, where n_0 is the fluid particle number density throughout the channel. Equation (6.27) uses the property that $\phi(\xi = 0) = 0$. The Reynolds number is then obtained as follows:

$$\mathrm{Re} = \frac{mQ_0}{\mu} = \frac{u_0}{\mathrm{Kn}}, \quad (6.28)$$

where $H = 2$, $n_0 = 1$ and $u_0 = Q_0$ under the non-dimensionalization employed in this Section, while the viscosity $\mu = \tau n T = \mathrm{Kn}$ by virtue of Eq. (6.23). As mentioned in Ref. [101], this inlet boundary condition immediately raised the concern that at $\xi = 0$, the channel already began its expansion, such that the inlet condition $u^x = 0$ is not realistic.

Even though the results presented in Ref. [101] used Eq. (6.27) as the inlet boundary condition, we instead impose the parabolic profile upstream from $\xi = 0$, at a value ξ_{in} where $\phi'(\xi_{\mathrm{in}}) \simeq 0$. Thus, Eq. (6.27) can be replaced by:

$$
\begin{aligned}
Q_{\mathrm{flow}}^{\mathrm{in}}(\lambda) &= \frac{3Q_0}{H[1 + \phi(\xi_{\mathrm{in}})]}\left\{1 - \frac{4x^2}{H^2[1 + \phi(\xi_{\mathrm{in}})]^2}\right\} \\
&= \frac{3Q_0}{H[1 + \phi(\xi_{\mathrm{in}})]}\left(1 - \frac{4\lambda^2}{H^2}\right), \quad (6.29)
\end{aligned}
$$

where the inlet particle flow rate $Q_{\text{flow}}^{\text{in}}(\lambda)$ at a given value of λ is computed as follows:

$$Q_{\text{flow}}^{\text{in}}(\lambda) = \int dp^{\hat{\xi}} dp^{\hat{\lambda}} f' \frac{p^y}{m}. \qquad (6.30)$$

After the discretization of the spatial domain and of the momentum space, the above expression can be computed using the numerical flux $\mathcal{F}_{\widetilde{\xi};s,1/2;i,j}$ corresponding to $\boldsymbol{p}_{i,j} = (p_i^{\hat{\lambda}}, p_j^{\hat{\xi}})$, as follows:

$$Q_{\text{flow};s}^{\text{in}} \equiv Q_{\text{flow}}^{\text{in}}(\lambda_s) = \sum_{i,j} \frac{p_{s,1/2;i,j}^y}{m} \mathcal{F}_{\widetilde{\xi};s,1/2;i,j}, \qquad (6.31)$$

where the labels of p^y (6.14b) indicate its explicit coordinate and momentum space dependence:

$$p_{s,1/2;i,j}^y = \frac{p_j^{\hat{\xi}} - \lambda_s \phi'(\xi_{1/2}) p_i^{\hat{\lambda}}}{\sqrt{1 + \lambda_s^2 \phi'^2(\xi_{1/2})}}. \qquad (6.32)$$

As also remarked in Ref. [128], the inlet and outlet boundary conditions can be imposed only at the level of the distribution functions corresponding to velocities which travel downstream from the inlet towards the fluid domain (i.e., $p^y > 0$). Thus, our strategy for imposing Eq. (6.29) is the following. The distributions corresponding to particles travelling upstream ($p^y < 0$) are extrapolated at zeroth order from the first fluid node:

$$f'_{s,-1;i,j} = f'_{s,0;i,j} = f'_{s,1;i,j}, \qquad p_{s,1/2;i,j}^y < 0, \quad (6.33)$$

A similar boundary condition is imposed for $f''_{s,p;i,j}$.

The flux for $p_{s,1/2;i,j}^y < 0$ can be computed by noting that $\sigma_3 = 0$ by virtue of Eq. (3.16), such that:

$$\mathcal{F}_{\widetilde{\xi};s,1/2;i,j} = f'_{s,1/2;i,j}, \qquad (p_{s,1/2;i,j}^y < 0). \qquad (6.34)$$

The distribution functions for the particles travelling downstream ($p_{s,1/2;i,j}^y > 0$) are set using:

$$\begin{aligned}
f'_{s,-2;i,j} &= f'_{s,-1;i,j} = f'_{s,0;i,j} = f'_{(\text{eq});\text{in};i,j}, \\
f''_{s,-2;i,j} &= f''_{s,-1;i,j} = f''_{s,0;i,j} = T_0 f'_{(\text{eq});\text{in};i,j},
\end{aligned} \qquad (6.35)$$

where $f'_{(\text{eq});\text{in};i,j} \equiv f'_{(\text{eq});i,j}(n_s^{\text{in}}, \boldsymbol{u}_s^{\text{in}}, T_0)$ is the reduced Maxwell-Boltzmann distribution (4.21), T_0 is the initial temperature and $(u_s^x, u_s^y) = (0, Q_{\text{flow};s}^{\text{in}})$. Since in this case $\sigma_1 = 0$ by virtue of Eq. (3.16), the flux is given by:

$$\mathcal{F}_{\widetilde{\xi};s,1/2;i,j} = f'_{(\text{eq});\text{in};i,j}, \qquad (p_{s,1/2;i,j}^y > 0). \qquad (6.36)$$

The density n_s^{in} is then obtained by imposing Eq. (6.31):

$$n_s^{\text{in}} = \frac{Q_{\text{flow};s}^{\text{in}} - \frac{1}{m} \sum\limits_{p_{s,1/2;i,j}^y < 0} f'_{1,p;i,j} p_{s,\frac{1}{2};i,j}^y}{\frac{1}{m} \sum\limits_{p_{s,1/2;i,j}^y > 0} f'_{(\text{eq});i,j}(1, \boldsymbol{u}_s^{\text{in}}, T_0) p_{s,\frac{1}{2};i,j}^y}. \qquad (6.37)$$

Setting the inlet boundary conditions as explained above achieves the desired parabolic velocity profile shortly after the simulation is started.

2. Outlet boundary conditions

In order to prevent the build-up of particles inside the flow domain, a similar parabolic profile is imposed at the domain outlet (where $\xi = \xi_{\text{out}}$). The value of ξ_{out} is again chosen sufficiently far downstream such that $\phi'(\xi_{\text{out}}) \simeq 0$. In this case, the equivalent of Eq. (6.29) becomes

$$Q_{\text{flow}}^{\text{out}}(\lambda) = \frac{3Q_0}{H[1 + \phi(\xi_{\text{out}})]} \left(1 - \frac{4\lambda^2}{H^2}\right). \qquad (6.38)$$

The construction of the outlet boundary conditions is analogous to the procedure described for the inlet.

3. Specular reflection boundary conditions

Taking advantage of the symmetry of the channel, the simulation domain can be restricted to its upper half when specular boundary conditions are imposed at the centerline. This amounts to populating the nodes with $s \in \{0, -1, -2\}$ as follows:

$$\begin{aligned}
f'_{0,p;i,j} &= f'_{1,p;\overline{\imath},j}, \\
f'_{-1,p;i,j} &= f'_{2,p;\overline{\imath},j}, \\
f'_{-2,p;i,j} &= f'_{3,p;\overline{\imath},j},
\end{aligned} \qquad (6.39)$$

and similarly for $f''_{s,p;i,j}$, where the notation $\overline{\imath}$ refers to the index corresponding to the momentum component $p_i^{\hat{\lambda}}$ which satisfies:

$$p_{\overline{\imath}}^{\hat{\lambda}} = -p_i^{\hat{\lambda}}. \qquad (6.40)$$

4. Diffuse reflection boundary conditions

Diffuse reflection boundary conditions are implemented on the top boundary. Since the vielbein is constructed such that the $p_i^{\hat{\lambda}}$ component of the momentum is always perpendicular to the top wall, the procedure described in Sec. III F applies unchanged to this case. In particular, the values of the distributions in the ghost nodes are populated for the particles travelling back towards the fluid domain ($p_i^{\hat{\lambda}} < 0$) following Eq. (3.30):

$$\begin{aligned}
f'_{N_\lambda+1,p;i,j} &= f'_{N_\lambda+2,p;i,j} = f'_{N_\lambda+3,p;i,j} \\
&= f'_{(\text{eq});\text{i},\text{j}}(n_{\text{w};p}, \boldsymbol{u}_{\text{w}} = 0, T_{\text{w}} = T_0), \quad (6.41)
\end{aligned}$$

while for the particles travelling towards the boundary, the second-order extrapolation given in Eq. (3.32) is employed. Since the wall is at rest, we have $\boldsymbol{u}_{\text{w}} = 0$, while the temperature $T_0 = 1$ is that of the initial state. The wall density $n_{\text{w};p}$ is obtained using Eq. (3.34), as follows:

$$n_{\text{w};p} = -\frac{\sum_{p_i^{\hat{\lambda}}>0} \sum_j V_{N_\lambda+1/2,p;i,j}^\lambda \mathcal{F}_{\widetilde{\lambda};N_\lambda+1/2,p;i,j}}{\sum_{p_i^{\hat{\lambda}}<0} \sum_j f'_{(\text{eq})}(n=1,0,T_0) V_{N_\lambda+1/2,p;i,j}^\lambda}, \qquad (6.42)$$

where $\mathcal{F}_{\widetilde{\lambda};N_\lambda+1/2,p;i}$ is the flux along the λ direction corresponding to the velocity $V_{N_\lambda+1/2,p;i,j}^\lambda$ (6.18).
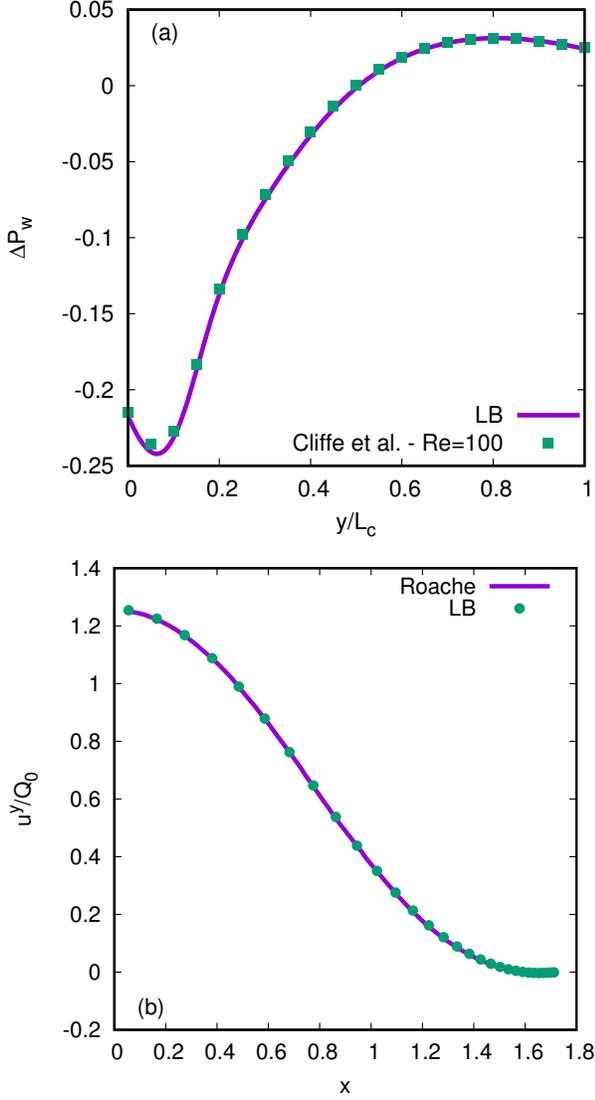
FIG. 23. Simulation results for the flow through the gradually expanding channel with $\mathrm{Re}_c = 100$, $Q_0 = 0.1$ and $\mathrm{Kn} = 0.001$. (a) Normalized wall pressure ΔP_w (6.49) with respect to the normalized coordinate $y/L_c = 3y/\mathrm{Re}_c$ along the channel, validated against the results reported by Cliffe [129]. (b) Normalized streamwise velocity u^y/Q_0 at $\xi = 100/12 \simeq 8.33$, validated against the results reported by Roache [100].

D. Hydrodynamic regime: validation

In this Section, our implementation is validated against results obtained in the incompressible limit of the Navier-Stokes equations, in the case when $\mathrm{Re} = \mathrm{Re}_c = 100$. In order to achieve the incompressible Navier-Stokes regime, we set $u_0 = Q_0 = 0.1$ and $\mathrm{Kn} = 10^{-3}$, which corresponds to $\mathrm{Re} = 100$ according to Eq. (6.28). The results reported in this section are obtained using the $\mathrm{H}(2;3) \times \mathrm{H}(2;3)$ model, employing $3 \times 3 = 9$ velocities.

In the incompressible (low Ma) regime, the continuity equation reduces to $\nabla \cdot \boldsymbol{u} = 0$, which allows the fluid

velocity in planar flows to be determined from the vector potential $\boldsymbol{\Psi}_{\mathrm{inc}} = \boldsymbol{k}\psi_{\mathrm{inc}}$ through $\boldsymbol{u} = \nabla \times \boldsymbol{\Psi}_{\mathrm{inc}}$, such that $u_x = \partial_y \psi_{\mathrm{inc}}$ and $u_y = -\partial_x \psi_{\mathrm{inc}}$ [122]. However, $\nabla \cdot \boldsymbol{u} = 0$ holds only approximately in gas flows. In the kinetic theory approach, the fluid always presents some degree of compressibility. Thus, the correct stream function is computed by noting that in the stationary limit, the continuity equation entails:

$$\nabla \cdot (\rho \boldsymbol{u}) = 0. \tag{6.43}$$

The above equation allows the product $\rho \boldsymbol{u}$ to be written as the curl of the vector potential $\boldsymbol{\Psi} = \boldsymbol{k}\psi$:

$$\rho \boldsymbol{u} = \nabla \times \boldsymbol{\Psi}, \tag{6.44}$$

such that [122]:

$$\rho u_x = \partial_y \psi, \qquad \rho u_y = -\partial_x \psi. \tag{6.45}$$

The stream function ψ can be constructed starting from $\rho u_y = -\partial_x \psi$. Setting $\psi = 0$ on the channel centerline ($s = 1/2$), ψ can be integrated along each line of constant ξ as follows:

$$\psi_{s+1/2,p} = \psi_{s-1/2,p} - \rho_{s,p} u_{s,p}^y (\lambda_{s+1/2,p} - \lambda_{s-1/2,p}), \tag{6.46}$$

where the Cartesian components u^x and u^y are obtained from the vielbein components $u^{\hat{\lambda}}$ and $u^{\hat{\xi}}$ using:

$$u^x = \frac{u^{\hat{\lambda}} + \lambda \phi'(\xi) u^{\hat{\xi}}}{\sqrt{1 + \lambda^2 \phi'^2(\xi)}}, \qquad u^y = \frac{u^{\hat{\xi}} - \lambda \phi'(\xi) u^{\hat{\lambda}}}{\sqrt{1 + \lambda^2 \phi'^2(\xi)}}. \tag{6.47}$$

The streamlines corresponding to the gradually expanding channel with $\mathrm{Re}_c = 100$ obtained from a simulation performed with the $\mathrm{H}(2;3) \times \mathrm{H}(2;3)$ model (employing 9 velocities) are shown in Fig. 22 and a good agreement can be seen with the results obtained using the D2Q9 LB model in Ref. [46]. The inlet and outlet boundary conditions were imposed at $\xi_{\mathrm{in}} = -10$ and $\xi_{\mathrm{out}} = 40$, respectively, and $N_\lambda \times N_\xi = 30 \times 200$ nodes were employed.

We first consider the validation of our numerical results by considering the pressure on the channel wall $P_{\mathrm{w};p} \equiv P_{N_\lambda+1/2;p}$, which is obtained via linear extrapolation along the λ direction from the inner nodes:

$$P_{\mathrm{w};p} = \frac{(x_{\mathrm{w}} - x_{N_\lambda-1})P_{N_\lambda,p} - (x_{\mathrm{w}} - x_{N_\lambda})P_{N_\lambda-1,p}}{x_{N_\lambda} - x_{N_\lambda-1}}, \tag{6.48}$$

where $x_w \equiv x_{N_\lambda+1/2}$ is the wall coordinate. The value $P_{\mathrm{w};c}$ of the wall pressure at the center of the channel (where $\xi = \mathrm{Re}_c/6 \simeq 16.67$) is further subtracted from $P_{\mathrm{w};p}$ and the result is divided by $\rho_0 u_0^2$ in order to conform with the non-dimensionalization conventions employed in Ref. [129]:

$$\Delta P_{\mathrm{w};p} = \frac{P_{\mathrm{w};p} - P_{\mathrm{w};c}}{\rho_0 u_0^2}. \tag{6.49}$$
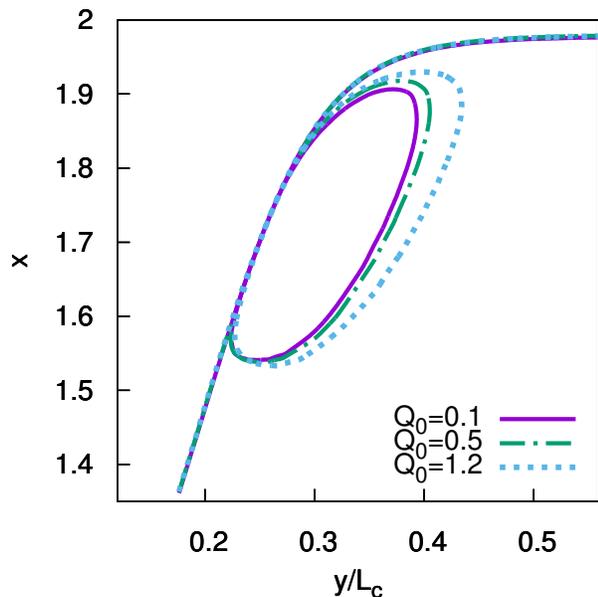
FIG. 24. Streamlines for the flow through the gradually expanding channel corresponding to $\mathrm{Re}_c = 100$, obtained for $(Q_0, \mathrm{Kn}) \in \{(0.1, 0.001); (0.5, 0.005); (1.2, 0.012)\}$, such that $\mathrm{Re} = 100$, highlighting the outermost contour of the vortex. Only the region around the vortex in the upper half of the channel is represented.

Kn	Model	N_{vel}	δt
0.001	$\mathrm{H}(2;3) \times \mathrm{H}(2;3)$	9	10^{-3}
0.002	$\mathrm{H}(4;5) \times \mathrm{H}(4;5)$	25	10^{-3}
0.005	$\mathrm{HH}(3;4) \times \mathrm{H}(4;5)$	40	2×10^{-3}
0.01	$\mathrm{HH}(3;4) \times \mathrm{H}(4;5)$	40	2×10^{-3}
0.05	$\mathrm{HH}(4;8) \times \mathrm{H}(4;5)$	80	10^{-3}
0.1	$\mathrm{HH}(4;12) \times \mathrm{H}(4;5)$	120	10^{-3}
0.2	$\mathrm{HH}(4;20) \times \mathrm{H}(4;5)$	200	5×10^{-4}
0.5	$\mathrm{HH}(4;40) \times \mathrm{H}(4;5)$	400	5×10^{-4}

TABLE IV. Mixed quadrature LB models, total number of velocities N_{vel} and time step δt employed for the study of rarefaction effects in the expanding channel in Subsec. VI F. The inlet half-channel mass flow rate is kept at $Q_0 = 0.1$.

It can be seen in Fig. 23(a) that our numerical results for $\Delta P_{\mathrm{w};p}$ are in very good agreement with the benchmark data reported by Cliffe [129].

Figure 23(b) validates our results for the normalized downstream velocity u^y/Q_0 (6.47) at $\xi = \mathrm{Re}_c/12 \simeq 8.33$, by comparing with the results reported by Roache [100]. An excellent agreement can be seen.

E. Compressibility effects

In order to probe the compressible, variable temperature regime of the Navier-Stokes equations, we consider three values for the inlet particle flow rate, namely $Q_0 = 0.1, 0.5, 1$ and 1.2. The value of the Reynolds number is kept at $\mathrm{Re} = 100$, such that the Knudsen number Kn is increased, taking the values $0.001, 0.005, 0.01$ and 0.012 by virtue of Eq. (6.28). The simulation corresponding to $\mathrm{Kn} = 0.001$ was performed using the $\mathrm{H}(2;3) \times \mathrm{H}(2;3)$ model, while for $\mathrm{Kn} = 0.005, 0.01$ and 0.012, the $\mathrm{HH}(3;4) \times \mathrm{H}(4;5)$ model was employed.

Using Eq. (6.46) to compute the stream function ψ, its isocontours of the stream function ψ corresponding to the outermost closed loops of the vortices corresponding to $Q_0 = 0.1, 0.5$ and 1.2 are represented in Fig. 24 with purple, green and cyan, respectively. It can be seen that as Q_0 is increased, the vortex is enlarged.

The profile of the normalized local particle flow rate $Q(x)/Q_0$ at $\xi = \mathrm{Re}_c/12$ is shown in Fig. 25(a). It can be seen that, for the values of Kn considered in this Subsec-

tion, $Q(x)/Q_0$ is independent of Kn and Q_0, as long as $\mathrm{Re} = 100$ is kept constant. Thus, the flow remains in the hydrodynamic regime even for $\mathrm{Kn} = 0.012$. The temperature profile shown in Fig. 25(b) has a non-monotonic behaviour with respect to x, exhibiting a point of maximum around $x \simeq x_{\mathrm{top}}/2$, where $x_{\mathrm{top}} \simeq 1.718$. Finally, the normalized pressure difference ΔP_{w} is shown in Fig. 25(c). It can be seen that ΔP_{w} increases at the onset of the expansion (around $\xi = 0$), as well as towards the outlet.

F. Rarefaction effects

In this Subsection, the capabilities of our models to capture non-equilibrium flows are highlighted by performing simulations at fixed mass flow rate $Q_0 = 0.1$ for various values of the Knudsen number, taken between $0.001 \leq \mathrm{Kn} \leq 0.5$. The models employed in order to conduct these simulations are summarized in Table IV. The aim of this Subsection is to highlight the transition from the hydrodynamic to the rarefied regime as the Knudsen layer develops at the diffuse reflective boundary. Even though Re decreases as Kn is increased according to Eq. (6.28), the simulations are performed in the channel corresponding to $\mathrm{Re}_c = 100$.

We begin this Section with a discussion of the pressure. In the limit when the inlet and outlet are positioned sufficiently far away, the flow configuration is comprised of two pressure-driven Poiseuille flow regions separated by the expanding portion between them.

Around the expanding portion and for $\mathrm{Kn} \lesssim 0.01$, the pressure profile exhibits a non-monotonic behaviour, as shown in Fig. 26(a). This kind of behaviour was also observed in simulations of the micro-orifice flow performed using the Direct Simulation Monte Carlo (DSMC) and the Gas-Kinetic Unified Algorithm (GKUA) in Refs. [134] and [135], respectively. As Kn is increased, the effect of the expanding portion becomes negligible and the pressure profiles decrease monotonically with ξ, as shown in Fig. 26(b).

Far from the expanding region, the pressure decreases
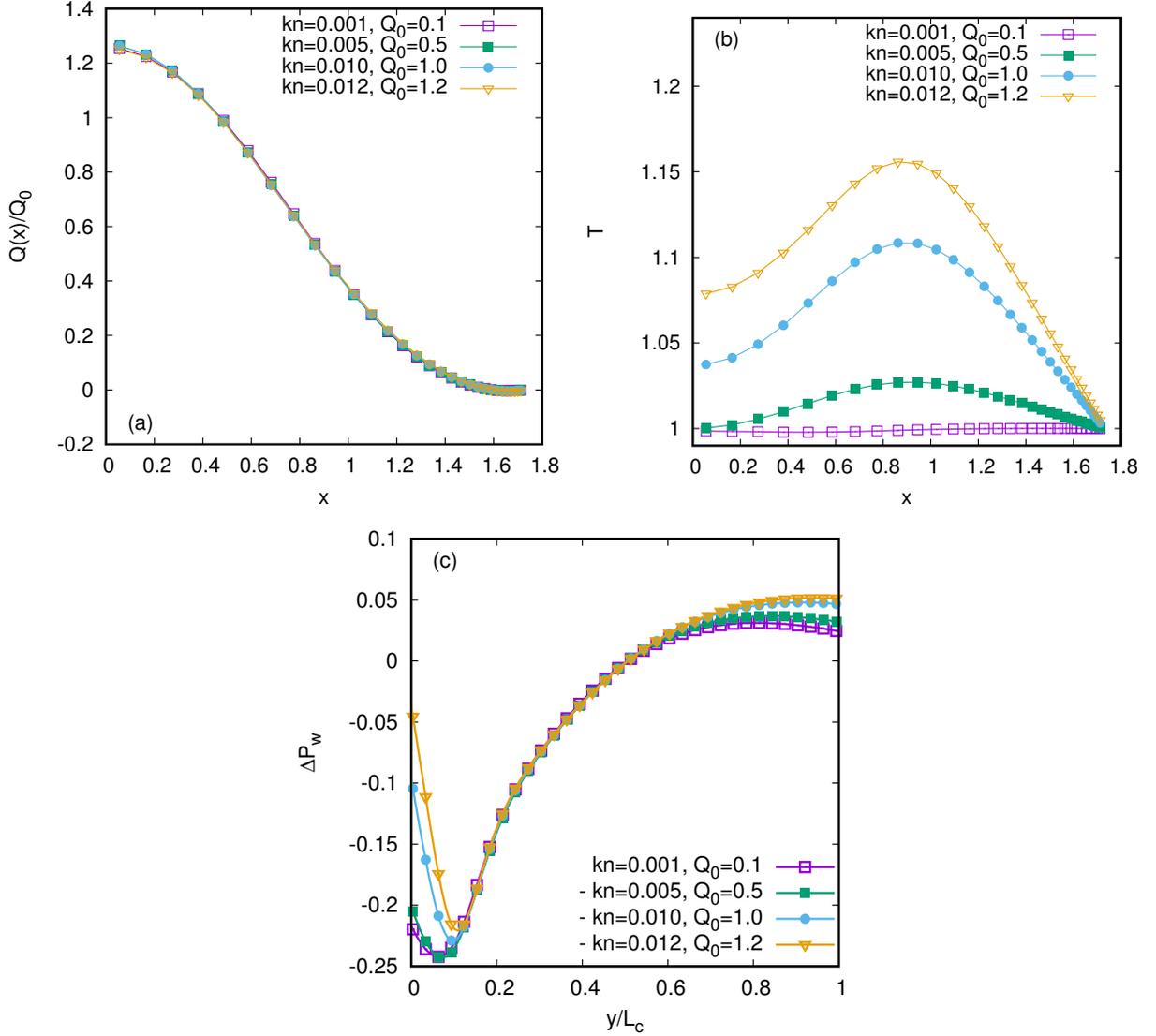
FIG. 25. Numerical results for the gradually expanding channel flow for (a) normalized local particle flow rate $Q(x)/Q_0$ and (b) temperature T across the channel at $\xi = \mathrm{Re}_c/12$, as well as (c) the normalized wall pressure difference ΔP_w (6.49) against the normalized streamwise coordinate $y/L_c = 3y/\mathrm{Re}_c$, at various values of Kn. The particle flow rate is varied according to $Q_0 = 100\,\mathrm{Kn}$ in order to maintain Re = 100 for all simulations.

linearly with respect to the streamwise coordinate y. In the hydrodynamic regime, the pressure gradient is given by [123]:

$$\frac{dP}{dy} = -\frac{12\mu Q_\mathrm{tot}}{n\ell^3} = -\frac{3Q_0}{(1+\phi)^3}\mathrm{Kn}, \qquad (6.50)$$

where $Q_\mathrm{tot} = 2Q_0$ is the particle flow rate through the full channel width $\ell = H(1+\phi)$, while $\phi(y \ll 0) \simeq -0.018$ and $\phi(y \gg 0) \simeq 0.982$ in the upstream and downstream regions from the expanding portion. Outside the hydrodynamic regime, the relation between the pressure gradient and the Knudsen number is more complicated. In-

troducing the notation:

$$\frac{dP}{dy} = -\frac{mQ_\mathrm{tot}v_0}{\ell^2 G_\mathrm{P}^*} = -\frac{Q_0}{\sqrt{2}(1+\phi)^2 G_\mathrm{P}^*}, \qquad (6.51)$$

where $v_0 = \sqrt{2K_B T_0/m} = \sqrt{2}$ is the most probable speed and $\ell = H(1+\phi) = 2(1+\phi)$ is the channel width, the dependence of the pressure gradient on the Knudsen number is contained in the Poiseuille coefficient G_P^* [11]. In the linearized limit of the slip regime, G_P^* can be written as:

$$G_\mathrm{P}^* = \frac{\delta}{6} + \sigma_\mathrm{P}, \qquad (6.52)$$

where the rarefaction parameter δ depends on the local
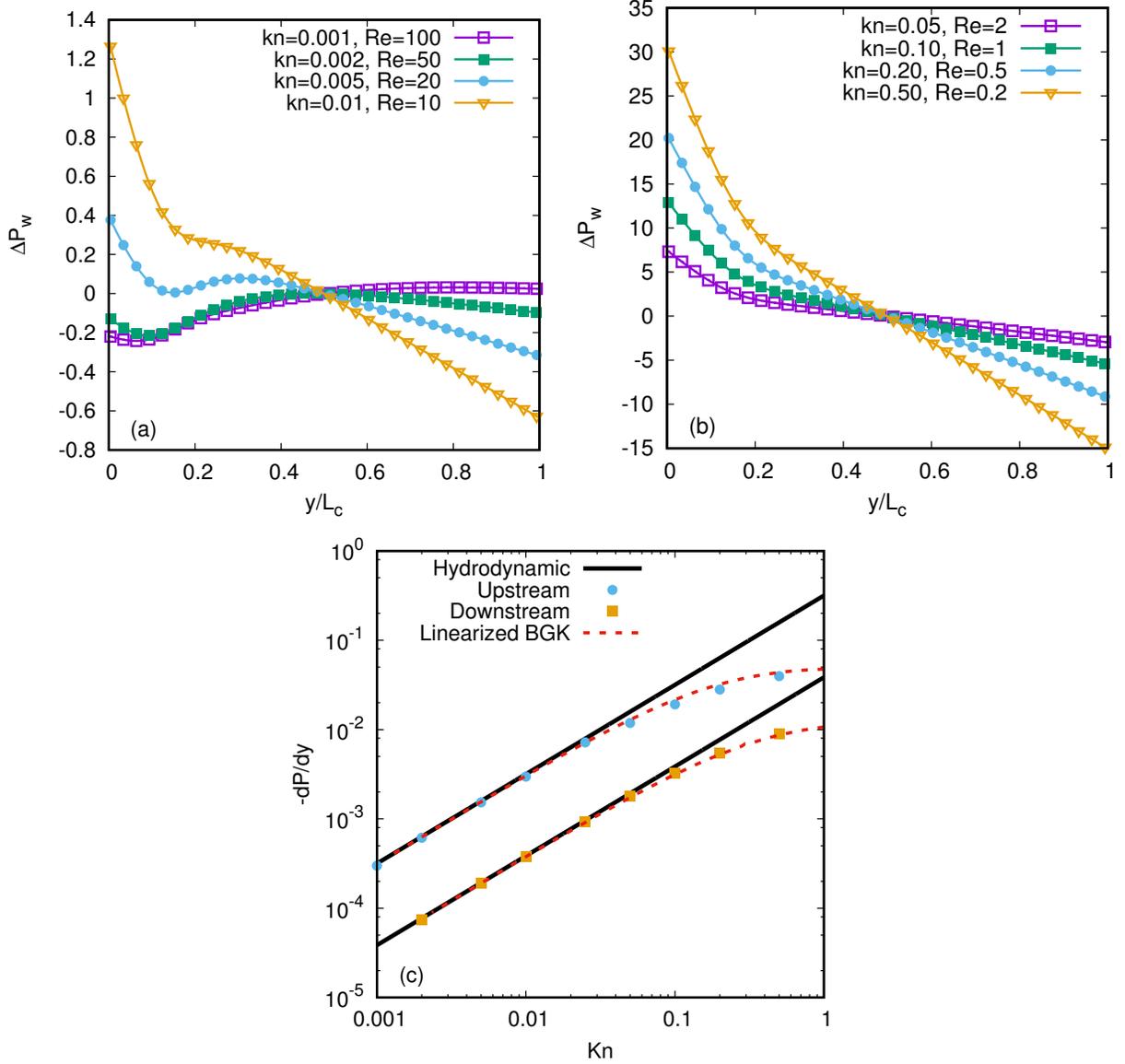
FIG. 26. Gradually expanding channel flow results for $\Delta P_{\rm w}$ (6.49) in the hydrodynamic (a) and slip flow (b) regimes with respect to the normalized downstream coordinate $y/L_c = 3y/\mathrm{Re}_c$, as well as for $-dP/dy$ in the upstream ($y/L_c < 0$) and downstream ($y/L_c > 0.5$) regions. The hydrodynamic limit curves $-dP/dy \simeq 0.317\,\mathrm{Kn}$ (upstream, $\phi \simeq -0.018$) and $-dP/dy \simeq 0.0385\,\mathrm{Kn}$ (downstream, $\phi \simeq 0.982$) are obtained from Eq. (6.50). The linearized Boltzmann-BGK results for the pressure-driven Poiseuille flow are represented with red dotted lines and are computed using Eq. (6.51) using the values for $G_{\rm P}^*$ reported in Refs. [131, 133]. The half-channel particle flow rate is taken as $Q_0 = 0.1$.

channel width and Knudsen number Kn through:

$$\delta = \frac{\ell}{\mathrm{Kn}\sqrt{2}} = \frac{\sqrt{2}}{\mathrm{Kn}}[1 + \phi(y)]. \qquad (6.53)$$

The value of $\sigma_{\rm P}$ in Eq. (6.52) depends on the particle-wall interaction, having the value $\sigma_{\rm P} \simeq 1.0162$ for diffuse reflection [11, 130–132]. In the transition and free molecular flow regimes, the values of $G_{\rm P}^*$ can be computed numerically or semianalytically and are tabulated in a variety of papers, of which we recall [11, 131–133], where the linearized limit of the Boltzmann-BGK equation is

considered. The values of $-dP/dy$ obtained from our numerical results far upstream and far downstream from the expanding portion are compared with the hydrodynamic limit (6.50) and the general formula (6.51) in Fig. 26(c), where the values of $G_{\rm P}^*$ correspond to the linearized limit of the pressure-driven Poiseuille flow and are taken from Refs. [131, 133]. It can be seen that the increase of the absolute value of the pressure gradient $-dP/dy$ is linear in Kn for Kn $\lesssim 0.05$, while for Kn $\gtrsim 0.05$, $-dP/dy$ increases at a much slower rate, in good agreement with the behaviour predicted in Refs. [11, 131–133]. This is
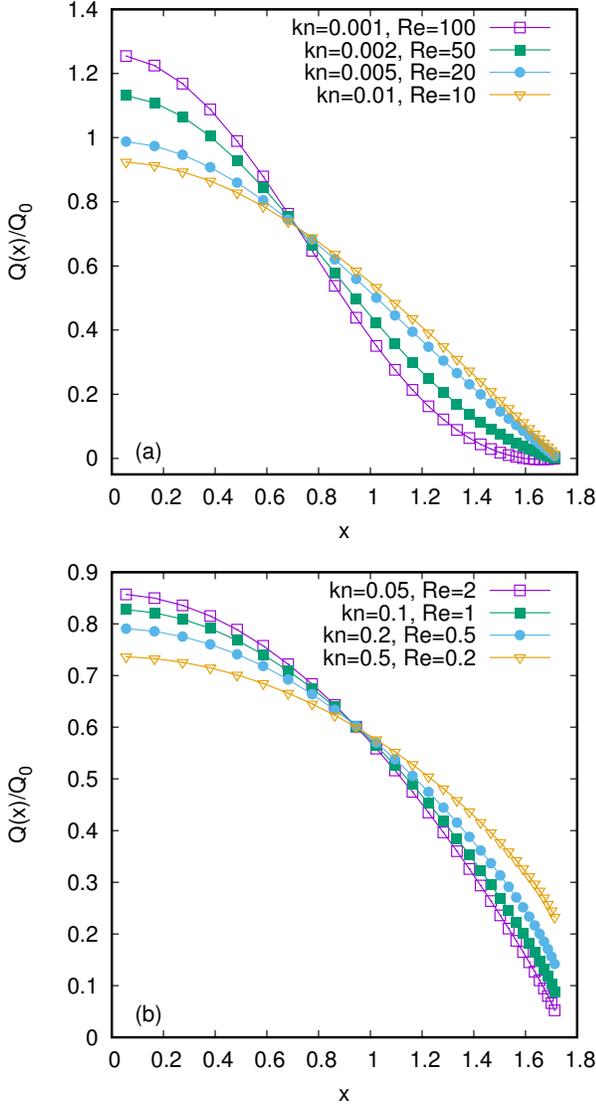
FIG. 27. Numerical results for the normalized local particle flow rate $Q(x)/Q_0$ across the channel at $\xi \simeq 8.33$ in the hydrodynamic (a) and slip flow (b) regimes for the gradually expanding channel flow corresponding to $\mathrm{Re}_c = 100$ in Eq. (6.24). The half-channel particle flow rate is taken as $Q_0 = 0.1$ for various values of Kn, such that the resulting Reynolds number decreases as Kn is increased.

FIG. 28. Numerical results for the normalized vorticity $-\omega/Q_0$ as a function of (a) x; and (b) d (6.58), taken at $y = \mathrm{Re}_c/16 \simeq 8.33$, where $\mathrm{Re}_c = 100$ defines the channel geometry through Eq. (6.24). The half-channel particle flow rate is taken as $Q_0 = 0.1$ for various values of Kn, such that the resulting Reynolds number of the flow decreases as Kn is increased.

the first indication that at $\mathrm{Kn} \gtrsim 0.05$, the rarefaction effects become important.

The normalized local particle flow rate profile at $y = \mathrm{Re}_c/12$ is shown in Fig. 27 for various values of Kn. The presence of the vortex in the $\mathrm{Kn} = 0.001$ simulation (corresponding to $\mathrm{Re} = 100$ for the flow) is highlighted by the negative values attained by u^y close to the boundary. For $\mathrm{Kn} \gtrsim 0.002$, Re is significantly decreased, the vortex no longer forms and u^y decreases monotonically from the channel centerline towards the boundary. In the hydrodynamic flow regime shown in Fig. 27(a) ($\mathrm{Kn} \lesssim 0.01$), the particle flow rate regains a parabolic profile as Kn

is increased, while the velocity slip at the wall remains negligible. Figure 27(b) shows that the slip velocity becomes non-negligible as $\mathrm{Kn} \gtrsim 0.05$, when the rarefaction effects become important, as also noted in the previous paragraph regarding the pressure profile.

The previous discussion of the particle flow rate profile clearly highlights the development of the Knudsen layer as Kn is increased above ~ 0.05. In order to better assess the capability of our models to capture the physics of the Knudsen layer, we note that the velocity receives contributions of the form $d \ln d$ inside the Knudsen layer,

where d measures the distance from the wall [17, 136–139]. While this term is difficult to highlight when discussing the velocity profile, it becomes dominant in the profile of the vorticity $\omega = \partial_x u_y - \partial_y u_x$, which can be written as:

$$\omega = -\frac{\partial u^x}{\partial \xi} + \frac{1}{1 + \phi(\xi)}\left[\frac{\partial u^y}{\partial \lambda} + \lambda \phi'(\xi)\frac{\partial u^x}{\partial \lambda}\right]. \quad (6.54)$$

The derivatives with respect to ξ are computed using centered differences and the second order forward or backward Euler scheme at the inlet and outlet nodes, respectively. For the derivatives with the non-equidistantly distributed λ coordinate, we used the following scheme for bulk nodes ($1 < s < N_\lambda$):

$$\left(\frac{\partial f}{\partial \lambda}\right)_{s,p} = \frac{(\lambda_s - \lambda_{s-1})f_{s+1,p}}{(\lambda_{s+1} - \lambda_s)(\lambda_{s+1} - \lambda_{s-1})}$$
$$+ \frac{(\lambda_{s+1} - 2\lambda_s + \lambda_{s-1})f_{s,p}}{(\lambda_{s+1} - \lambda_s)(\lambda_s - \lambda_{s-1})}$$
$$- \frac{(\lambda_{s+1} - \lambda_s)f_{s-1,p}}{(\lambda_{s+1} - \lambda_{s-1})(\lambda_s - \lambda_{s-1})}. \quad (6.55)$$

In the first node ($s = 1$), the following formula is used:

$$\left(\frac{\partial f}{\partial \lambda}\right)_{1,p} = -\frac{(\lambda_2 + \lambda_3 - 2\lambda_1)f_{1,p}}{(\lambda_2 - \lambda_1)(\lambda_3 - \lambda_1)}$$
$$+ \frac{(\lambda_3 - \lambda_1)f_{2,p}}{(\lambda_2 - \lambda_1)(\lambda_3 - \lambda_2)} - \frac{(\lambda_2 - \lambda_1)f_{3,p}}{(\lambda_3 - \lambda_1)(\lambda_3 - \lambda_2)}. \quad (6.56)$$

The derivative in the last node ($s = N_\lambda$) is computed using:

$$\left(\frac{\partial f}{\partial \lambda}\right)_{N_\lambda,p} = -\frac{(2\lambda_{N_\lambda} - \lambda_{N_\lambda-1} - \lambda_{N_\lambda-2})f_{N_\lambda,p}}{(\lambda_{N_\lambda} - \lambda_{N_\lambda-1})(\lambda_{N_\lambda} - \lambda_{N_\lambda-2})}$$
$$- \frac{(\lambda_{N_\lambda} - \lambda_{N_\lambda-2})f_{N_\lambda-1,p}}{(\lambda_{N_\lambda} - \lambda_{N_\lambda-1})(\lambda_{N_\lambda-1} - \lambda_{N_\lambda-2})}$$
$$+ \frac{(\lambda_{N_\lambda} - \lambda_{N_\lambda-1})f_{N_\lambda-2,p}}{(\lambda_{N_\lambda} - \lambda_{N_\lambda-2})(\lambda_{N_\lambda-1} - \lambda_{N_\lambda-2})}. \quad (6.57)$$

Due to the logarithmic singularity of the gradient of the velocity, the vorticity cannot be defined on the diffuse reflective boundary. The logarithmic divergence of the vorticity is highlighted in Fig. 28 with respect to (a) the distance x from the channel center and (b) the non-dimensionalized distance d to the top wall, defined through:

$$d = 1 + \phi(y) - \frac{2x}{H}. \quad (6.58)$$

At Kn $= 0.002$, no evidence of the Knudsen layer can be seen. This is due to the fact that the point which is closest to the boundary is at a non-dimensionalized distance $d \simeq 0.0055$ from the boundary, while at Kn $= 0.002$, the Knudsen layer is localized closer to the boundary. When Kn $\gtrsim 0.01$, the Knudsen layer becomes visible especially
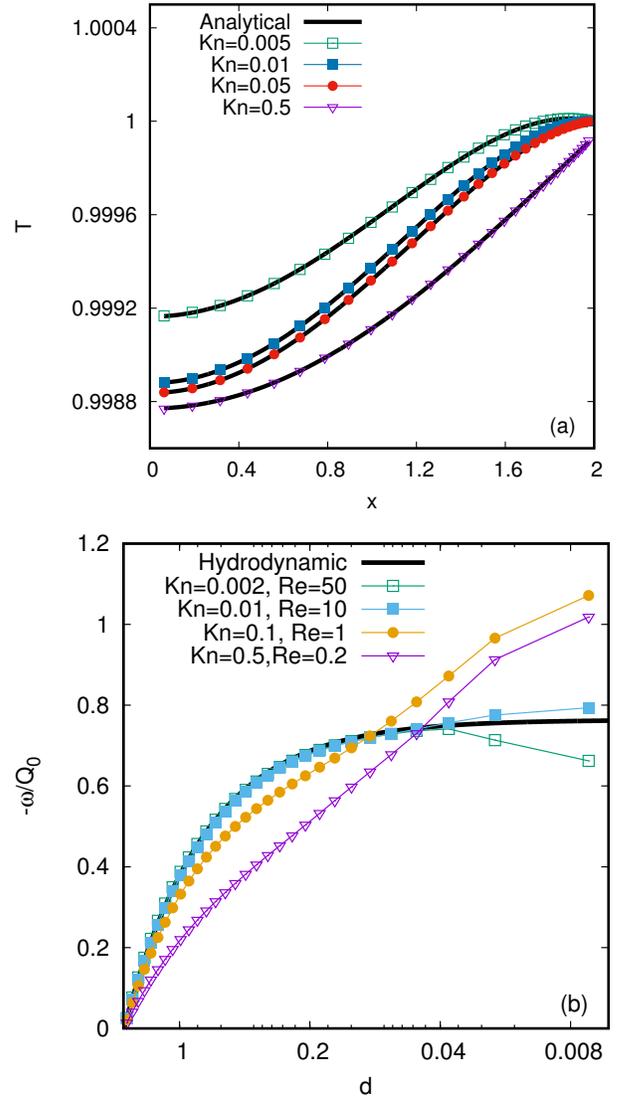
FIG. 29. Numerical results for the temperature T(a) and normalized vorticity $-\omega/Q_0$(b) across the channel at $\xi \simeq 33$ slip flow regime for the gradually expanding channel flow corresponding to $\text{Re}_c = 100$ in Eq. (6.24). The half-channel particle flow rate is taken as $Q_0 = 0.1$ for various values of Kn, such that the resulting Reynolds number decreases as Kn is increased.

in Fig. 28(a), where the rapid increase of $-\omega$ in the vicinity of the wall can be clearly seen. At Kn $= 0.5$, $-\omega$ increases roughly linearly with respect to $-\ln d$, except for the last few nodes, which may be affected by numerical effects caused by our formulation of the diffuse reflection boundary conditions.

We finally consider the analysis of the flow far downstream from the expanding region. At $y = \text{Re}/3$, the flow enters the regime of the Poiseuille flow. At non-negligible values of Kn, the temperature profile for the Poiseuille flow between parallel plates can be written as

[35, 140, 141]:

$$T(x) = T_0 + \alpha x^2 + \beta x^4, \qquad (6.59)$$

where T_0 is the temperature on the centerline. The bimodal profile for the temperature occurs as a rarefaction effect and was shown in Ref. [142] to be accounted for only at super-Burnett level. After fitting T_0, α and β to the numerical data, it can be seen in Fig. 29(a) that the fluid temperature falls below the temperature of the channel wall. This effect was also observed in Refs. [6, 142–144] and is due to fact that the viscous heating is superseded by the gas expansion [143]. In the hydrodynamic regime, the streamwise velocity u^y is approximately given by an expression similar to Eq. (6.27), such that the vorticity becomes:

$$\omega_{\text{Pois}} = -\frac{3u_0 x}{x_{\text{top}}^2}. \qquad (6.60)$$

It can be seen in Fig. 29(b) that the results corresponding to Kn = 0.002 and 0.01 agree very well with the hydrodynamic prediction (6.60), except for the last few nodes which may receive errors from our formulation of the boundary conditions. At Kn $\gtrsim 0.1$, the effects of the Knudsen layer become visible as the magnitude of the vorticity $-\omega$ increases almost linearly with $-\ln d$.

G. Cartesian decomposition of the momentum space

Let us now analyze the case when the momentum space is discretized with respect to its Cartesian degrees of freedom (p^x, p^y). Making the coordinate change from (x, y) to (λ, ξ), the Boltzmann equation becomes:

$$\frac{\partial f}{\partial t} + \frac{p^{\widetilde{\lambda}}}{m}\frac{\partial f}{\partial \lambda} + \frac{p^{\widetilde{\xi}}}{m}\frac{\partial f}{\partial \xi} = -\frac{1}{\tau}[f - f^{(\text{eq})}], \qquad (6.61)$$

where $p^{\widetilde{\lambda}}$ and $p^{\widetilde{\xi}}$ are given in Eq. (6.7). Equation (6.61) can be put in conservative form as follows:

$$\frac{\partial f}{\partial t} + \frac{\partial (V^\lambda f)}{\partial \lambda} + \frac{\partial (V^\xi f)}{\partial \chi^\xi} = -\frac{1}{\tau}[f - f^{(\text{eq})}], \qquad (6.62)$$

where χ^ξ is defined in Eq. (6.19) and

$$V^\lambda = \frac{p^x - \lambda \phi' p^y}{m(1 + \phi)}, \qquad V^\xi = (1 + \phi)\frac{p^y}{m}. \qquad (6.63)$$

The advantage of the Boltzmann equation (6.62) written with respect to the original Cartesian components (p^x, p^y) of the momentum space is that the force terms appearing in the vielbein equivalent (6.17) are absent. Thus, the coefficient a_5 corresponding to the computation of the force term can be set to 0 in the runtime estimate given by Eq. (5.68). However, we anticipate

that this apparent improvement of the runtime is compensated by increased quadrature orders, as will be discussed below.

The drawback when the vielbein formalism is not employed is that the diffuse reflection boundary conditions must be implemented judging by the sign of a linear combination of p^x and p^y. Considering that the momentum space is discretized using Gauss quadratures of orders Q_x and Q_y with respect to p_x and p_y, respectively, the density n_w required to construct the wall populations is computed using:

$$n_w = -\frac{\displaystyle\sum_{V^\lambda_{N_\lambda+1/2,p;i,j} > 0} \mathcal{F}_{\lambda;N_{\lambda+1/2},p;i,j}}{\displaystyle\sum_{V^\lambda_{N_\lambda+1/2,p;i,j} < 0} f'_{(\text{eq})}(n = 1, 0, T_0)V^\lambda_{N_\lambda+1/2,p;i,j}}, \qquad (6.64)$$

where the discretization of the spatial grid is performed as discussed in Subsec. VI A. In the regions where ϕ' is non-negligible, n_w must be computed by integrating over regions of the momentum space which are position-dependent.

We now consider the flow through the gradually expanding channel corresponding to Re$_c$ = 100 in Eq. (6.24). As before, the flow region of interest is between $\xi = 0$ and $\xi = \text{Re}_c/3 \simeq 33.33$. The inlet and outlet are positioned at $\xi_{\text{in}} = -10$ and $\xi_{\text{out}} = 40$, thus giving enough space for the flow to adjust itself before entering the region of interest. For definiteness, we consider $Q_0 = 0.1$ and Kn = 0.2 for the remainder of this Subsection. The channel is discretized using $N_\xi = 200$ equidistant points along the ξ axis and $N_\lambda = 30$ points along the λ direction, which are stretched according to Eq. (6.20) with $A = 0.95$.

It can be expected that the differences between the vielbein-based lattice Boltzmann (VLB) and Cartesian split-based lattice Boltzmann (CLB) implementations will be most significant in the expanding region of the channel. Moreover, we expect that the VLB implementation will be more accurate within the Knudsen layer. In Fig. 30, the normalized wall pressure ΔP_w (6.49) obtained using the VLB and CLB implementations at similar quadrature orders is shown. It can be seen that there are no visible discrepancies at the level of the wall pressure. Next, Fig. 31 shows a comparison of the VLB and CLB results for the normalized flow rate Q/Q_0 and vorticity $-\omega/Q_0$ around the expansion region, along lines of constant λ. In Fig. 31(a), it can be seen that the flow rate results are in general in good agreement, apart from along the line which is closest to the wall ($\lambda = 0.997$), where a small discrepancy can be seen in the expanding region (around $y/L_c \simeq 0.1$). Also in the expanding region, Fig. 31(b) shows that the CLB results for the vorticity profile present oscillations with respect to y/L_c, which become more pronounced as the wall is approached. On the other hand, the VLB results vary smoothly with respect to y/L_c.
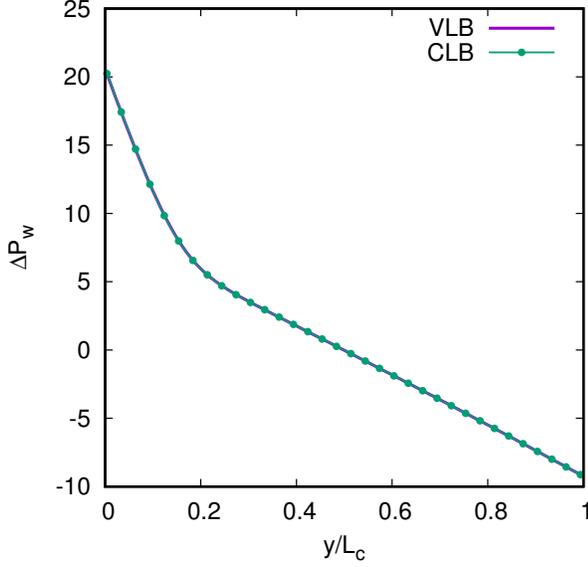
FIG. 30. Comparison of the simulation results for the normalized wall pressure $\Delta P_{\rm w}$ (6.49) obtained using the VLB model HH(4; 6) × H(4; 5) (solid line) and the CLB model HH(4; 6) × HH(4; 6) (line and points). The results are overlapped.

The amplitude of the oscillations observed in the vorticity profile obtained using the CLB approach decrease as the quadrature order increases. Similarly, the results obtained using the VLB approach exhibit a convergence trend as the quadrature order is increased. For the study of the quadrature order dependence of ω, we consider the transverse vorticity profile at fixed values of y/L_c inside the expansion region.

In Fig. 32, the typical convergence trend of the vorticity profile obtained using the VLB implementation is shown at $y/L_c = 0.25$ by varying Q_λ at fixed $Q_\xi = 5$ (a) and by varying Q_ξ at fixed $Q_\lambda = 16$ (b). The half-range and full-range Gauss Hermite quadratures are used on the λ and ξ directions, respectively. From Fig. 32(a), it can be seen that convergence with respect to Q_λ is achieved faster for the nodes closer to the channel center than for the nodes in the vicinity of the wall. Figure 32(b) demonstrates the remarkable property that the VLB results for the vorticity corresponding to a fixed value of Q_λ are overlapped for all values of $Q_\xi \geq 3$. A similar property is also observed in the context of the Couette [34] and Poiseuille [35] flows between parallel plates. It is shared by the VLB implementation because the $p^{\hat{\xi}}$ momentum space direction is always parallel to the wall. We note that $Q_\xi = 3$ is insufficient to capture the temperature profile shown in Fig. 29(a). For small Mach number flows, $Q_\xi = 4$ is in general sufficient to obtain accurate results, even for the temperature profile. When the Mach number is non-negligible (i.e., as considered in Fig. 25), $Q_\xi = 5$ must be used. Our simulations indicate that further increasing the value of Q_ξ does not affect the ac-
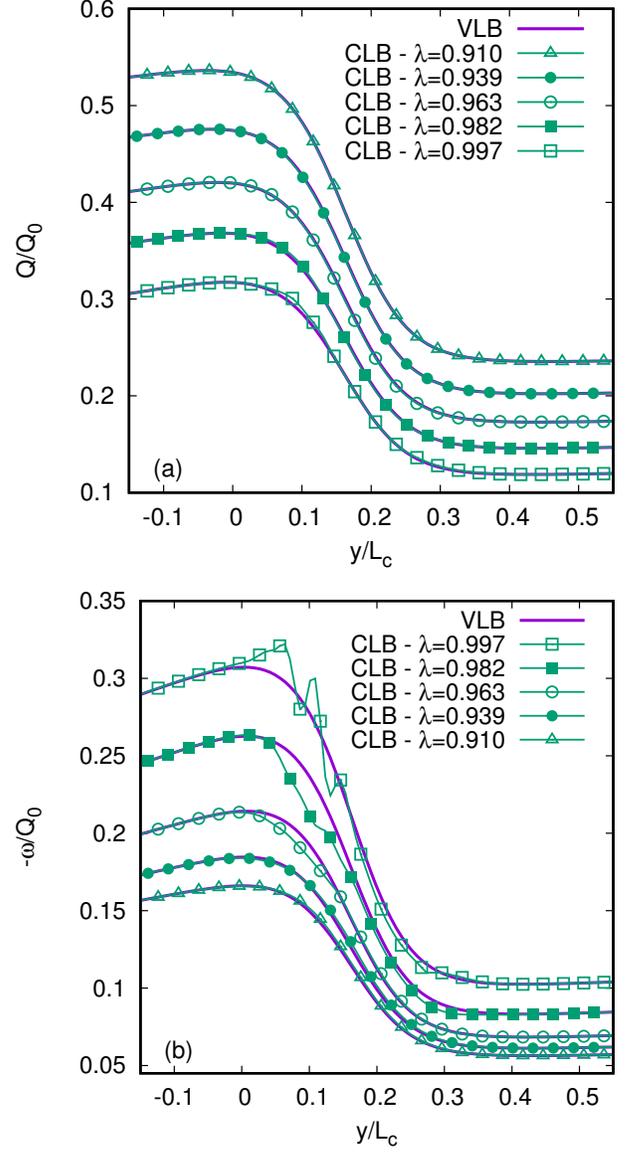
FIG. 31. Comparison of (a) the normalized mass flow rate Q/Q_0 and (b) the normalized vorticity $-\omega/Q_0$ at $\lambda = \{0.997, 0.982, 0.963, 0.939, 0.910\}$ obtained using the VLB model HH(4; 6) × H(4; 5) (solid lines) and the CLB model HH(4; 6) × HH(4; 6) (lines and points).

curacy of the numerical results for all the flow parameters considered in this section.

In order to study the convergence trend of the CLB results, the transverse ω profile is represented in Fig. 33 at selected values of y/L_c. According to Eq. (6.64), the computation of the density n_w of the populations emerging from the wall back into the fluid requires the recovery of integrals over the half of the (p^x, p^y) plane for which $p^x - \lambda\phi'(y)p^y$, such that the integration range does not cover the full $(-\infty, \infty)$ interval on either p^x or p^y. Thus, the momentum space is discretized using the half-range Gauss-Hermite quadrature for both the p^x and the p^y

degrees of freedom. Figure 33(a) shows that increasing $Q_x = Q_y$ simultaneously brings the CLB results towards the VLB results obtained using $Q_\lambda = 20$ and $Q_\xi = 5$, confirming that at high quadrature orders, the VLB and CLB implementations yield similar results. However, Fig. 33(b) shows that the accuracy of the CLB results depends strongly on Q_y. Thus, contrary to the case of the VLB implementation, the accuracy of the CLB results also depends on the value of Q_y. The results in Figs. 33(a) and 33(b) are represented at $y/L_c \simeq 0.041$ and $y/L_c \simeq 0.154$, respectively.

It is worth remarking that the profiles of the pressure P and flow rate Q can be recovered with much smaller quadrature orders compared to the profile of the vorticity ω, even at non-negligible values of Kn. Moreover, Figs. 31(b) and 30 show that the fluctuations in the profiles of Q and P are almost negligible, even when the model $HH(4;6) \times HH(4;6)$ is employed.

We end this section with a comparative analysis of the performance of the CLB and VLB implementations. Since the primary difference of these implementations is in the way the momentum space is discretized, it is reasonable to compare their performance on the same spatial grid, comprised of $N_\lambda \times N_\xi = 30 \times 200 = 6\,000$ nodes. In the VLB implementation, the full-range Gauss-Hermite quadrature of order $Q_\xi = 5$ can be employed along the flow direction, while the half-range Gauss-Hermite quadrature of order $Q_\lambda = Q$ is employed along the direction which is perpendicular to the boundary. In order to ensure the same degree of accuracy between the VLB and CLB implementations, the half-range Gauss-Hermite quadrature must be employed on both axes in the CLB implementation, with quadrature orders equal to the one employed in the VLB implementation, namely $Q_x = Q_y = Q$. The total number of velocities in the VLB implementation is $N_{\text{vel}}^{\text{VLB}} = 10Q$, while in the CLB implementation, $N_{\text{vel}}^{\text{CLB}} = 4Q^2$ velocities are employed. The time ΔT required to perform one iteration can be estimated as in Eq. (5.68) (after minor adjustments to account for a two-dimensional grid). In the case of the VLB implementation, ΔT can be estimated through:

$$\Delta T_{\text{VLB}} = 10a_{\text{v}}Q + 10b_{\text{v}}(2Q + 5)Q + c_{\text{v}}, \qquad (6.65)$$

while in the case of the CLB implementation, the force term is absent ($b_c = 0$):

$$\Delta T_{\text{CLB}} = 4a_c Q^2 + c_c. \qquad (6.66)$$

Formally, the algorithmic complexity of the VLB and CLB implementations is similar. At large values of Q, $\Delta T_{\text{VLB}}/\Delta T_{\text{CLB}} \simeq 5b_v/a_c$, where b_v and a_c are the values of the coefficients b and a corresponding to the VLB and CLB implementations, respectively. In the context of the circular Couette flow, the analysis in Sec. V G shows that $5b/a \simeq 0.11$, thus it can be expected that the VLB implementation is roughly one order of magnitude faster than the CLB implementation.

In order to quantitatively assess the computational performance of the VLB and CLB implementations, we
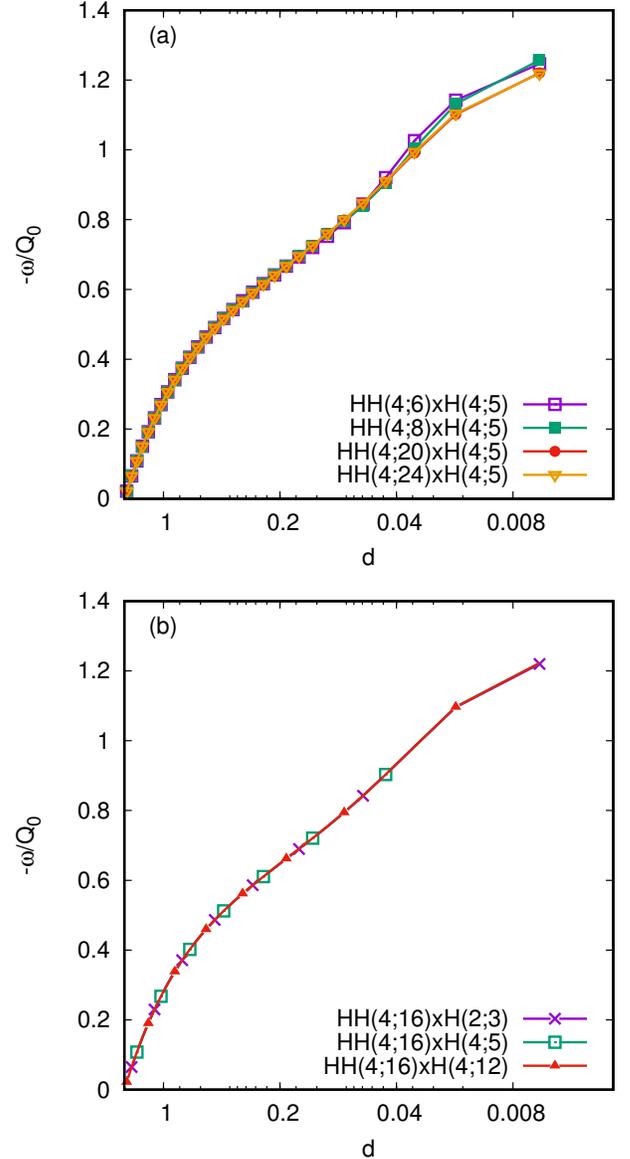
FIG. 32. Convergence study of the normalized vorticity with respect to quadrature order Q_λ (a) and Q_ξ (b) for the VLB implementation at $y/L_c \simeq 0.25$.

evaluate the number of million of sites updated per second (Msites/s) MS (5.73), which in the case of the gradually expanding channel reads:

$$\text{MS} = \frac{N_\lambda \times N_\xi}{10^6 \Delta T} = \frac{0.006}{\Delta T}, \qquad (6.67)$$

where ΔT is expressed in seconds. In order to account for runtime fluctuations, we perform for each value of Q a series of simulations with total number of iterations N_{iter} varying between $5 \leq N_{\text{iter}} \leq 15$. For each simulation, the value of MS is computed using the formula:

$$\text{MS}(N_{\text{iter}}) = \frac{0.006 N_{\text{iter}}}{T(N_{\text{iter}})}, \qquad (6.68)$$

FIG. 34. Number of millions of site updates per second in the context of the gradually expanding channel Couette flow for a system with $N_\lambda \times N_\xi = 30 \times 200$ nodes when the VLB HHLB$(4;Q) \times$ HLB$(4;5)$ (lines and squares) and CLB HHLB$(4;Q) \times$ HHLB$(4;Q)$ (lines and circles) models are employed. The solid lines correspond to Eqs. (6.65) and (6.66), where the parameters a, b and c are obtained using a fitting routine.

FIG. 33. Comparison of the VLB and CLB implementations. Convergence study of the normalized vorticity for the CLB implementation with respect to quadrature order by (a) steadily increasing the quadrature order on both axes at $y/L_c \simeq 0.041$ and (b) keeping Q_x fixed and varying Q_y at $y/L_c \simeq 0.154$.

where $T(N_{\mathrm{iter}})$ is the total runtime to complete N_{iter} iterations, expressed in seconds. The value of MS corresponding to a given quadrature order Q is computed by averaging over the values MS(N_{iter}).

Figure 34 shows the dependence of MS with respect to Q for the VLB (lines and circles) and CLB (lines and squares) implementations. The solid lines correspond to the best fits of Eqs. (6.65) and (6.66) to the numerical data. The results of the numerical fits for the particular case of a grid comprised of $N_\lambda \times N_\xi = 30 \times 200 = 6000$ nodes are $a_{\mathrm{v}} \simeq 4.97$ ms, $b_{\mathrm{v}} \simeq 0.071$ ms, $a_{\mathrm{c}} \simeq 4.12$ ms, while the free coefficient c appears to be negligible in both

implementations. Thus, at large quadrature orders Q, it can be expected that time per iteration ratio between the VLB and CLB implementations is $5b_{\mathrm{v}}/a_{\mathrm{c}} \simeq 0.086$. For low Mach number flows, Q_ξ can be decreased below the value $Q_\xi = 5$ considered above such that the time per iteration ratio becomes $Q_\xi b_{\mathrm{v}}/a_{\mathrm{c}} \simeq 0.0172 Q_\xi$. Thus, it can be expected that the VLB implementation is in general at least one order of magnitude faster than the CLB implementation at the same level of accuracy.

H. Summary

In this Section, the vielbein formalism was employed to study flows through channels with non-planar walls. In particular, we considered the case of the gradually expanding channel, for which the expanding Section is governed by a hyperbolic tangent. Adapting the coordinate system to the channel boundary induces a non-diagonal metric. Our choice for the vielbein field allows the momentum space to be aligned along the boundary, such that the diffuse reflection boundary conditions can be implemented just like in the case of planar walls.

Our implementation is validated in the incompressible hydrodynamics limit, where our results obtained using the H(2; 3) × H(2; 3) model (employing 9 velocities) are successfully compared with computational fluid dynamics (CFD) results. We further presented results for the

compressible hydrodynamics case, when the temperature is no longer a constant. Our analysis of the flow through the gradually expanding channel ends with an analysis of rarefaction effects. In particular, we highlight the deviations from the hydrodynamic solution of the pressure-driven flow in the case when the pressure gradient is no longer proportional to Kn. We further validate the results for the temperature profile by successfully fitting a quartic function of the distance from the channel center to the numerical data. The ability of our implementation to capture rarefaction effects was demonstrated by highlighting the logarithmic divergence of the vorticity inside the Knudsen layer.

Finally, we discuss the advantages of using the vielbein formalism (VLB) in contrast with the case when the momentum space is discretized with respect to its Cartesian degrees of freedom (p^x, p^y) (CLB). In the context of the gradually expanding channel, the flow domain cannot be reduced to one dimension. However, the VLB formalism allows the momentum space to be factorized such that one component is always perpendicular to the wall. Our analysis shows that this allows a full-range Gauss-Hermite quadrature of low order to be employed on the direction which remains parallel to the wall, while the accuracy of the simulation depends only on the quadrature along the direction which is perpendicular to the wall. In the CLB implementation, the momentum space directions are always parallel to the (fixed) x and y axes. Accurate simulation results of the flow inside the expanding portion of the channel can be obtained only when the half-range Gauss-Hermite quadrature is employed on both axes, at equally high order. Moreover, the vorticity profile obtained in the CLB formulation exhibits oscillations near the wall (inside the Knudsen layer), which are not present when the VLB implementation is used. An analysis of the runtime of the CLB and VLB implementations at the same level of accuracy (same values for the half-range Gauss-Hermite quadratures) shows that, at large values of the quadrature order, the VLB implementation is one order of magnitude faster than the CLB implementation.

VII. CONCLUSION

In this paper, the Boltzmann equation with respect to curvilinear coordinates was considered, written with respect to orthonormal vielbein fields (triads in $3D$), extending the formalism introduced in Ref. [48] for the relativistic Boltzmann equation to the non-relativistic case. The vielbein can be used to align the momentum space along the coordinate directions, while also decoupling the dependence of $(\boldsymbol{p} - m\boldsymbol{u})^2$ appearing in the Maxwell-Boltzmann equilibrium distribution on the induced metric tensor. Our formalism allows the Boltzmann equation to be obtained in conservative form for any choice of coordinates using elementary differential geometry.

Choosing a coordinate system adapted to the bound-ary of the fluid domain allows the momentum space to be aligned such that the incoming and outgoing fluxes are described by conditions of the form $p^{\hat{a}} > 0$ and $p^{\hat{a}} < 0$, respectively. The separation of incoming and outgoing particles is directly amenable to discretizations of the momentum space based on half-range quadratures. In the case when the flow shares the symmetries of the curvilinear grid, aligning the momentum space to the coordinate grid results in a phase space which preserves the symmetries of the flow, allowing the spatial dimensions along which the flow is homogeneous to be suppressed.

To illustrate the advantages of this methodology, we considered two applications, namely the circular Couette flow between coaxial cylinders and the flow through a gradually expanding channel. In the first case, the use of vielbeins in the momentum space allows a one dimensional spatial grid to be employed. In the second case, the vielbeins allow the momentum space degrees of freedom to be aligned along the boundary, making the implementation of diffuse reflection using half-range Gauss-Hermite quadratures identical to the case of Cartesian geometries.

The validation of our scheme in the context of the circular Couette flow was performed by comparing our simulation results with the analytic solutions in the hydrodynamic and ballistic regimes and with the transition regime results reported in Ref. [88], which were obtained using high-order Discrete Velocity Models. We performed simulations in the incompressible (low-Mach number) regime, as well as in the non-negligible Mach number regime. In the latter case, we were able to successfully recover the temperature, stress-tensor and heat flux fields. Thus, we conclude that our resulting scheme is applicable for the simulation of the circular Couette flow of a compressible gas obeying the Boltzmann-BGK equation for all degrees of rarefaction.

In the context of the gradually expanding channel, our numerical results were validated in the incompressible limit of the Navier-Stokes regime by comparison with the benchmark CFD solutions reported in Refs. [100, 129] for the case when the Reynolds number is Re = 100, achieved by setting the inlet debit at $Q_0 = 0.1$ and a Knudsen number of Kn = 0.001. Maintaining Re = 100 while increasing the viscosity $\mu = $ Kn brings the flow in the compressible, non-isothermal regime, where we highlighted the temperature variation in the transverse direction, as well as the enhancement of the vortex dimensions with the increase of the debit at the inlet. Finally we explored the rarefaction effects by keeping $Q_0 = 0.1$ for increasing values of Kn. We were able to highlight deviations from the Hagen-Poiseuille law for the pressure gradient, as well as the formation of a Knudsen layer where the vorticity diverges logarithmically with the distance to the boundary.

Since our quadrature-based lattice Boltzmann models are off-lattice, we employed high-order finite-difference methods such as the total variation diminishing third-order Runge-Kutta (TVD RK-3) method developed

in Ref. [84] for the time-stepping procedure, together with the fifth-order weighted essentially non-oscillatory (WENO-5) method for the computation of the numerical fluxes. Noting that the non-trivial features of the flow form predominantly near the domain boundaries, we employed a grid stretching method inspired from Refs. [40, 65]. We were thus able to obtain accurate simulation results with a comparatively small number of grid nodes, ranging from 96 points to 16 points in the hydrodynamic and ballistic regimes for the circular Couette flow and $30 \times 200 = 6000$ nodes for the gradually expanding channel.

During the analysis of the circular Couette flow, we considered two formulations of the Boltzmann equation, namely the $\widetilde{f}$ and χ formulations. We found that applying the TVD RK-3 and WENO-5 schemes to solve the Boltzmann equation in the $\widetilde{f}$ formulation could not recover the simple solution $f = \text{constant}$ in the case when both cylinders were kept at rest and at the same temperature. We further demonstrated that in the $\widetilde{f}$ formulation, the macroscopic variables (number density n, temperature T and radial and tangential heat fluxes $q^{\hat{R}}$ and $q^{\hat{\varphi}}$) develop sharp jumps near the boundaries, as well as non-physical oscillations when the lattice spacing is coarse. With our implementation of the χ formulation of the Boltzmann equation, we were able to reproduce the exact solution $f = \text{constant}$ in the stationary case, and in the case when the cylinders undergo rotation, the resulting stationary profiles of n, T, $u^{\hat{\varphi}}$ and $q^{\hat{\varphi}}$ are smooth. However, the radial heat flux still exhibits jumps which are formed in the two nodes which are nearest to the boundaries. These jumps were visible only in the hydrodynamic regime, while at larger values of the relaxation time (i.e. for $\tau \gtrsim 0.01$), the stationary profile of $q^{\hat{R}}$ became smooth. We found that the effects of these irregularities on the bulk profiles were greatly diminished by applying the grid stretching technique to increase the resolution near the boundaries, while maintaining a considerably coarser resolution within the bulk of the flow. The gain in performance is evident, since we were able to obtain the same level of accuracy with a stretched grid comprised of 32 points per unit radial length as with the unstretched grid employing 128 points per unit radial length.

We finally draw some conclusions regarding the efficiency of our implementation. Since the dynamics along the vertical axis in the flows considered in this paper is trivial, we integrated out the p^z degree of freedom of the momentum space and introduced two sets of reduced distributions in order to solve the 2D Boltzmann equation.

In the incompressible limit of the Navier-Stokes regime, we recovered the analytic solution in the circular Couette flow problem, as well as the benchmark solutions of Refs. [100, 129] for the flow through the gradually expanding channel using the $H(2;3) \times H(2;3)$ model (i.e., the 3rd order full-range Gauss-Hermite quadrature on both axes) employing $3 \times 3 = 9$ velocities. While the number of velocities is the same as that employed by the popular D2Q9 lattice Boltzmann model, the efficiency of our implementation with respect to, e.g., Refs. [45, 53], is immediately obvious in the context of the circular Couette flow, since the vielbein approach allows us to employ a one-dimensional discretization of the spatial grid (i.e. only along the radial direction).

In the slip-flow and transition regimes of the circular Couette flow, our models employ a number of velocities similar to that used in the implementation presented in Ref. [43], which is based on a Cartesian split of the momentum space. Since the latter approach does not preserve the symmetries of the geometry, a 2D spatial grid is required, which makes our implementation more efficient by at least two orders of magnitude. Furthermore, the number of velocities employed in Ref. [88], where the cylindrical symmetry in the momentum space is retained (allowing a one-dimensional spatial grid to be used) is significantly larger than the one employed in our models, mainly due to the fact that our models employ the half-range Gauss-Hermite quadrature in order to implement the boundary conditions. Thus, our implementation is at least two orders of magnitude faster than that employed in Ref. [88] for $\text{Kn} \lesssim 10$. It is worth mentioning that at larger values of Kn, the number of velocities required for our models increases dramatically, becoming of the same order of magnitude to the number of velocities employed in Ref. [88].

The versatility of our models to probe rarefaction effects in non-Cartesian geometries is demonstrated by our simulations performed in the context of the gradually expanding channel for values of Kn up to 0.5, highlighting the formation of a Knudsen layer where the vorticity presents a logarithmic divergence with respect to the distance to the channel wall. To the best of our knowledge, our results represent the first account for rarefaction effects in the gradually expanding channel geometry. Our investigations show that the simulation of rarefied flows in the geometry of the gradually expanding channel is around one order of magnitude faster in the vielbein approach than when a Cartesian decomposition of the momentum space is employed.

Appendix A: Boltzmann equation with respect to general coordinates

It is easy to check that Eq. (2.4) is in covariant form, i.e. that its form remains unchanged under a change of coordinate system from $\{x^{\widetilde{\imath}}\}$ to some new coordinates $\{x^{\overline{\imath}}\}$. Also, it can be checked that Eq. (2.4) reduces to the Boltzmann equation (2.1) when Cartesian coordinates are employed.

For completeness, this appendix presents a derivation of the form in Eq. (2.4) without the use of the tools of differential geometry. The first step in writing the Boltzmann equation with respect to the new coordinates is to consider the differential of f:

$$df = \frac{\partial f}{\partial t}dt + \left(\frac{\partial f}{\partial x^i}\right)_{p^j}dx^i + \frac{\partial f}{\partial p^i}dp^i \qquad (A1a)$$

$$= \frac{\partial f}{\partial t}dt + \left(\frac{\partial f}{\partial x^{\widetilde{\imath}}}\right)_{p^{\widetilde{\jmath}}}dx^{\widetilde{\imath}} + \frac{\partial f}{\partial p^{\widetilde{\imath}}}dp^{\widetilde{\imath}}, \qquad (A1b)$$

where the notation $(\partial f/\partial x^i)_{p^j}$ refers to the derivative of f with respect to x^i while keeping p^j constant. In order to replace the derivatives occurring in Eq. (A1a) with those occurring in Eq. (A1b), the following results can be used:

$$dx^{\widetilde{\imath}} = \frac{\partial x^{\widetilde{\imath}}}{\partial x^j}dx^j, \qquad dp^{\widetilde{\imath}} = \frac{\partial x^{\widetilde{\imath}}}{\partial x^j}dp^j + p^j\frac{\partial^2 x^{\widetilde{\imath}}}{\partial x^k \partial x^j}dx^k. \qquad (A2)$$

Thus, the Boltzmann equation takes the form:

$$\frac{\partial f}{\partial t} + \frac{p^{\widetilde{\imath}}}{m}\frac{\partial f}{\partial x^{\widetilde{\imath}}} + \left(F^{\widetilde{\imath}} + \frac{1}{m}\frac{\partial^2 x^{\widetilde{\imath}}}{\partial x^j \partial x^k}p^j p^k\right)\frac{\partial f}{\partial p^{\widetilde{\imath}}} = J[f]. \qquad (A3)$$

Writing:

$$\frac{\partial^2 x^{\widetilde{\imath}}}{\partial x^j \partial x^k}p^j p^k = \frac{\partial x^j}{\partial x^{\widetilde{\jmath}}}\frac{\partial x^k}{\partial x^{\widetilde{k}}}\frac{\partial^2 x^{\widetilde{\imath}}}{\partial x^j \partial x^k}p^{\widetilde{\jmath}}p^{\widetilde{k}}$$

$$= -\frac{\partial x^{\widetilde{\imath}}}{\partial x^\ell}\frac{\partial^2 x^\ell}{\partial x^{\widetilde{\jmath}}\partial x^{\widetilde{k}}}p^{\widetilde{\jmath}}p^{\widetilde{k}}, \qquad (A4)$$

the identification (2.6) can be made on the last line above, such that Eq. (A3) reduces to (2.4).

Appendix B: Boltzmann equation with respect to orthonormal triads

The same methodology as in appendix A can be applied in the case when orthonormal triads are employed:

$$df = \frac{\partial f}{\partial t}dt + \left(\frac{\partial f}{\partial x^{\widetilde{\imath}}}\right)_{p^{\widetilde{\jmath}}}dx^{\widetilde{\imath}} + \frac{\partial f}{\partial p^{\widetilde{\imath}}}dp^{\widetilde{\imath}} \qquad (B1a)$$

$$= \frac{\partial f}{\partial t}dt + \left(\frac{\partial f}{\partial x^{\widetilde{\imath}}}\right)_{p^{\hat{a}}}dx^{\widetilde{\imath}} + \frac{\partial f}{\partial p^{\hat{a}}}dp^{\hat{a}}. \qquad (B1b)$$

In this case, it is possible to express $dp^{\hat{a}}$ as follows:

$$dp^{\hat{a}} = d(\omega_{\widetilde{\imath}}^{\hat{a}}p^{\widetilde{\imath}}) = \omega_{\widetilde{\imath}}^{\hat{a}}dp^{\widetilde{\imath}} + p^{\widetilde{\imath}}\frac{\partial \omega_{\widetilde{\imath}}^{\hat{a}}}{\partial x^{\widetilde{\jmath}}}dx^{\widetilde{\jmath}}. \qquad (B2)$$

Thus, the Boltzmann equation becomes:

$$\frac{\partial f}{\partial t} + \frac{p^{\hat{a}}}{m}e_{\hat{a}}^{\widetilde{\imath}}\frac{\partial f}{\partial x^{\widetilde{\imath}}}$$
$$+ \left[F^{\hat{a}} + \frac{1}{m}p^{\widetilde{\imath}}p^{\widetilde{\jmath}}\left(\frac{\partial \omega_{\widetilde{\imath}}^{\hat{a}}}{\partial x^{\widetilde{\jmath}}} - \omega_{\widetilde{k}}^{\hat{a}}\Gamma^{\widetilde{k}}_{\widetilde{\imath}\widetilde{\jmath}}\right)\right]\frac{\partial f}{\partial p^{\hat{a}}} = J[f]. \qquad (B3)$$

Noting that the connection coefficients $\Gamma^{\hat{a}}_{\hat{b}\hat{c}}$ are related to the covariant derivative of $\omega_{\widetilde{\imath}}^{\hat{a}}$ through:

$$\nabla_{\widetilde{\jmath}}\omega_{\widetilde{\imath}}^{\hat{a}} = \frac{\partial \omega_{\widetilde{\imath}}^{\hat{a}}}{\partial x^{\widetilde{\jmath}}} - \omega_{\widetilde{k}}^{\hat{a}}\Gamma^{\widetilde{k}}_{\widetilde{\imath}\widetilde{\jmath}}$$
$$= \omega_{\widetilde{\jmath}}^{\hat{c}}\nabla_{\hat{c}}\omega_{\widetilde{\imath}}^{\hat{a}}$$
$$= -\Gamma^{\hat{a}}_{\hat{b}\hat{c}}\omega_{\widetilde{\imath}}^{\hat{b}}\omega_{\widetilde{\jmath}}^{\hat{c}}. \qquad (B4)$$

The above result is sufficient to render Eq. (B3) in the form of Eq. (2.20).

Appendix C: Boltzmann equation in conservative form

Starting from Eq. (2.20), it is possible to arrive at Eq. (3.1) by forcing a $g^{-1/2}$ factor in front of each term on the left hand side, as follows:

$$\frac{1}{\sqrt{g}}\frac{\partial(f\sqrt{g})}{\partial t} + \frac{1}{\sqrt{g}}\frac{\partial}{\partial x^{\widetilde{\imath}}}\left(\frac{p^{\hat{a}}}{m}e_{\hat{a}}^{\widetilde{\imath}}f\sqrt{g}\right)$$
$$+ \frac{1}{\sqrt{g}}\frac{\partial}{\partial p^{\hat{a}}}\left[\left(F^{\hat{a}} - \frac{1}{m}\Gamma^{\hat{a}}_{\hat{b}\hat{c}}p^{\hat{b}}p^{\hat{c}}\right)f\sqrt{g}\right]$$
$$- f\left[\frac{p^{\hat{a}}}{m}\frac{1}{\sqrt{g}}\frac{\partial}{\partial x^{\widetilde{\imath}}}\left(e_{\hat{a}}^{\widetilde{\imath}}\sqrt{g}\right) - \left(\Gamma^{\hat{a}}_{\hat{a}\hat{b}} + \Gamma^{\hat{a}}_{\hat{b}\hat{a}}\right)\frac{p^{\hat{b}}}{m}\right] = J[f]. \qquad (C1)$$

The only step required to arrive at Eq. (3.1) is to show that the last term in the left hand side of Eq. (C1) vanishes.

First, we use the following property:

$$\frac{1}{\sqrt{g}}\frac{\partial}{\partial x^{\widetilde{\imath}}}\left(e_{\hat{a}}^{\widetilde{\imath}}\sqrt{g}\right) = \nabla_{\widetilde{\imath}}e_{\hat{a}}^{\widetilde{\imath}}. \qquad (C2)$$

We note that in the above, the covariant derivative refers only to the coordinate $\widetilde{\imath}$. Since the covariant derivative $\nabla_{\widetilde{\imath}}$ transforms as a tensor with respect to changes of coordinates, it is possible to express Eq. (C2) in terms of a covariant derivative in the tetrad index $\hat{b}$, as follows:

$$\nabla_{\widetilde{\imath}}e_{\hat{a}}^{\widetilde{\imath}} = \omega_{\widetilde{\imath}}^{\hat{b}}\nabla_{\hat{b}}e_{\hat{a}}^{\widetilde{\imath}}. \qquad (C3)$$

The covariant derivative of $e_{\hat{a}}^{\tilde{i}}$ with respect to $\hat{b}$ can be written, by definition, using the connection coefficients $\Gamma^{\hat{c}}_{\hat{a}\hat{b}}$, as follows:

$$\omega_{\tilde{i}}^{\hat{b}}\nabla_{\hat{b}}e_{\hat{a}}^{\tilde{i}} = \omega_{\tilde{i}}^{\hat{b}}\Gamma^{\hat{c}}_{\hat{a}\hat{b}}e_{\hat{c}}^{\tilde{i}}. \qquad (C4)$$

Noting that, by construction, $\omega_{\tilde{i}}^{\hat{b}}e_{\hat{c}}^{\tilde{i}} = \delta^{\hat{b}}_{\hat{c}}$, the following result is obtained:

$$\frac{1}{\sqrt{g}}\frac{\partial}{\partial x^{\tilde{i}}}\left(e_{\hat{a}}^{\tilde{i}}\sqrt{g}\right) = \Gamma^{\hat{b}}_{\hat{a}\hat{b}}. \qquad (C5)$$

With the above result, the last term in the left hand side of Eq. (C1) reduces to:

$$\frac{p^{\hat{a}}}{m}\frac{1}{\sqrt{g}}\frac{\partial}{\partial x^{\tilde{i}}}\left(e_{\hat{a}}^{\tilde{i}}\sqrt{g}\right) - \left(\Gamma^{\hat{a}}_{\hat{a}\hat{b}} + \Gamma^{\hat{a}}_{\hat{b}\hat{a}}\right)\frac{p^{\hat{b}}}{m} = -\Gamma^{\hat{a}}_{\hat{a}\hat{b}}\frac{p^{\hat{b}}}{m}. \qquad (C6)$$

Expression (2.24) is obtained after noting that $\Gamma^{\hat{a}}_{\hat{a}\hat{b}} = 0$, due to the antisymmetry of the connection coefficients in the first pair of indices.

Appendix D: Projection of the force term onto the space of orthogonal polynomials

In this Section of the appendix, the implementation of the momentum space derivatives $\partial_{p^{\hat{a}}}f$ and $\partial_{p^{\hat{a}}}(fp^{\hat{a}})$ of the distribution function f (or its reduced versions f' and f'' introduced in Sec. IV A) in the LB models employed in this paper is reviewed for the cases when the full-range and half-range Gauss-Hermite quadratures are employed. We consider that the momentum space is two-dimensional, since in the applications considered in this paper, the third dimension is reduced by analytic integration, as described in Sec. IV A. It is understood that all instances of f can be replaced directly by the reduced distributions f' and f''.

1. Projection on the space of full-range Hermite polynomials

a. Projection of $\partial f/\partial p^{\hat{a}}$

The projection of $\partial f/\partial p^{\hat{a}}$ onto the space of full-range Hermite polynomials has been discussed in the context of the LB models employed in this paper in Refs. [35, 36]. For completeness, we include in this Subsection a brief review of the results presented therein.

Let us consider the expansion of the distribution function f with respect to the momentum component $p^{\hat{a}}$ in terms of full-range Hermite polynomials:

$$f = \frac{e^{-p_{\hat{a}}^2/2}}{\sqrt{2\pi}}\sum_{\ell=0}^{\infty}\frac{1}{\ell!}\mathcal{F}_\ell H_\ell(p^{\hat{a}}). \qquad (D1)$$

The expansion coefficients $\mathcal{F}_\ell$ can be obtained using:

$$\mathcal{F}_\ell = \int_{-\infty}^{\infty}dp^{\hat{a}}\,f\,H_\ell(p^{\hat{a}}), \qquad (D2)$$

where the following orthogonality relation of the Hermite polynomials was used:

$$\int_{-\infty}^{\infty}\frac{dx}{\sqrt{2\pi}}e^{-x^2/2}H_\ell(x)H_{\ell'}(x) = \ell!\delta_{\ell,\ell'}. \qquad (D3)$$

The derivative of f with respect to $p^{\hat{a}}$ is given by:

$$\frac{\partial f}{\partial p^{\hat{a}}} = -\frac{e^{-p_{\hat{a}}^2/2}}{\sqrt{2\pi}}\sum_{\ell=0}^{\infty}\frac{1}{\ell!}\mathcal{F}_\ell H_{\ell+1}(p^{\hat{a}}), \qquad (D4)$$

where the relation $\partial_x[e^{-x^2/2}H_\ell(x)] = -e^{-x^2/2}H_{\ell+1}(x)$ was used.

For definiteness, let us consider a quadrature Q_1 along the first momentum space direction, such that $p^{\hat{1}}$ takes the discrete values $p_i^{\hat{1}}$ $(i = 1, 2, \ldots Q_1)$ satisfying $H_{Q_1}(p_i^{\hat{1}}) = 0$. The other component $p^{\hat{2}} \to \{p_j^{\hat{2}}\}$ $(j = 1, 2, \ldots Q_2)$ is also discretized according to an arbitrary quadrature, such that Eq. (D1) is replaced by:

$$f_{ij} = w_i^H\sum_{\ell=0}^{Q_1-1}\frac{1}{\ell!}\mathcal{F}_{\ell;j}H_\ell(p_i^{\hat{1}}), \qquad (D5)$$

where w_i^H is the full-range Gauss-Hermite quadrature weight defined in Eq. (4.10). The above definition of f_{ij} allows the integral in Eq. (D2) to be exactly recovered using the full-range Gauss-Hermite quadrature formula [37, 38]:

$$\mathcal{F}_{\ell;j} = \sum_{i=1}^{Q_1}f_{ij}H_\ell(p_i^{\hat{1}}). \qquad (D6)$$

Truncating Eq. (D4) following the above recipe gives:

$$\left(\frac{\partial f}{\partial p^{\hat{1}}}\right)_{ij} = \sum_{i'=1}^{Q_1}\mathcal{K}_{i,i'}^{\hat{1},H}f_{i'j}, \qquad (D7)$$

where the elements of the $Q_1 \times Q_1$ matrix $\mathcal{K}_{i,i'}^{\hat{1},H}$ are given in Eq. (4.15).

b. Projection of $\partial(fp^{\hat{a}})/\partial p^{\hat{a}}$

Starting from the expansion (D1) of f with respect to $p^{\hat{a}}$, a similar expansion for $\partial(fp^{\hat{a}})/\partial p^{\hat{a}}$ can be assumed:

$$\frac{\partial(fp^{\hat{a}})}{\partial p^{\hat{a}}} = \frac{e^{-p_{\hat{a}}^2/2}}{\sqrt{2\pi}}\sum_{\ell=0}^{\infty}\frac{1}{\ell!}\mathcal{F}_\ell' H_\ell(p^{\hat{a}}). \qquad (D8)$$

The coefficients $\mathcal{F}_\ell'$ can be obtained by multiplying Eq. (D8) by $H_\ell(p^{\hat{a}})$ and integrating with respect to $p^{\hat{a}}$:

$$\mathcal{F}_\ell' = -\int_{-\infty}^{\infty}dp^{\hat{a}}\,f\,p^{\hat{a}}\frac{\partial H_\ell(p^{\hat{a}})}{\partial p^{\hat{a}}}, \qquad (D9)$$

where integration by parts was used to arrive at the above result. Using the property $xH'_\ell(x) = \ell H_\ell(x) + \ell(\ell-1)H_{\ell-2}(x)$, the integral in Eq. (D9) can be performed in terms of the coefficients $\mathcal{F}_\ell$:

$$\mathcal{F}'_\ell = -\ell \mathcal{F}_\ell - \ell(\ell-1)\mathcal{F}_{\ell-2}. \tag{D10}$$

We now assume that a represents the first momentum space direction and $p^{\hat{1}} \to p_i^{\hat{1}}$ ($i = 1, 2, \ldots Q_1$) according to a full-range Gauss-Hermite quadrature of order Q_1. In this case, $\mathcal{F}'_\ell$ can be written as:

$$\mathcal{F}'_{\ell;j} = -\sum_{i'=1}^{Q_1} f_{i'j}[\ell H_\ell(p_{i'}^{\hat{1}}) + \ell(\ell-1)H_{\ell-2}(p_{i'}^{\hat{1}})]. \tag{D11}$$

Thus, $\partial(fp^{\hat{1}})/\partial p^{\hat{1}}$ (D8) can be written as a linear combination of f_{ij}:

$$\left[\frac{\partial(fp^{\hat{1}})}{\partial p^{\hat{1}}}\right]_{ij} = \sum_{i'=1}^{Q_1} \widetilde{\mathcal{K}}_{i,i'}^{\hat{1},H} f_{i'j}, \tag{D12}$$

where the elements of the $Q_1 \times Q_1$ matrix $\widetilde{\mathcal{K}}_{i,i'}^{\hat{1},H}$ are given in Eq. (4.18).

2. Projection on the space of half-range Hermite polynomials

a. Projection of $\partial f/\partial p^{\hat{a}}$

The construction of the derivative $\partial f/\partial p^{\hat{a}}$ in the frame of LB models based on the half-range Gauss-Hermite quadrature was presented in Ref. [36]. In this Subsection, the construction procedure and the main results are briefly reviewed.

The idea behind LB models based on half-range Gauss-Hermite quadratures is to acknowledge that the wall interaction induces a discontinuity in the distribution function, since the distribution of particles emitted by the diffuse reflective boundary has in general a different functional form compared to that of the distribution of the incident particles. Thus, it is natural to separate the space of incoming and outgoing particles as follows:

$$f(p^{\hat{a}}) = \theta(p^{\hat{a}})f^+(p^{\hat{a}}) + \theta(-p^{\hat{a}})f^-(p^{\hat{a}}). \tag{D13}$$

Taking the derivative of Eq. (D13) with respect to $p^{\hat{a}}$ gives:

$$\frac{\partial f}{\partial p^{\hat{a}}} = \theta(p^{\hat{a}})\left(\frac{\partial f}{\partial p^{\hat{a}}}\right)^+ + \theta(-p^{\hat{a}})\left(\frac{\partial f}{\partial p^{\hat{a}}}\right)^-, \tag{D14}$$

where

$$\left(\frac{\partial f}{\partial p^{\hat{a}}}\right)^\pm = \frac{\partial f^\pm}{\partial p^{\hat{a}}} + \delta(p^{\hat{a}})[f^+(0) - f^-(0)]. \tag{D15}$$

The Dirac delta function is obtained as the derivative of the Heaviside step functions:

$$\delta(x) = \pm\partial_x\theta(\pm x). \tag{D16}$$

In obtaining Eq. (D15), we used $\delta(p^{\hat{a}}) \to \delta(p^{\hat{a}})[\theta(p^{\hat{a}}) + \theta(-p^{\hat{a}})]$, while $f^\pm(0)$ are defined through:

$$f^+(0) = \lim_{p^{\hat{a}} \to 0+} f(p^{\hat{a}}), \qquad f^-(0) = \lim_{p^{\hat{a}} \to 0-} f(p^{\hat{a}}). \tag{D17}$$

In general, $f^+(0) \neq f^-(0)$ due to the interaction with the boundary.

Let us now consider the expansion of $f^\pm(p^{\hat{a}})$ with respect to the half-range Hermite polynomials [34, 36]:

$$f^\pm = \frac{e^{-p_{\hat{a}}^2/2}}{\sqrt{2\pi}} \sum_{\ell=0}^\infty \mathcal{F}_\ell^\pm \mathfrak{h}_\ell(|p^{\hat{a}}|), \tag{D18}$$

where the expansion coefficients $\mathcal{F}_\ell^\pm$ are given as:

$$\mathcal{F}_\ell^+ = \int_0^\infty dp^{\hat{a}}\, f\, \mathfrak{h}_\ell(p^{\hat{a}}), \qquad \mathcal{F}_\ell^- = \int_{-\infty}^0 dp^{\hat{a}}\, f\, \mathfrak{h}_\ell(-p^{\hat{a}}). \tag{D19}$$

The expansion of $(\partial f/\partial p^{\hat{a}})^\pm$ (D15) was obtained in Ref. [36]:

$$\left(\frac{\partial f}{\partial p^{\hat{a}}}\right)^\pm = \pm\frac{e^{-p_{\hat{a}}^2/2}}{\sqrt{2\pi}}\left\{\vphantom{\sum}\right.$$
$$\sum_{\ell=0}^\infty \mathcal{F}_\ell^\pm \sum_{s=\ell+1}^\infty \left[\frac{\mathfrak{h}_{s,0}\mathfrak{h}_{\ell,0}}{\sqrt{2\pi}} - \frac{1}{a_s}\delta_{\ell,s+1}\right]\mathfrak{h}_s(|p^{\hat{a}}|)$$
$$-\frac{1}{2\sqrt{2\pi}}\left[\sum_{\ell=0}^\infty(\mathcal{F}_\ell^+ + \mathcal{F}_\ell^-)\mathfrak{h}_{\ell,0}\right]\left[\sum_{s=0}^\infty \mathfrak{h}_{s,0}\mathfrak{h}_s(|p^{\hat{a}}|)\right]\left.\right\}, \tag{D20}$$

where the notation $\mathfrak{h}_{\ell,s}$ is defined in Eq. (4.13).

Let us now consider that $\hat{a}$ refers to the first momentum space direction and $p^{\hat{1}}$ is discretized using $p_i^{\hat{1}}$ ($i = 1, 2, \ldots 2Q_a$) according to the half-range Gauss-Hermite quadrature, as described in Eq. (4.6). Considering also that $p^{\hat{2}} \to p_j^{\hat{2}}$ according to an arbitrary quadrature method, the equivalent of Eq. (D5) becomes:

$$f_{ij} = w_i^{\mathfrak{h}} \sum_{\ell=0}^{Q_1-1} \frac{1}{\ell!}\mathcal{F}_{\ell;j}^+ \mathfrak{h}_\ell(p_i^{\hat{1}}),$$

$$f_{i+Q_1,j} = w_i^{\mathfrak{h}} \sum_{\ell=0}^{Q_1-1} \frac{1}{\ell!}\mathcal{F}_{\ell;j}^- \mathfrak{h}_\ell(p_i^{\hat{1}}), \tag{D21}$$

where $i = 1, 2, \ldots Q_1$ and the expansion on the second line corresponds to the negative momentum semi-axis. The expansion coefficients $\mathcal{F}_{\ell;j}^\pm$ can be obtained using the following quadrature sums:

$$\mathcal{F}_{\ell;j}^+ = \sum_{i=1}^{Q_1} f_{ij}\mathfrak{h}_\ell(p_i^{\hat{1}}), \qquad \mathcal{F}_{\ell;j}^- = \sum_{i=1}^{Q_1} f_{i+Q_1,j}\mathfrak{h}_\ell(p_i^{\hat{1}}). \tag{D22}$$

Truncating Eq. (D20) following the above recipe gives:

$$\left(\frac{\partial f}{\partial p^{\hat{1}}}\right)_{ij} = \sum_{i'=1}^{2Q_1} \mathcal{K}_{i,i'}^{\hat{1},\mathfrak{h}} f_{i'j},$$ (D23)

where the elements of the $2Q_1 \times 2Q_1$ matrix $\mathcal{K}_{i,i'}^{\hat{1},\mathfrak{h}}$ are given in Eq. (4.16).

b. Projection of $\partial(fp^{\hat{a}})/\partial p^{\hat{a}}$

Since the product $p^{\hat{a}}f$ vanishes at $p^{\hat{a}} = 0$, the δ term appearing in the expression of $\partial f/\partial p^{\hat{a}}$ does not appear in this case, such that $\partial(p^{\hat{a}}f)/\partial p^{\hat{a}}$ can be expanded as:

$$\frac{\partial(p^{\hat{a}}f)}{\partial p^{\hat{a}}} = \frac{e^{-p_{\hat{a}}^2/2}}{\sqrt{2\pi}} \sum_{\ell=0}^{\infty} \mathcal{F}_{\ell}^{\hat{a},\sigma} \mathfrak{h}(|p^{\hat{a}}|),$$ (D24)

where, $\sigma = \pm 1$ when $\pm p^{\hat{a}} > 0$. The coefficients $\mathcal{F}^{\hat{a},\pm}$ can be obtained by virtue of the orthogonality of the half-range Hermite polynomials using integration by parts:

$$\mathcal{F}_{\ell}^{\hat{a},+} = -\int_0^{\infty} dp^{\hat{a}} \, f \, p^{\hat{a}} \mathfrak{h}_{\ell}'(p^{\hat{a}}),$$

$$\mathcal{F}_{\ell}^{\hat{a},-} = -\int_{-\infty}^0 dp^{\hat{a}} \, f \, p^{\hat{a}} \mathfrak{h}_{\ell}'(-p^{\hat{a}}).$$ (D25)

The product $x\mathfrak{h}_{\ell}'(x)$ appearing above can be written as [34]:

$$x\mathfrak{h}_{\ell}'(x) = \ell\mathfrak{h}_{\ell}(x) + \frac{\mathfrak{h}_{\ell,0}^2 + \mathfrak{h}_{\ell-1,0}^2}{a_{\ell-1}\sqrt{2\pi}}\mathfrak{h}_{\ell-1}(x)$$
$$+ \frac{1}{a_{\ell-1}a_{\ell-2}}\mathfrak{h}_{\ell-2}(x). \quad (D26)$$

Substituting the above result into Eq. (D25) and using Eq. (D19) yields:

$$\mathcal{F}_{\ell}^{\hat{a},\pm} = -\left[\ell\mathcal{F}_{\ell}^{\pm} + \frac{\mathfrak{h}_{\ell,0}^2 + \mathfrak{h}_{\ell-1,0}^2}{a_{\ell-1}\sqrt{2\pi}}\mathcal{F}_{\ell-1}^{\pm} + \frac{1}{a_{\ell-1}a_{\ell-2}}\mathcal{F}_{\ell-2}^{\pm}\right].$$ (D27)

Let us now consider that the $\hat{a}$ direction corresponds to the first direction of the momentum space and $p^{\hat{1}}$ is discretized according to the half-range Gauss-Hermite quadrature of order Q_1, such that Eq. (D24) takes the form:

$$\left[\frac{\partial(p^{\hat{1}}f)}{\partial p^{\hat{1}}}\right]_{ij} = \sum_{i'=1}^{2Q_1} \widetilde{\mathcal{K}}_{i,i'}^{\hat{1},\mathfrak{h}} f_{i',j},$$ (D28)

where the elements of the $2Q_1 \times 2Q_1$ matrix $\widetilde{\mathcal{K}}_{i,i'}^{\hat{1},\mathfrak{h}}$ are given in Eq. (4.19).

[1] H. Grad, *Principles of the Kinetic Theory of Gases*, Encyclopedia of Physics vol. 3/12, edited by S. Flügge (Springer, Berlin, 1958), DOI: doi.org/10.1007/978-3-642-45892-7_3.

[2] M. N. Kogan, *Rarefied gas dynamics* (Plenum press, New York, NY, 1969).

[3] C. Cercignani, *The Boltzmann equation and its applications* (Springer-Verlag, New York, NY, 1988).

[4] C. Cercignani, *Rarefied gas dynamics - From basic concepts to actual calculations* (Cambridge University Press, Cambridge, 2000).

[5] R. L. Liboff, *Kinetic Theory: Classical, Quantum and Relativistic Descriptions*, (Springer-Verlag, New York, NY, 2003), 3rd ed.

[6] G. Karniadakis, A. Beskok, and N. Aluru, *Microflows and Nanoflows: Fundamentals and Simulation* (Springer, Berlin, 2005).

[7] H. Struchtrup, *Macroscopic Transport Equations for Rarefied Gas Flows* (Springer, Berlin, 2005).

[8] C. Shen, *Rarefied gas dynamics - Fundamentals, simulations and micro flows* (Springer-Verlag, Berlin, 2005).

[9] M. Gad-el-Haq (Editor), *MEMS Handbook* (CRC Press, Boca Raton, 2006).

[10] Y. Sone, *Molecular Gas Dynamics: Theory, Techniques and Applications* (Birkhäuser, Boston, 2007).

[11] F. Sharipov, *Rarefied gas dynamics: Fundamentals for research and practice* (Wiley-VCH, Weinheim, 2016).

[12] J. P. Meng and Y. H. Zhang, J. Comput. Phys. **230**, 835–849 (2011).

[13] J. P. Meng and Y. H. Zhang, Phys. Rev. E **83**, 036704 (2011).

[14] J. P. Meng, Y. H. Zhang, and X. W. Shan, Phys. Rev. E **83**, 046701 (2011).

[15] J. P. Meng, Y. H. Zhang, N. G. Hadjiconstantinou, G. A. Radtke, and X. W. Shan, J. Fluid. Mech. **718**, 347–370 (2013).

[16] V. E. Ambruș and V. Sofonea, Phys. Rev. E **98**, 063311 (2018).

[17] E. P. Gross, E. A. Jackson, and S. Ziering, Ann. Phys. **1**, 141–167 (1957).

[18] J. Y. Yang, J. C. Huang, and L. Tsuei, P. R. Soc. A **448**, 55–80 (1995).

[19] Z.-H. Li and H.-X. Zhang, Int. J. Numer. Meth. Fl. **42**, 361–382 (2003).

[20] Z.-H. Li and H.-X. Zhang, J. Comput. Phys. **193**, 708–738 (2004).

[21] Z.-H. Li and H.-X. Zhang, J. Comput. Phys. **228**, 1116–1138 (2009).

[22] S. Lorenzani, L. Gibelli, A. Frezzotti, A. Frangi, and C. Cercignani, Nanosc. Microsc. Therm. **11**, 211–226 (2007).

[23] A. Frezzotti, L. Gibelli, and B. Franzelli, Continuum Mech. Therm. **21**, 495–509 (2009).

[24] A. Frezzotti, G. P. Ghiroldi, and L. Gibelli, Comput. Phys. Commun. **182**, 2445–2453 (2011).

[25] L. Gibelli, Phys. Fluids **24**, 022001 (2012).

[26] Z. Guo, K. Xu, and R. Wang, Phys. Rev. E **88**, 033305 (2013).

[27] G. P. Ghiroldi and L. Gibelli, J. Comput. Phys. **258**, 568–584 (2014).

[28] V. E. Ambruș and V. Sofonea, Phys. Rev. E **89**, 041301 (2014).

[29] V. E. Ambruș and V. Sofonea, Interfac. Phenom. Heat Transfer **2**, 235–251 (2014).

[30] V. E. Ambruș and V. Sofonea, Int. J. Mod. Phys. C **25**, 1441011 (2014).

[31] Z. Guo, R. Wang, and K. Xu, Phys. Rev. E **91**, 033313 (2015).

[32] G. P. Ghiroldi and L. Gibelli, Commun. Comput. Phys. **17**, 1007–1018 (2015).

[33] Y. Shi, Y. W. Yap, and J. E. Sader, Phys. Rev. E **92**, 013307 (2015).

[34] V. E. Ambruș and V. Sofonea, J. Comput. Phys. **316**, 760–788 (2016).

[35] V. E. Ambruș and V. Sofonea, J. Comput. Sci. **17**, 403–417 (2016).

[36] V. E. Ambruș, V. Sofonea, R. Fournier, and S. Blanco, arXiv:1708.03249, [physics.flu-dyn].

[37] F. B. Hildebrand, *Introduction to Numerical Analysis*, 2nd ed. (Dover Publications, Toronto, 1987).

[38] B. Shizgal, *Spectral Methods in Chemistry and Physics - Applications to Kinetic Theory and Quantum Mechanics* (Springer, Dordrecht, 2015).

[39] L. Mieussens, J. Comput. Phys. **162**, 429–466 (2000).

[40] Z. Guo and T. S. Zhao, Phys. Rev. E **67**, 066709 (2003).

[41] M. Mendoza and J.-D. Debus, Int. J. Mod. Phys. C **25**, 1441001 (2014).

[42] C. Lin, A. Xu, G. Zhang, Y. Li, and S. Succi, Phys. Rev. E **89**, 013307 (2014).

[43] M. Watari, J. Fluids Eng. **138**, 011202 (2016).

[44] J.-D. Debus, M. Mendoza, S. Succi, and H. J. Herrmann, Phys. Rev. E **93**, 043316 (2016).

[45] K. Hejranfar, M. H. Saadat, and S. Taheri, Phys. Rev. E **95**, 023314 (2017).

[46] K. Hejranfar and M. Hajihassanpour, Comput. Fluids **146**, 154–173 (2017).

[47] A. M. Velasco, J. D. Muñoz, and M. Mendoza, J. Comput.Phys. **376**, 76–97 (2019).

[48] C. Y. Cardall, E. Endeve, and A. Mezzacappa, Phys. Rev. D **88**, 023011 (2013).

[49] I. Nitschke, A. Voigt, and J. Wensch, J. Fluid Mech. **708**, 418–438 (2012).

[50] S. Reuther and A. Voigt, Multiscale Model. Simul. **13**, 632–643 (2015).

[51] S. Reuther and A. Voigt, J. Comput. Phys. **322**, 850–858 (2016).

[52] S. Reuther and A. Voigt, Phys. Fluids **30**, 012107 (2018).

[53] L. Budinsky, Comput. Fluids **96**, 288–301 (2014).

[54] J. P. Meng and Y. H. Zhang, J. Comput. Phys. **230**, 835–849 (2011).

[55] J. P. Meng and Y. H. Zhang, Phys. Rev. E **83**, 036704 (2011).

[56] J. P. Meng, Y. H. Zhang, and X. W. Shan, Phys. Rev. E **83**, 046701 (2011).

[57] M. Watari and M. Tsutahara, Phys. Rev. E **67**, 036306 (2003).

[58] M. Watari and M. Tsutahara, Phys. Rev. E **70**, 016703 (2004).

[59] M. Watari and M. Tsutahara, Physica A **364**, 129–144 (2006).

[60] F. Nannelli and S. Succi, J. Stat. Phys. **68**, 401–407 (1992).

[61] S. Succi, G. Amati, and R. Benzi, J. Stat. Phys. **81**, 5–16 (1995).

[62] G. McNamara, A. L. Garcia, and B. J. Alder, J. Stat. Phys. **81**, 395–408 (1995).

[63] M. B. Reider and J. D. Sterling, Comput. Fluids **24**, 459–467 (1995).

[64] N. Cao, S. Chen, S. Jin, and D. Martinez, Phys. Rev. E **55**, R21 (1997).

[65] R. Mei and W. Shyy, J. Comput. Phys. 143, 426–448 (1998).

[66] W. Shi, W. Shyy, and R. Mei, Numer. Heat Transfer, Part B **40**, 1–21 (2001).

[67] S. Teng, Y. Chen, and H. Ohashi, Int. J. Heat Fluid Flow **21**, 112–121 (2000).

[68] T. Seta, K. Kono, D. Martinez, and S. Chen, JSME Int. J. Ser. B **43**, 305–313 (2000).

[69] V. Sofonea, A. Lamura, G. Gonnella, and A. Cristea, Phys. Rev. E **70**, 046702 (2004).

[70] Y. Gan, A. Xu, G. Zhang, X. Yu, and Y. Li, Physica A **387**, 1721–1732 (2008).

[71] D. V. Patil and K. N. Lakshmisha, J. Comput. Phys. **228**, 5262–5279 (2009).

[72] B. Piaud, S. Blanco, R. Fournier, V. E. Ambruș, V. Sofonea, Int. J. Mod. Phys. C **25**, 1340016 (2014).

[73] T. Biciușcă, A. Horga, and V. Sofonea, C. R. Mecanique **343**, 580–588 (2015).

[74] S. Busuioc, V. E. Ambruș, and V. Sofonea, AIP Conf. Proc. **1796**, 020009 (2017).

[75] A. Cristea and V. Sofonea, Cent. Eur. J. Phys. **2**, 382–396 (2004).

[76] P. Fede, V. Sofonea, R. Fournier, S. Blanco, O. Simonin, G. Lepoutére, and V. E. Ambruș, Int. J. Multiphas. Flow **76**, 187–197 (2015).

[77] V. Sofonea, T. Biciușcă, S. Busuioc, V. E. Ambruș, G. Gonnella, A. Lamura, Phys. Rev. E **97**, 023309 (2018).

[78] G. S. Jiang and C. W. Shu, J. Comput. Phys. **126**, 202–228 (1996).

[79] C.-W. Shu, in *High-order methods for computational physics*, edited by T. J. Barth, H. Deconinck (Springer-Verlag, Berlin, 1999).

[80] Y. Gan, A. Xu, G. Zhang, and Y. Li, Phys. Rev. E **83**, 056704 (2011).

[81] L. Rezzolla and O. Zanotti, *Relativistic hydrodynamics* (Oxford University Press, Oxford, 2013).

[82] V. E. Ambruș and R. Blaga, Phys. Rev. C **98**, 035201 (2018).

[83] S. Busuioc, V. E. Ambruș, T. Biciușcă, and V. Sofonea, Comput. Math. Appl., *accepted for publication*.

[84] C.-W. Shu and S. Osher, J. Comput. Phys. **77**, 439–471 (1988).

[85] S. Gottlieb and C.-W. Shu, Math. Comput. **67**, 73–85 (1998).

[86] A. K. Henrick, T. D. Aslam, and J. M. Powers, J. Comput. Phys. **207**, 542–567 (2005).

[87] J. A. Trangenstein, *Numerical solution of hyperbolic partial differential equations* (Cambridge University Press, New York, NY, 2007).

[88] K. Aoki, H. Yoshida, T. Nakanishi, and A. L. Garcia, Phys. Rev. E **68**, 016302, (2003).

[89] C.-H. Kong and I-C. Liu, Phys. Fluids **6**, 2617–2622 (1994).

[90] H. Yoshida and K. Aoki, Phys. Rev. E **73**, 021201 (2006).

[91] K. W. Tibbs, F. Baras, and A. L. Garcia, Phys. Rev. E **56**, 2282–2283 (1997).

[92] S. Yuhong, R. W. Barber, and D. R. Emerson, Phys. Fluids **17**, 047102 (2005).

[93] Y. Jung, Phys. Rev. E **75**, 051203 (2007).

[94] A. Agrawal and S. V. Prabhu, Exp. Therm. Fluid Sci. **32** 991–996 (2008).

[95] S. Kim, Phys. Rev. E **79**, 036312 (2009).

[96] Z. Guo, B. Shi, and C. Zheng, Comput. Math. Appl. **61** 3519–3527 (2011).

[97] N. Dongari, R. W. Barber, D. R. Emerson, Y. Zhang, and J. M. Reese, J. Phys. Conf. Ser. **362**, 012009 (2012).

[98] S. Kosuge, Phys. Rev. E **92**, 013013 (2015).

[99] H. Akhlaghi and K. Javadi, Vacuum **121**, 56–63 (2015).

[100] P. J. Roache, *Scaling of high-Reynolds-number weakly separated channel flows*, chapter in Proceedings of a Symposium on *Numerical and physical aspects of aerodynamic flows*, edited by T. Cebeci (Springer, New York, NY, 1982), 87–98.

[101] M. Napolitano and P. Orlandi, Int. J. Numer. Meth. Fl. **5**, 667–683 (1985).

[102] V. Sofonea, Phys. Rev. E **74**, 056705 (2006).

[103] G. Gonnella, A. Lamura, and V. Sofonea, Eur. Phys. J. - Spec. Top. **171**, 181–187 (2009).

[104] V. Sofonea, J. Comput. Phys. **228**, 6107–6118 (2009).

[105] P. Romatschke, M. Mendoza, and S. Succi, Phys. Rev. C. **84**, 034903 (2011).

[106] V. E. Ambruș and V. Sofonea, Phys. Rev. E **86**, 016708 (2012).

[107] R. J. LeVeque, *Finite Volume Methods for Hyperbolic Problems*, (Cambridge University Press, Cambridge, 2002), 1st ed.

[108] E. M. Shakov, Fluid Dyn. **3**, 112–115 (1968).

[109] V. A. Titarev, Comput. Fluids **36**, 1446–1459 (2007).

[110] I. A. Graur and A. P. Polikarpov, Heat Mass Transfer **46**, 237–244 (2009).

[111] I. Graur, M. T. Ho and M. Wuest, J. Vacuum Sci. Technol. A: Vacuum Surf. Films **31**, 061603 (2013).

[112] M. T. Ho and I. Graur, Int. J. Heat Mass Transfer **90**, 58–71 (2015).

[113] S. A. E. G. Falle and S. S. Komissarov, Mon. Not. R. Astron. Soc. **278**, 586–602 (1996).

[114] T. P. Downes, P. Duffy, and S. S. Komissarov, Mon. Not. R. Astron. Soc. **332**, 144–154 (2002).

[115] J. C. Butcher, *Numerical Methods for Ordinary Differential Equations* (2nd edition), John Wiley & Sons, Chichester, West Sussex, England (2008).

[116] X. Shan, X.-F. Yuan, and H. Chen, J. Fluid Mech. **550**, 413–441 (2006).

[117] F. M. Sharipov and G. M. Kremer, Eur. J. Mech. B-Fluids **18**, 121–130 (1999).

[118] H. An, C. Zhang, J. Meng, and Y. Zhang, Physica A **391**, 8–14 (2012).

[119] L. M. G. Cumin, G. M. Kremer, and F. Sharipov, Math. Mod. Meth. Appl. S. **12**, 445–459 (2002).

[120] N. Dongari, C. White, T. J. Scanlon, Y. Zhang, and J. M. Reese, Phys. Fluids **25**, 052003 (2013)

[121] V. A. Titarev and E. M. Shakhov, Comp. Math. Math. Phys.+ **46**, 505–513 (2006).

[122] P. K. Kundu, I. M. Cohen, D. R. Dowling, *Fluid Mechanics*, 6th edition (Academic Press, 2015).

[123] M. Rieutord, *Fluid dynamics: an introduction* (Springer, 2015).

[124] D. R. Willis, Phys. Fluids **8**, 1908–1910 (1965).

[125] H. Sugimoto and Y. Sone, Phys. Fluids A **4**, 419–440 (1992).

[126] Y. Sone and H. Sugimoto, Phys. Fluids A **5**, 1491–1511 (1993).

[127] Y. Sone and H. Sugimoto, Phys. Fluids **7**, 2072–2085 (1995).

[128] Z. Zhang, W. Zhao, Q. Zhao, G. Lu, and J. Xu, Mod. Phys. Lett. B **32**, 1850048 (2018).

[129] K. A. Cliffe, C. P. Jackson, and A. C. Greenfield, *Finite-element solutions for flow in a symmetric channel with a smooth expansion*, Harwell Rep, AERE R-10608, HMSO (1982).

[130] C. Cercignani, *Theory and application of the Boltzmann equation* (Scottish Academic Press, Edinburgh, 1975).

[131] S. S. Lo and S. K. Loyalka, J. Appl. Math. Phys. (ZAMP) **33**, 419–424 (1982).

[132] F. Sharipov, J. Vac. Sci. Technol. A **17**, 3062–3066 (1999).

[133] C. Cercignani and C. D. Pagani, Phys. Fluids **9**, 1167–1173 (1966).

[134] M. Wang and Z. Li, Int. J. Heat Int. J. Heat Fluid Fl. **25**, 975–985 (2004).

[135] S.-M. Hou, Z.-H. Li, X.-Y. Jiang and S. Zeng, Commun. Comput. Phys. **23**, 1393–1414 (2018).

[136] Y. Sone, Phys. Fluids **7**, 470–471 (1964).

[137] Y. W. Yap and J. E. Sader, Phys. Fluids **24**, 032004 (2012).

[138] W. Li, L.-S. Luo, J. Shen, Comput. Fluids **111**, 18–32 (2015).

[139] S. Jiang and L.-S. Luo, J. Comput. Phys. **316**, 416–434 (2016).

[140] M. M. Mansour, F. Baras, and A. L. Garcia, Physica A **240**, 255–267 (1997).

[141] S. Hess and M.M. Mansour, Physica A **272**, 481–496 (1999).

[142] K. Xu, Phys. Fluids **15**, 2077–2080 (2003).

[143] Y. Zheng, A. L. Garcia, and B. J. Alder, J. Stat. Phys. **109**, 495–505 (2002).

[144] V. Sofonea, Europhys. Lett. **76**, 829–835 (2006).

[145] S. Balay, S. Abhyankar, M. F. Adams, J. Brown, P. Brune, K. Buschelman, L. Dalcin, V. Eijkhout, W. D. Gropp, D. Kaushik, M. G. Knepley, L. C. McInnes, K. Rupp, B. F. Smith, S. Zampini, H. Zhang, and H. Zhang, *PETSc Users Manual*,(Argonne National Laboratory ,2016), Technical Report ANL-95/11 – Revision 3.7, *PETSc Web page*: http://www.mcs.anl.gov/petsc.

[146] S. Balay, W. D. Gropp, L. C. McInnes, and B. F. Smith, *Efficient Management of Parallelism in Object Oriented Numerical Software Libraries*, Ed. E. Arge, A. M. Bruaset, and H. P. Langtangen (Birkhäuser Press, 1997), 163–202.